



UNIVERSIDAD NACIONAL AUTÓNOMA DE MÉXICO
PROGRAMA DE MAESTRÍA Y DOCTORADO EN INGENIERÍA
MAESTRÍA EN INGENIERÍA MECÁNICA – TERMOFLUIDOS

AEROTHERMODYNAMIC ANALYSIS OF THE REATTACHMENT RING ON
BLUNT SPIKED BODIES AT MULTIPLE ANGLES OF ATTACK

TESIS
QUE PARA OPTAR POR EL GRADO DE:
MAESTRO EN INGENIERÍA

PRESENTA:
ANTONIO ESDRAS ZAMARRÓN HIDALGO

TUTORES PRINCIPALES
GABRIEL, ASCANIO, GASCA, ICAT
JORGE, RAMÍREZ, CRUZ, FACULTAD DE INGENIERÍA

Ciudad Universitaria, CD. MX. ENERO 2024



Universidad Nacional
Autónoma de México

Dirección General de Bibliotecas de la UNAM

Biblioteca Central



UNAM – Dirección General de Bibliotecas
Tesis Digitales
Restricciones de uso

DERECHOS RESERVADOS ©
PROHIBIDA SU REPRODUCCIÓN TOTAL O PARCIAL

Todo el material contenido en esta tesis esta protegido por la Ley Federal del Derecho de Autor (LFDA) de los Estados Unidos Mexicanos (México).

El uso de imágenes, fragmentos de videos, y demás material que sea objeto de protección de los derechos de autor, será exclusivamente para fines educativos e informativos y deberá citar la fuente donde la obtuvo mencionando el autor o autores. Cualquier uso distinto como el lucro, reproducción, edición o modificación, será perseguido y sancionado por el respectivo titular de los Derechos de Autor.


JURADO ASIGNADO:

Presidente: Dr. William Vicente y Rodríguez
Secretario: Dr. Carlos Alberto Palacios Morales
1 er. Vocal: Dr. Gabriel Ascanio Gasca
2 do. Vocal: Dr. Ian Guillermo Monsivais Montoliu
3 er. Vocal: Dr. Jorge Ramírez Cruz

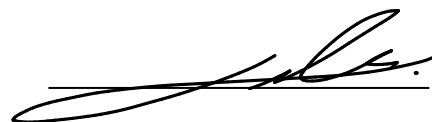
Ciudad Universitaria, Ciudad de México, México, 2024

TUTORES DE TESIS:

Dr. Gabriel Ascanio Gasca



Dr. Jorge Ramírez Cruz



Acknowledgements

“Only one who attempts the absurd is capable of achieving the impossible”. Miguel de Unamuno, 1905. [1]

I would not have been able to write this thesis without the support of so many people, I could never repay all the help you have given me, so I can only hope my words of appreciation reach you:

To my parents, Fabiola Hidalgo and Eduardo Alanís, for teaching me that reaching my dreams requires me to work hard and that whatever I do I should do with my utmost effort. "Do what you must, and the rest will follow". I love you.

To my father Antonio Zamarrón, for all the acts of kindness you have done for me, I know you have performed them from the bottom of your heart.

To my tutors, Dr. Gabriel Ascanio and Dr. Jorge Ramírez, for having near infinite patience, for supporting me innumerable times, and for helping me see this project through all the way from the beginning to the end.

To all my family, especially my grandparents and my aunt Raquel, who have helped me countless times and for turning really happy and proud every time I accomplish something, you truly fill my heart with joy.

To Sponky, whenever the wind may graze me, wherever the breeze may carry me, I know you will always be by my side, my eternal and loyal companion.

To Goyo and Leo, for brightening my every day and reminding me that life does not need to be complicated so I should take it slow every now and then.

To all my friends who have accompanied me through the years, for cheering me up, for making me smile and laugh, and for taking my fantasies serious and joining me in fulfilling them.

To my beloved alma mater, my second home, to the faculty of engineering, and to the teachers and students who make it up, for enriching my mind and spirit and teaching me everything I dreamed of learning as a kid. "Por mi raza hablará el espíritu".

To the countless persons who have helped me even in the smallest of ways, I would not be where I am without you.

And finally, to the kid inside me, who has relentlessly sought to understand the world around him, who wanted to fly with the clouds, and who told me to study engineering just because he found planes and vortexes fascinating, I will never stop listening to you, however absurd your dreams may be.

Thank you all, for believing in me, for raising me whenever I fell, for defending me from my own doubts, for helping me realize my potential, and for telling me my dreams were not fantasies. From the bottom of my heart, thank you.

Contents

Abstract	4
1 Introduction	6
1.1 Supersonic Flow	6
1.1.1 Conservation and Constitutive Equations.	6
1.1.2 Relevant dimensionless numbers and quantities	7
1.1.3 Shock Waves	10
1.1.4 Dimensionless Equations	11
1.2 Aerospike	12
1.2.1 Basic Mechanism	12
1.2.2 Aerodisk	13
1.2.3 Drag Reduction	14
1.2.4 Effective Body	15
1.2.5 Heat Reduction	16
1.3 Reattachment Ring	17
2 Motivation, hypothesis and objectives	17
2.1 Motivation	17
2.2 Hypothesis	18
2.3 Objectives	19
3 Methodology	20
3.1 SU2 Governing Equations	20
3.2 Turbulence Model	20
3.3 Validation Cases	22
3.3.1 Code Validation	22
3.3.2 Grid Independence Test	28
3.3.3 Mesh Design and Ringed Body Confirmation Test	28
3.3.4 Reattachment Ring at multiple angles of attack	36
4 Results	42
4.1 Code Validation Results	42
4.2 Grid Independence Test Results	47
4.3 Ringed Body Confirmation Test Results	48
4.4 Reattachment Ring at Multiple Angles of Attack Results	59
4.4.1 Drag Coefficient Results	59

4.4.2 Results at 0°	60
4.4.3 Results at 16°	62
4.4.4 Results at 30°	74
Conclusions	88
Further Research	88
References	89

Abstract

In the field of supersonic vehicle design it is often the case that blunt bodies are preferred because their larger surface area can better deal with the high heat flux caused by the body-shockwave interactions present in supersonic flows. However, blunt bodies have higher drag coefficients than those of their slender aerodynamic counterparts, that is why multiple drag and heat reduction methods have been studied and developed. One of them is the Aerospike, which works by decomposing the strong bow shockwave of the blunt body with a system of weaker shockwaves, this method's performance can be further enhanced by other auxiliary methods, such as the Aeroshield, and the more recent Reattachment Ring. Proposed by Elsamanoudy et al. [2], this latter reduction method alleviates the effects of the recompression shockwave caused by the aerospike, such as high temperatures and high heat flux on the blunt body shoulder, however its performance and flow structure at non-zero angles of attack have not been analyzed, and that is exactly the main objective of this thesis.

In the first chapter the concept of the drag and reduction method known as the Aerospike is introduced, along with an explanation of its behavior, its drag reduction mechanism, the effective body shape and how it affects the flow stability, its heat reduction mechanism, along with how the addition of the aerodisk and the reattachment ring improve its overall performance. In order to look into the aerospike, an introduction of the physics used to analyze it is given, mainly the conservation, constitutive equations and dimensionless numbers and how they give shape to the dimensionless equations used in supersonic computer fluid dynamics, and a simple explanation of the physics of shock waves. Lastly, the main hypothesis is explained in detail along with the motivation of this analysis, where the practical uses of reduction methods studies such as this one and their importance is stated.

The second chapter presents the motivation, the main hypothesis behind this study, and finally the general and particular objectives of this thesis.

The third and fourth chapters consist of the code validation process, in which SU2, the simulation program used for this thesis, and the set of governing equations and turbulence model used in the following analyses are introduced, these being the compressible Navier-Stokes Equations and the RANS and SST models, respectively. Next, the chosen validation case, its meshed models and its study conditions are shown, along with its results in which a comparison between the experimental and simulated drag coefficients and shock wave shapes are presented. Then, a grid independence test is performed in order to show the quality of the designed meshes and explain why certain mesh sizes were chosen. Moving on, a design test is carried out to confirm that the designed aerospike and reattachment ring are working accordingly to what the literature indicates, where firstly the blunt body, spiked body and ringed body design and meshes are visualized, then the test conditions are shown, and finally the results are explained in detail, which consist of a drag coefficient plot, Mach Number, Pressure Gradient, body heat flux, and temperature flow visualizations and body surface

temperature plots of each body.

Lastly, a more detailed explanation of the reattachment ring is given, the main study of the thesis is performed, a comparison test of a blunt body, the blunt body with a spike, called spiked body, the spiked body with a reattachment ring, and another spiked body with a longer ring at a constant mach number and different angles of attack, where mainly the drag coefficients, surface temperatures, and body heat flux are described, compared and analyzed in-depth with the aid of the same flow visualizations performed in the design confirmation test, with the aim to clearly observe the performance of the reattachment ring at multiple angles of attack and determine when and how it stops reducing either the drag coefficient, the heat flux, or both.

At the end a conclusion of the whole analysis is given where the results of the study and their meaning are explained again in a shorter and simpler manner, along with a small explanation of further studies that could be done.

1 Introduction

1.1 Supersonic Flow

1.1.1 Conservation and Constitutive Equations.

The study of fluid mechanics in supersonic regime differs greatly from that in subsonic regime. Firstly, we speak of supersonic regime when a body travels through a fluid, or the fluid moves around the body in relative terms, at velocities higher than the corresponding sound velocity of the medium. Generally speaking, the more the velocity of the flow increases, the more relevant the changes in some important properties of the fluid become, mainly the density and viscosity, which at lower speeds can be simply considered constants. However, in supersonic flow this is no longer the case, as speed increases the flow's own inertia begins to compress the fluid, which in turn increases both its density and viscosity (in the case of gases). Successively, this results in equations that are almost trivial in subsonic flows, in terms of the flow's velocity field, becoming much more relevant. Essentially, the conservation of mass and conservation of momentum equations get linked to the conservation of energy equation, and consequently this means that it is not longer possible to solve one of them without simultaneously solving the other, which is in itself a problem because now there are more unknown variables than there are equations to find them. It is because of this that it is necessary to make use of other auxiliary equations, such as the constitutive equation of ideals gases.

Conservation equations for a Newtonian Fluid of variable density and viscosity in supersonic flow [3]:

- **Mass Conservation Equation:**

$$\frac{\partial \rho}{\partial t} + \frac{\partial}{\partial x_j}(\rho u_j) = 0 \quad (1)$$

- **Linear Momentum Conservation Equation, or Navier-Stokes Equation:**

$$\frac{\partial}{\partial t}(\rho u_i) + \frac{\partial}{\partial x_j} \left(\rho u_i u_j + p \delta_{ij} - \mu \left(\frac{\partial u_i}{\partial x_j} + \frac{\partial u_j}{\partial x_i} - \frac{2}{3} \frac{\partial u_k}{\partial x_k} \delta_{ij} \right) \right) = 0, i = 1, 2, 3 \quad (2)$$

- **Energy Conservation Equation:**

$$\frac{\partial}{\partial t}(\rho e_0) + \frac{\partial}{\partial x_j} \left(\rho u_j e_0 + u_j p + q_j - \mu u_i \left(\frac{\partial u_i}{\partial x_j} + \frac{\partial u_j}{\partial x_i} - \frac{2}{3} \frac{\partial u_k}{\partial x_k} \delta_{ij} \right) \right) = 0 \quad (3)$$

$$e = e_0 + \frac{u_k u_k}{2} \quad (4)$$

- **Ideas Gas Constitutive Equation, Fourier’s Heat Conduction Law, and thermodynamic properties relations:**

$$p = \rho RT \tag{5}$$

$$q_j = -k_c \frac{\partial T}{\partial x_j} \tag{6}$$

$$R = c_p - c_v \tag{7}$$

$$\gamma = \frac{c_p}{c_v} \tag{8}$$

$$e = c_v T \tag{9}$$

Where ρ is the fluid’s density, x_j are the coordinate system basis, u_j is the velocity, p es is the pressure, δ_{ij} is Dirac’s Delta, μ is the fluid’s dynamic viscosity, e_0 is the fluid’s total energy, e is the fluid’s internal energy, q_j is the heat flux, R is the fluid’s particular ideal gas constant, T is the temperature, k_c is the fluid’s thermal conductivity, c_p is the fluid’s specific heat at constant pressure, c_v is the fluid’s specific heat at constant volume, and γ is the heat capacity ratio, or adiabatic index.

1.1.2 Relevant dimensionless numbers and quantities

The previously presented equation can also be written in their dimensionless form in order to perform a better and simpler analysis with the help of the dimensionless terms that arise. When working with supersonic flows the most important ones are the following:

- **Mach Number Ma :** The Mach Number is a dimensionless number which represents the rate between the flow’s speed and the speed of sound of the medium, i.e. the fluid. In addition, the speed of sound is the speed at which a mechanical wave travels through a medium, thus the speed at which it transmits information, and therefore it depends on the properties of the medium itself. Consequently, in the study of Fluid Mechanics, this number speaks of how fast the flow travels with respect to the speed of sounds of its corresponding fluid, and more specifically, when it comes to the analysis of the flow around a geometry, it speaks of the speed of free flow, or the speed of the geometry.

Thus, the Mach Number directly indicates the flow regime in which one is working, for numbers lower than one we’re dealing with subsonic flow, where compressibility effects can be neglected, for numbers equal to one we are dealing with transonic flow, in which case shock waves start to appear and the compressibility effects start to become relevant for the flow analysis, for numbers greater than one, we speak of supersonic flow, where not only do shock waves appear, but also the heat

transfer analysis start to become more important for vehicle design and the flow's properties analysis, finally, when dealing with Mach Numbers greater than 5 we speak of hypersonic flow, where in addition to all the effects mentioned above, it's important to take into account the chemical composition of the fluid, mainly for heat transfer analysis, for instance, space shuttles enter earth's atmosphere at numbers greater than 25, and so, the air around them becomes ionized gas, which overheats the vehicle. [4]

$$Ma = \frac{u}{c} \quad (10)$$

Where Ma is the Mach Number, u is the characteristic velocity, and c is the medium's speed of sound.

- **Reynolds number Re :** The Reynolds number is a dimensionless number that represents the rate between the inertial forces and the the viscous forces, and thus serves to analyze how important the flow's viscous effects are, in other words, the flow's regime. For small numbers the regime is called laminar and the viscous effects are important, for greater numbers we say the regime is in transition and despite a lot of studies and efforts it still isn't fully comprehended, and finally for big numbers the regime is called turbulent, where the viscous effects have close to none relevance and the cinematic effects dictate most of the flow's behavior. [5] Note that the numbers are spoken of in relative terms as the exact numbers change in a case by case basis, depending mainly on the characteristic length.

$$Re = \frac{\rho u L}{\mu} \quad (11)$$

Where Re is the Reynolds number, u is the characteristic velocity, L is a characteristic length, for example the diameter of a cylinder immersed in a flow, and μ is the fluid's dynamic viscosity.

- **Prandtl number Pr :** Prandtl's number is a dimensionless number that represents the rate between the momentum transport capacity and the heat transport capacity of the fluid. Unlike the previously mentioned numbers, Prandtl's number does not depend on the flow's properties such as the velocity, but merely on the fluid's property, and is therefore an intrinsic property of the fluid. [5]

$$Pr = \frac{\nu}{\alpha} = \frac{c_p \mu}{k_c} \quad (12)$$

Where Pr is Prandtl's number, ν is the kinematic viscosity, α is the thermal diffusivity, c_p is the specific heat at constant pressure, μ is the dynamic viscosity, and k is the thermal conductivity.

Other relevant quantities in the study of supersonic flow, specifically in the study of external flows, are the drag and lift coefficients.

- **Drag Coefficient** c_D : This dimensionless quantity essentially speaks of the resistance of an object submerged in a fluid with the flow itself, meaning, it quantifies the friction force, or drag, generated between the flow and the object. It may seem like so but this coefficient is not a constant, in reality it is a function of the properties of the flow and the object, like the flow's speed, the fluid's density, the size of the object, among others. For this reason, it's not uncommon to find expressions of this coefficient in terms of Reynolds and/or Mach numbers, depending on the regime of the flow. Another aspect to note is that the drag coefficient contains within itself two types of drag, the form drag, which is the drag that occurs due to the mere geometry of the object, and the surface friction drag, which occurs due to the interaction of the object's surface and the flow.

$$c_D = \frac{2F_D}{\rho u^2 A} \quad (13)$$

Where c_D is the drag coefficient, F_D is the friction force experimented by the object, ρ is the fluid's density, u is the flow's velocity, and A a reference area of the object, which depends on the geometry one is working with. Due to the nature of the variables that define it, the drag coefficient is usually determined experimentally. [6]

- **Lift Coefficient** c_L : This dimensionless quantity is very similar to the drag coefficient, as it relates the lift forces experimented by a body with a certain geometry and surface submerged in a flow with certain properties, such as the Reynolds and Mach numbers, thus, in other words, it quantifies how good a body is at generating lift in a certain flow. The lift forces are forces that raise a body and they're generated by the pressure gradients present in the flow around the object, which in turn are formed by the geometry of the object, for instance, the wings of a plane generate a pressure difference such that the air pushes them up and thus lift the airplane.

$$c_L = \frac{2F_L}{\rho u^2 S} \quad (14)$$

Where c_L is the lift coefficient, F_L is the lift force experimented by the body, ρ is the fluid's density, u is the flow's speed, and S is an arbitrary reference surface of the object, which depends on the geometry with which one is working, and therefore, as with the drag coefficient, it's important to specify it along with the the coefficient's value for comparison purposes. This coefficient is also usually calculated experimentally. [7]

1.1.3 Shock Waves

One of the most important phenomena present in the supersonic regime are the shock waves. In a medium information travels through waves, properties such as the density, the pressure or the temperature, and these waves' speed is the well known speed of sound, which in turn depends on the medium's properties. As mentioned before, the supersonic regime takes place when the Mach number is greater than 1, that is to say, the flow, or an object submerged in it, moves at a faster speed than the speed of sound of the medium, meaning, the object travels and disrupts the medium faster than the information of these disruptions can. Therefore, the flow not being able to react to these disturbances fast enough to readjust to the immersed object, it instead gets suddenly compressed, thus generating a fast and big pressure change and therefore also a big change in the rest of the flow's properties, that is, this abrupt transition is the shock wave. Because it affects all the properties of the fluid the shock wave also represents a big discontinuity in the medium, and it's exactly from there that the complexity of its analysis arises, since fluid mechanics are based on the continuum medium theory, so certain considerations are made and new techniques used to analyze this type of flows.

One of the properties that suffers a considerable change, specifically an increase, in the shock waves is entropy, which together with the compression mentioned above implies that the heat flux along the shock waves is increased, which is why thermodynamic analysis is of great importance when studying supersonic vehicles, since the shock wave can collide and interact with object, and can even bounce in different areas of its geometry, and thus generate complex patterns in the temperature distribution in the vehicle. [8] [9] [10]

In general, the study of shock waves is of great importance in supersonic vehicle analysis, due to the complex interactions that can occur, however, despite of the many efforts made along the years in this topic, there's still no exact analytical method to determine neither their shape nor their position with respect to the object, even if fortunately we have come very close, as *J. Sinclair & X. Cui*, who through Newton's modified impact theory, and two geometrical reduction parameters for the subsonic region of the flow and for the shock wave separation distance, managed to obtain that determines the shock wave separation distance for a cylinder as a function of the free flow's Mach number and the location of the sonic point on the body's surface, and whose results agree quite nicely with the experimental ones. [11]

Consequently, because of the complications that these waves present for analytical methods, experimental methods for the visualization of supersonic flows and shock waves are of great importance. One of the optimal methods for these kind of analyses is the *Schlieren* visualization method, which is used to analyze flows with variable density. The implementation of this method involves the use of a single collimated light source to illuminate an object inside the flow, the refraction index variations in the medium cause by the pressure gradients distort the intensity of this illumination and subsequently allow the aforementioned variations in the fluid density, such as shock waves, to be clearly observed. [12]

In addition, many advancements and variations have been performed on this technique, such as the *direction-indicating color schlieren method (DInCS)*, which unlike the usual method that provides monochromatic images of one-dimensional gradients, it instead provides images of two-dimensional gradients through the use of colour; and others such as that of *T. Mizukaki* who instead of making the medium flow for it to interact with the object, shot the object into the fluid by designing an small experimental free-flight setup with a single-stage low-caliber gunpowder cannon, and obtained good results in comparison to the usual methods. [\[13\]](#)

1.1.4 Dimensionless Equations

Now then, the equations that dictate fluid mechanics can be rendered dimensionless, and in doing so the aforementioned dimensionless numbers arise in them, and thus these tell us, depending on the flow's properties, which terms of the equations become important and which become irrelevant. This is a common practice in the numerical simulation of fluids, because by removing these irrelevant terms from the calculations much computational time can be saved, and also, the greatest benefit is that one can compare their results with those of other experiments, even if their geometries, working fluid, velocities and/or temperatures, among others, are not the same.

Dimensionless conservation equations in supersonic flow for a Newtonian fluid of varying density and viscosity:

- **Mass Conservation Equation.**

$$\frac{\partial \rho}{\partial t} + \frac{\partial}{\partial x_i} [\rho u_i] = 0 \quad (15)$$

- **Linear Momentum Conservation Equation.**

$$\frac{\partial}{\partial t} (\rho u_i) + \frac{\partial}{\partial x_i} (\rho u_i u_j) + \frac{1}{\gamma Ma^2} \frac{\partial}{\partial x_i} p \delta_{ij} - \frac{2}{Re} \frac{\partial}{\partial x_i} [\mu S_{ij}] = 0 \quad (16)$$

$$S_{ij} = \frac{1}{2} \left(\frac{\partial u_i}{\partial x_j} + \frac{\partial u_j}{\partial x_i} - \frac{2}{3} \frac{\partial u_k}{\partial x_k} \delta_{ij} \right) \quad (17)$$

- **Energy Conservation Equation.**

$$\frac{\partial}{\partial t} (\rho e) + \frac{\partial}{\partial x_i} [(\rho e + p) u_i] - \frac{2\gamma Ma^2}{Re} \frac{\partial}{\partial x_i} [\mu S_{ij} u_j] - \frac{\gamma}{Pr Re (\gamma - 1)} \frac{\partial}{\partial x_i} \left[k_c \frac{\partial T}{\partial x_i} \right] = 0 \quad (18)$$

$$\rho e = \left(\frac{1}{\gamma - 1} \right) c_v \rho T + \gamma Ma^2 \frac{1}{2} \rho ||v||^2 \quad (19)$$

$$||v||^2 = (u_1^2 + u_2^2 + u_3^2) \quad (20)$$

1.2 Aerospikes

In vehicle design, mainly supersonic and hypersonic ones, there are two main objectives: to reduce the drag the vehicle experiences, and to reduce the heat transfer that occurs between the vehicle and the fluid. However, it is often the case that these two objectives are opposite to one another, a clear example can be seen when in the two main body types dealt with in fluid mechanics:

- **Blunt Bodies:** They are those bodies in which the drag is mainly composed of their pressure component. The drag they experience when immersed in a flow tends to be large, while the heat transfer is low since it can be distributed over a larger area.
- **Streamlined Bodies:** They are those bodies in which the drag is mainly composed of their friction component. The drag they experience when immersed in a flow is usually low, while the heat transfer is high since they have a smaller area to distribute it. [14]

In the case of supersonic and hypersonic vehicle design blunt bodies tend to be preferred, as heat peaks can damage the vehicle's material, the vehicle's electronic components which operate at a certain temperature range, and other components. However, this results in high drag forces, which leads to higher volumes of fuel to be transported and thus higher travel costs because of the fuel itself. It's for this reason that there exist multiple drag and heat reduction methods. [15]

1.2.1 Basic Mechanism

One of the simplest yet effective methods is the Aerospike method, which consists in placing a rod or cylinder, of fixed length, at the stagnation point of the blunt body. The Aerospike replaces the strong shock wave with a system of weaker shock waves, and it promotes the separation of the boundary layer from the body's surface. In addition, a layer called the Shear Layer is generated, which covers the body and surrounds a recirculation zone, where the flow reaches low pressure and velocity values, thus reducing both drag and heat transfer. This shear layer subsequently gets reattached to the rest of the flow at the body's shoulder, where the flow suffers a rapid and severe recompression which causes high pressure and heat transfer rates to be attained, meaning temperature peaks, however, this method results in less drag and heat transfer than in the original body. Furthermore, this shear layer orients the exterior flow parallel to the body's surface, this coupled with the drag and heat reductions can be seen as the body changing shape to a new effective body, much more aerodynamic than the original one. [15]: Now then, the aerospike does not come without its disadvantages, the main ones being:

- The aerospike tip suffers from large heat fluxes and therefore ablation.

- As mentioned before, high temperatures are reached at the shoulder of the body where the shear layer reattaches to the rest of the flow.
- Depending on the geometry, while the spike reduces drag, the heat flux could increase in comparison to the original geometry, so it's important to be careful when designing the spike.
- Clearly the spike implies an increase in weight for the vehicle.
- The spike is only effective if the blunt body generates an bow-shaped shock wave in front of itself, if the spike is long enough, in flows where the Mach numbers is greater than 1.2 [15], and at low angles of attack ($AoA < 9^\circ$) [19], which is why it's more advisable to use the spike on vehicles that perform few maneuvers.
- The spike moves the center of pressure upstream, which increases maneuverability but reduces the vehicle's stability.
- In the case of very long spikes, their structural rigidity must be taken into account for the design.
- For certain lengths of the spike, different instability modes can occur that generate fluctuations in pressure and heat.

Figure 1 shows clearly, thanks to the use of the Schlieren visualization technique, the decomposition of the shock wave that occurs thanks to the spike, in a) the blunt body can be seen with a clear bow-shaped shock wave, while in b) the decomposition of the wave can be appreciated. First we find an oblique foreshock, which can be conical or arc-shaped depending on the spike's geometry, then coming out of the spike's base is the shear layer, which surrounds the recirculation zone, where there are low velocity and pressure values which then gets reattached to the rest of the flow at the reattachment zone, where a great recompression occurs and thus a reattachment shock is formed, which is the cause of the temperature peaks at the body's shoulder.

Figure 2 shows in a) the normalized local pressures along the spike, and along the body surface in b), and it is in the latter that the sudden recompression of the flow at body's shoulder can be easily observed.

1.2.2 Aerodisk

Studies on spiked bodies date back to 1947, some of the first ones were done at the Langley Pilotless Aircraft Research, among them was the idea of the Aerodisk, also called Windshield at the time. Now, as it was already mentioned, one of the biggest problems aerospikes have is that its tip experiments large heat fluxes and ablation, besides the main cause of drag and heat reduction to the body is the expansion zone that covers the body, thus it was proposed to enlarge the spike's tip to increase the size of the expansion zone and protect the spike a bit more, this geometry is called an

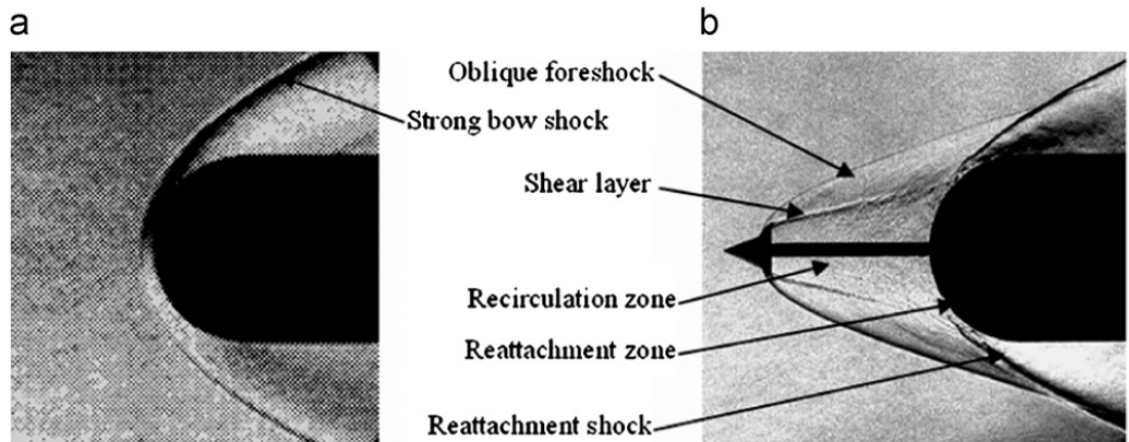


Figure 1: a) Blunt body's shock wave, b) Shock wave decomposition into a shock wave system in a spiked body. [15]

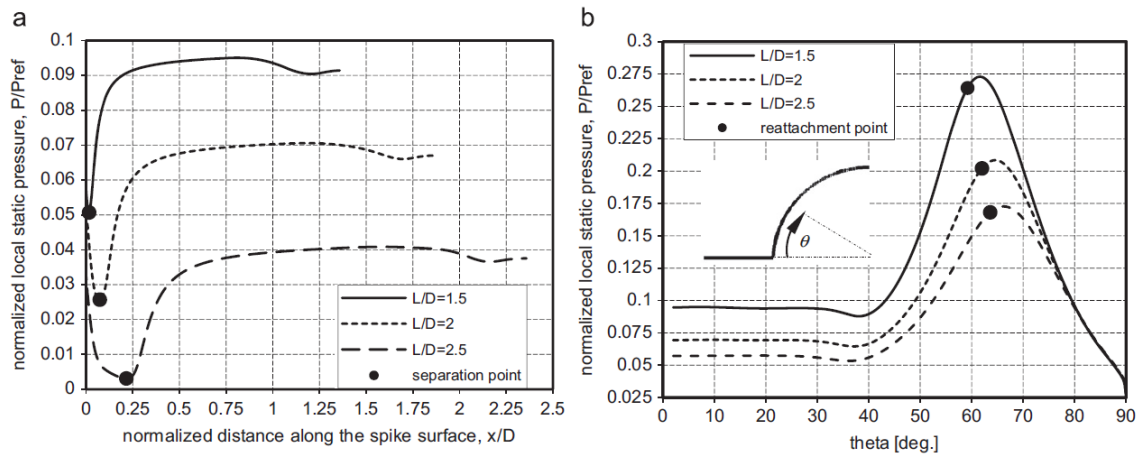


Figure 2: Normalized static local pressure. a) along the spike, b) along the body. [15]

Aerodisk. The aerodisk can have many different geometries, semi-spherical, conical, circular, among others, but in general it has the effect to further reduce the drag and heat flux, widening the range of angles of attack at which the spike is effective, and reducing heat and ablation at the spike tip. Figure 3 shows the configuration of a spike with an aerodisk.

1.2.3 Drag Reduction

The drag reduction that the body experiments thanks to spike can be simply explained by the fact that the recirculation zone covers most of the body from the free stream, besides, increasing the length of the spike causes the reattachment point to move down-

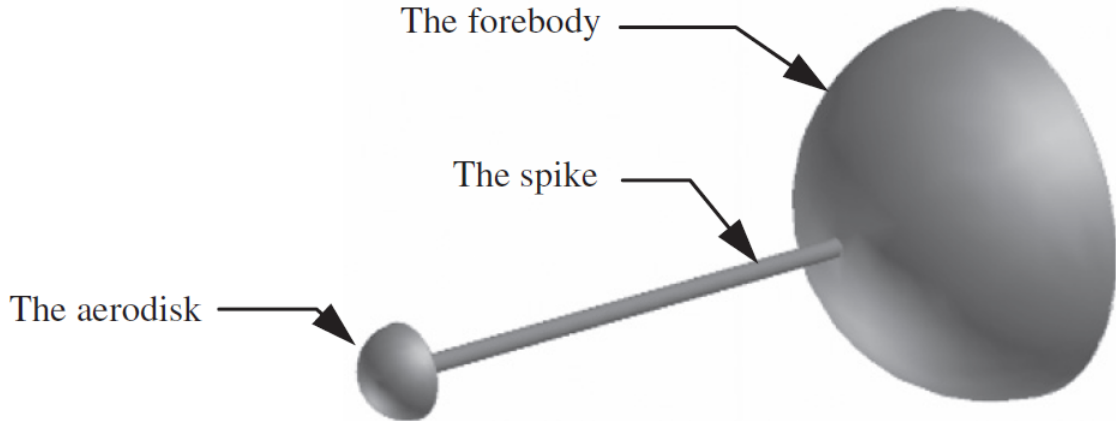


Figure 3: Diagram of a blunt body with a spike and an aerodisk at its tip. [15]

stream and the recirculation zone to expand even more, thus covering more of the body. The strength of the recompression shock wave is reduced when the reattachment point moves downstream, and so is the peak temperature and and pressure points. However, this explanation does not account for all the aspects of heat and drag reduction, because the increase in spike length reduces pressure everywhere, not just at the reattachment point, and the small change in the position of this point does not appear to be sufficient to explain the large decrease in peak pressure. It is for this reason that Ahmed et al. [15] implemented the concept of Effective Body, which is well established in the field of spiked bodies, and was introduced by Alexander SR., and it simply states that the blunt body is effectively transformed into a slimmer body due to the generation of the shear layer. This explanation was confirmed by Mair, who noticed that the flow outside of the shear layer is very similar to that of a conical body, so he compared the inclination angles of the separation shock against that of the shock ahead of a conical body with the same deflection as the shear layer, the angles turned out to be very similar, multiple other authors later confirmed the same idea [15].

1.2.4 Effective Body

Though it may be intuitive, defining the effective body shape by the shear layer is not accurate because its thickness can drastically change when the separation point moves, this being the point where the shear layer starts and the flow stagnates, furthermore, some of the shear layer streamlines go past the reattachment zone to merge with the rest of the flow and others turn around to go back to the recirculation zone, in fact only one stream line separates this two types of streamline and it was defined by Chapman et al. as the defining streamline, which at equilibrium links the separation point and the reattachment point, and in general determines the stability of the flow, this can be seen in Figure 4. This streamline is the only one that stagnates at the reattachment point

and as such Ahmed et al. suggest that it is more accurate to use it to define the effective body shape. To show these, in their paper they the flow of spiked bodies with different lengths and compared the inclination angles of their dividing streamlines and separation shock, with the theoretical analysis of the supersonic flow around conical bodies, and their results showed good agreement. [15] Furthermore, the inclination of this streamline dictates the strength of the separation shock and the pressure field after this shock, thus by increasing the length of the spike the effective body is rendered more slender. In addition, the expansion fan, or recirculation zone, reduces the pressure downstream of it, and accordingly the separation point shift due to an increase in the spike length also increases the expansion fan. Thus the length of the spike influences the pressure field on the whole body, in general by increasing the pressure is reduced, but as mentioned before, the longer it is the more one has to take into account its structural rigidity. [15] Now, as aforementioned, the aerodisk also affects the pressure field, this is because the separation point is located at its shoulder and thus an increase in disk's size pushes this point away from the body, and it also pushes the reattachment point further towards the forebody shoulder, in general turning the effective body more slender. Moreover, the expansion fan also increases as the angle of the dividing streamline is decreased, and more importantly, the effects of the strong bowed foreshock is almost limited to the surface of the disk as it shields the rest of the body. [15] Chapman et al. argued that the pressure along the dividing streamline governed the the pressure in the recirculation zone and stability of reattachment, such that for it to be stable the pressure inside the recirculation zone must equal the peak static reattachment pressure. Kenworthy proposed the concept of the energetic shear layer as a factor for the oscillation mode on spiked flat cylinder models. Ahmed et al. further expands this hypothesis, in general if the dividing streamline does not have enough energy in terms of pressure after the separation point, it gets closer to the spike and can even reattach to it, thus affecting the effective body, and as the streamline approaches the body the pressure rises and it ultimately manages to separates from the spike to spread towards the forebody. However, a high-pressure streamline (with enough energy) can continue directly to the reattachment zone to stagnate, resulting in a better defined body shape and a more stable shear layer. In this way, bigger aerodisk that results in a less inclined dividing streamline result in higher energy levels as it promotes the separation from the body surface. [15]

1.2.5 Heat Reduction

According to Holden (1966) [16], the value of peak aeroheating, that occurs on the shoulder, is dependent on the geometry of the recompression shock wave, the greater the angle between the normal to the body surface and the reattaching shear layer is, the greater the aeroheating is. In this way, if the spike length increases the reattachment point shifts towards the shoulder of the forebody and thus the aeroheating decrease, it is worth noting that the heat flux decreases on the whole body, not only on the reattachment zone. So, while the pressure peak is dependent on the reattachment

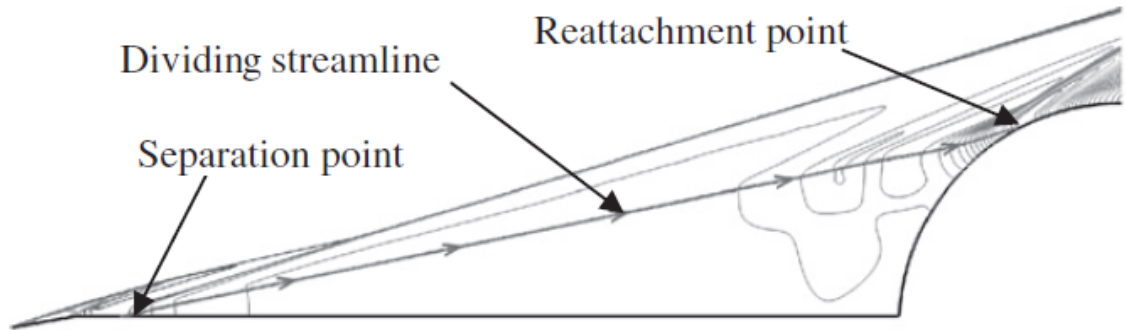


Figure 4: Dividing streamline details [15]

shock wave, the aeroheating peak is dependent on the impingement of the recompression wave on the body surface, and therefore the aeroheating peak can be used to locate the reattachment point. [15]

1.3 Reattachment Ring

The reattachment ring is a heat and/or drag reduction scheme specifically for spiked bodies, it was introduced by M. Elsamanoudy, who had the idea of mounting a ring on the shoulder of the blunt body, as seen in figure 5, with the purpose of reducing the heat peak that appears there due to the recompression shock wave. It also reduces the peak pressure and ergo the drag. However, it was noted that depending on the height of the ring it can be made to reduce heat more than drag or vice versa, as needed, making it a very versatile scheme. Its operation is the same as that of the spike, i.e., it decomposes the recompression shock wave from the body shoulder into a system of smaller waves, this can be seen in figure 6. However, work can still be done on optimizing the design of the ring at non-zero angles of attack as indicated by [2], information about the approximate range of angles at which the ring is effective or how the ring parameters affect it wasn't reported, so with this technique seeming so useful for spiked bodies, it is pertinent to analyze and look further into exactly the cases of non-zero angles of attack, specifically find out the effective angle range.

2 Motivation, hypothesis and objectives

2.1 Motivation

One of the fundamental problems in supersonic and hypersonic vehicle design is the constant struggle between drag and heat reduction, design the vehicle like a blunt body and it will have a greater surface area to distribute the heat but will inherently cause a lot of drag. On the other hand, design a more slender vehicle and it will have a lower

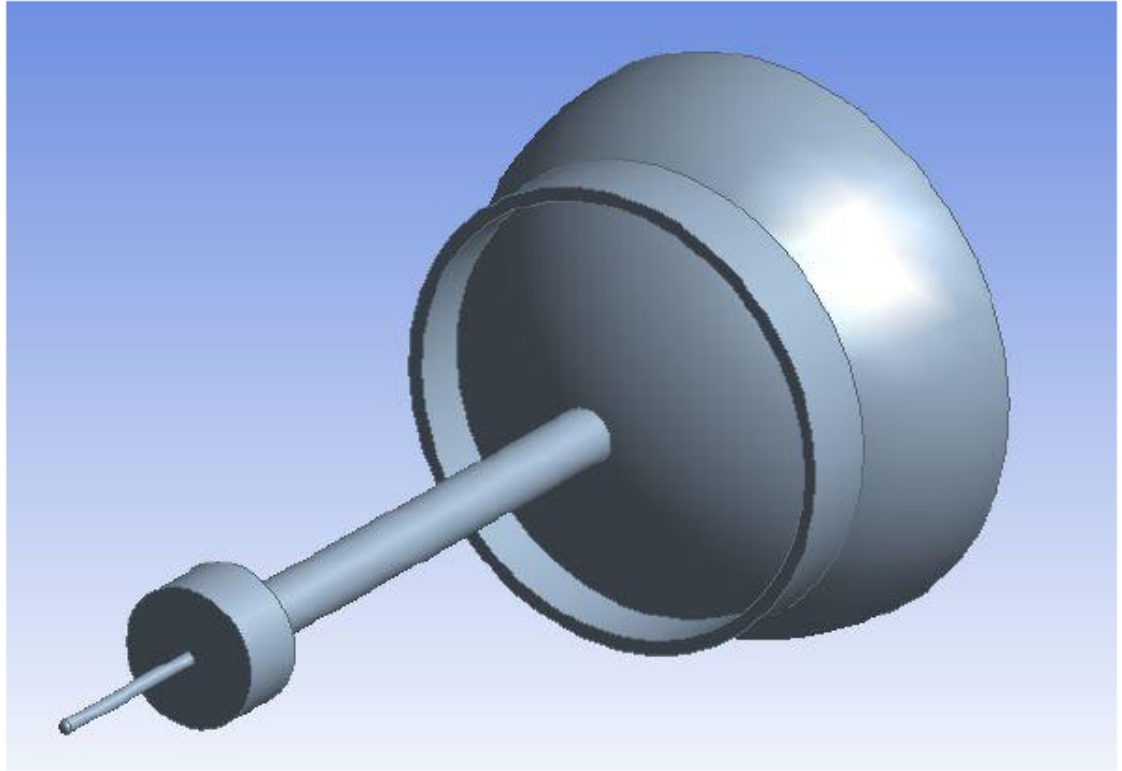


Figure 5: Diagram of the spiked body with a reattachment ring. [2]

drag coefficient but the heat will be more concentrated on the surface area thus provoking the vehicle to heat up, attaining both or either reductions is a difficult task which is why a lot of research is done regarding reduction methods. Furthermore, studying these reduction methods is important as they not only help improve the aerodynamic and thermodynamic performance, in turn they help reduce fuel load, material ablation on the vehicle's surface, risk of overheating of the vehicle components, flight time, and in general overall costs. Moreover, as time passes and technology develops, the aerospace industry becomes more and more important, and supersonic and hypersonic flight becomes more common, so all these reasons combined with the fact that one of the core philosophies of engineering is attaining the best performance with the least amount of the resources makes it clear that this is a crucial and ample field of study that needs to be analyzed with the purpose of obtaining better designs and making the industry progress as a whole.

2.2 Hypothesis

With all the previously presented information and knowing that the drag coefficient of spiked bodies correlates with the angle of attack due to the increment in projection

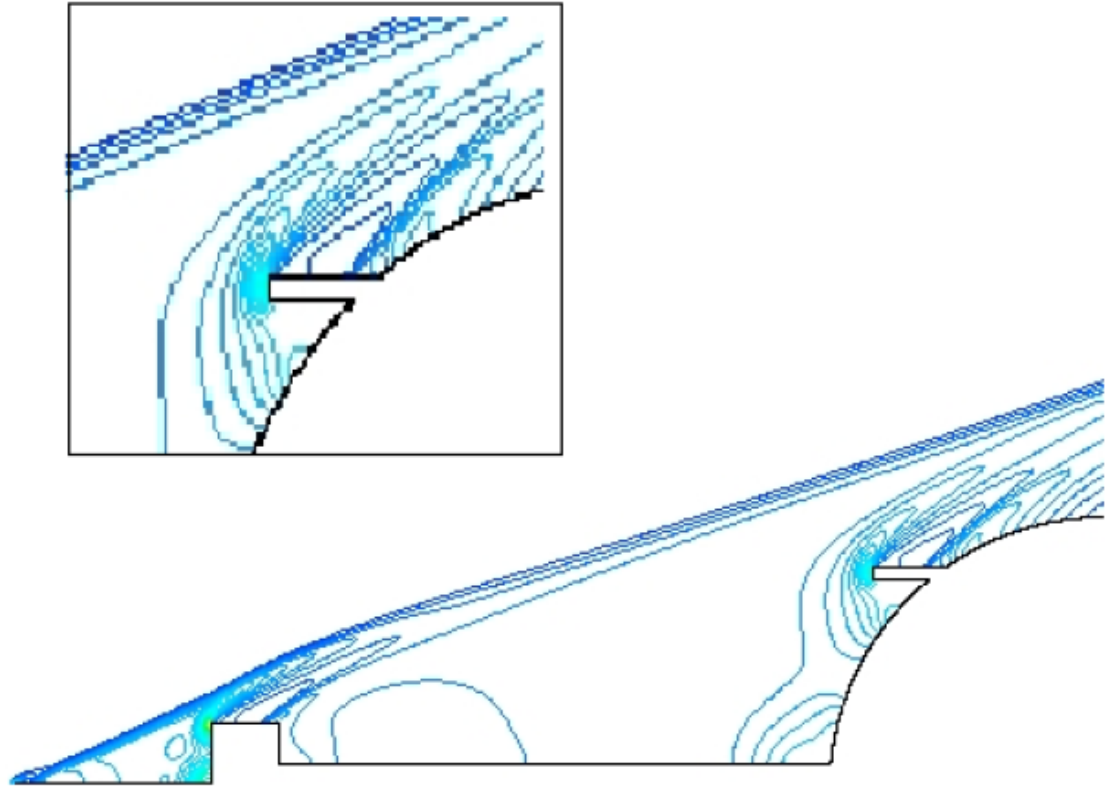


Figure 6: Decomposition of the shock waves due to the reattachment ring. [2]

area the aerospikes provoke, it can hypothesized that the reattachment ring will still reduce both drag and heat transfer in a certain angle of attack range as it will keep shielding the main body from the air flow, these reductions will be proportional to the ring's length as the longer it is the more surface it shields, however the angle of attack range at which the spike will provide these reductions will be inversely proportional to said length, as the longer the ring is the greater the projection area change, or drag, to angle of attach change ratio will be. When the angle of attack is greater than the mentioned range, the ring will start to cause worse drag coefficients and heat transfer, whether it will provide reductions in heat transfer and increments in drag coefficient or vice versa versa is unknown, but the ring will eventually become counterproductive when compared to the ring-less spiked bodies.

2.3 Objectives

General: To perform an aerodynamic and thermodynamic analysis of certain drag and heat transfer reduction methods on blunt bodies.

Particular:

- To analyze the effects the reattachment ring has as an auxiliary reduction method on the flow structure of a spiked blunt body.
- To study the reattachment ring’s effective angle of attack range at which it reduces the spiked blunt body’s drag coefficient and heat transfer.

3 Methodology

The software used to perform the simulations and validations in this study is the open-source software SU2. ”The SU2 software suite has been recently developed for the task of solving partial differential equation (PDE) analyses and PDE-constrained optimization problems on general unstructured meshes...the core of the suite is a Reynolds-averaged Navier-Stokes (RANS) solver capable of simulating the compressible, turbulent flows that are representative of many problems in aerospace and mechanical engineering.” [21]

3.1 SU2 Governing Equations

SU2 basically uses the same governing equations that were previously presented, the compressible Navier-Stokes equations, however, it is worth talking about how it models turbulence.

3.2 Turbulence Model

RANS

The Reynolds-Averaged Navier-Stokes Equations (RANS) are a form of the Navier-Stokes equations in which the steady-state solution is separated from the time-dependent fluctuations, which account for turbulence in different flow regimes. To derive this equations the Reynolds-decomposition techniques is used, in which the solution is split into a time-independent mean flow velocity and time-varying fluctuations about the mean, in other words [22]:

$$u(x, t) = \bar{u}(x) + u'(x, t) \tag{21}$$

Applying this decomposition to the Navier-Stokes equations and using the adequate properties and time-averaging operators one can obtain the following:

$$\rho \bar{u}_j \frac{\partial \bar{u}_i}{\partial x_j} = \rho \bar{f}_i + \frac{\partial}{\partial x_j} \left[-\bar{p} \delta_{ij} + 2\mu \bar{S}_{ij} - \rho \overline{u'_i u'_j} \right] \tag{22}$$

With the mean of the strain rate tensor:

$$\bar{S}_{ij} = \frac{1}{2} \left(\frac{\partial \bar{u}_i}{\partial x_j} + \frac{\partial \bar{u}_j}{\partial x_i} - \frac{2}{3} \frac{\partial \bar{u}_k}{\partial x_k} \delta_{ij} \right) \tag{23}$$

SST

SU2 makes use of multiple variants of the SST and SA turbulence models, in the case of these analyses the SST is employed. The Menter Shear Stress Transport Turbulence Model, or simply SST model, was developed by Menter to blend the accuracy of the $k - \omega$ model near the wall region, and the $k - \epsilon$ model for the far field conditions. This model is linear so it uses the Boussinesq assumption for the constitutive equation of the stress tensor:

$$\tau_{ij} = 2\mu_t S_{ij} - \frac{2}{3}\rho k \delta_{ij} \quad (24)$$

There are multiple variations of the SST model, here the Standard Menter SST Two-Equation Model will be presented. The k terms are interpreted as turbulence kinetic energy and the ω represent the rate of dissipation of eddies:

$$\frac{\partial(\rho k)}{\partial t} + \frac{\partial(\rho u_j k)}{\partial x_j} = P - \beta^* \rho \omega k + \frac{\partial}{\partial x_j} [(\mu + \sigma_k \mu_t) \frac{\partial k}{\partial x_j}] \quad (25)$$

$$\frac{\partial(\rho \omega)}{\partial t} + \frac{\partial(\rho u_j \omega)}{\partial x_j} = \frac{\gamma}{\nu_t} P - \beta \rho \omega^2 + \frac{\partial}{\partial x_j} [(\mu + \sigma_\omega \mu_t) \frac{\partial \omega}{\partial x_j}] + 2(1 - F_1) \frac{\rho \sigma_{\omega 2}}{\omega} \frac{\partial k}{\partial x_j} \frac{\partial \omega}{\partial x_j} \quad (26)$$

$$P = \tau_{ij} \frac{\partial u_i}{\partial x_j} \quad (27)$$

Where the turbulent eddy viscosity is:

$$\mu_t = \frac{\rho a_1 k}{\max(a_1 \omega, \Omega F_2)} \quad (28)$$

Each of the constants present in this equations are a blend of constants from the $k - \omega$ and $k - \epsilon$ models, as previously mentioned, and are blended via:

$$\phi = F_1 \phi_1 + (1 - F_1) \phi_2 \quad (29)$$

With additional functions:

$$F_1 = \tanh(\arg_1^4) \quad (30)$$

$$\arg_1 = \min \left[\max \left(\frac{\sqrt{k}}{\beta^* \omega d}, \frac{500\nu}{d^2 \omega} \right), \frac{4\rho \sigma_{\omega 2} k}{CD_{k\omega} d^2} \right] \quad (31)$$

$$CD_{k\omega} = \max \left(2\rho \sigma_{\omega 2} \frac{1}{\omega} \frac{\partial k}{\partial x_j} \frac{\partial \omega}{\partial x_j}, 10^{-20} \right) \quad (32)$$

$$F_2 = \tanh \arg_2^2 \quad (33)$$

$$\arg_2 = \max \left(2 \frac{\sqrt{k}}{\beta^* \omega d}, \frac{500\nu}{d^2 \omega} \right) \quad (34)$$

Where ρ is the density, $\nu_t = \mu_t/\rho$ is the turbulent kinematic viscosity, μ is the molecular dynamic viscosity, d is the distance from the field point to the nearest wall, and $\Omega = \sqrt{2W_{ij}W_{ij}}$ is the vorticity magnitude with $W_{ij} = \frac{1}{2}\left(\frac{\partial u_i}{\partial x_j} - \frac{\partial u_j}{\partial x_i}\right)$ [23].

NASA-Rumsey [23] also notes that it is recommended to use a production limiter, where the term P in the k -equation is resplaced by:

$$\min(P, 20\beta^*\rho\omega k) \quad (35)$$

The boundary conditions recommended are:

$$\frac{U_\infty}{L} < \omega_{farfield} < 10\frac{U_\infty}{L} \quad (36)$$

$$\frac{10^{-5}U_\infty^2}{Re_L} < k_{farfield} < \frac{0.1U_\infty^2}{Re_L} \quad (37)$$

$$\omega_{wall} = 10\frac{6\nu}{\beta_1(\Delta d_1)^2} \quad (38)$$

$$k_{wall} = 0 \quad (39)$$

”Where L is the approximate length of the computational domain,’ and the combination of the two far field values should yield a freestream turbulent viscosity between 10^{-5} and 10^{-2} times freestream laminar viscosity.” (NASA-Rumsey [23]).

Finally the constants are:

$$\gamma_1 = \frac{\beta_1}{\beta^*} - \frac{\sigma_{\omega 1}k^2}{\sqrt{\beta^*}}, \gamma_2 = \frac{\beta_2}{\beta^*} - \frac{\sigma_{\omega 2}k^2}{\sqrt{\beta^*}} \quad (40)$$

$$\sigma_{k1} = 0.85, \sigma_{\omega 1} = 0.5, \beta_1 = 0.075 \quad (41)$$

$$\sigma_{k2} = 1.0, \sigma_{\omega 2} = 0.856, \beta_2 = 0.0828 \quad (42)$$

$$\beta^* = 0.09, k = 0.41, a_1 = 0.31 \quad (43)$$

As previously mentioned, the model’s equations where consulted from NASA-Rumsey [23].

3.3 Validation Cases

In the following paragraphs all of the tests performed during this study will be presented, however, their respective results will be later shown in the Results section.

3.3.1 Code Validation

It was decided to replicate Shoemaker’s FL02D ([20]) validation case to in turn validate the SU2 code. In this case the numerical data of two models was compared against

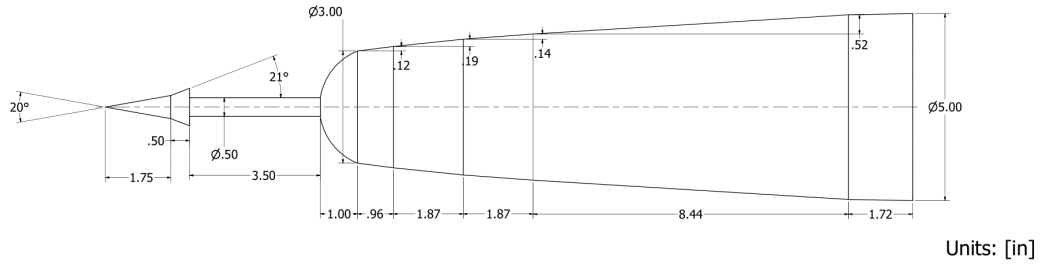


Figure 7: Geometry of the body with the Spiked-Windshield, dimensions in inches.

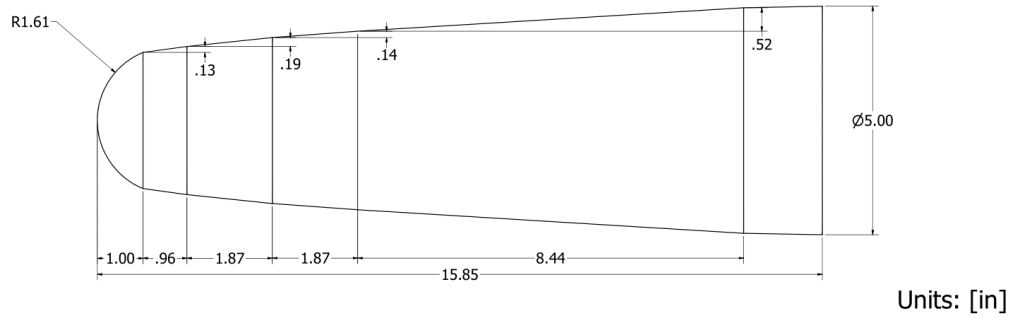


Figure 8: Geometry of the body with the circular nose, dimensions in inches.

Piland's ([24]) experimental data. The objects of study are blunt bodies with a spike-mounted windshield and a circular nose, for which the drag coefficient was calculated for Mach numbers between 0.8 and 1.8. The thermodynamic conditions of the freestream are sea-level pressure and temperature, and as for the boundary conditions, far field, constant wall-temperature, no-slip on the wall, and symmetry conditions were used, due to the figures having axial symmetry. This shortens the simulation time, and the literature indicates it is safe to assume the flow is symmetrical for spiked bodies [15]. The fluid used was air with $\gamma = 1.4$ and $R = 287.058 [J/kg \cdot K]$. The RANS solver and SST turbulence model were set up along with a null angle of attack. The two geometries can be seen in figures 7 and 8, and were drawn using Autodesk Inventor Professional 2024, a computer-aided design application for 3D mechanical design, simulation, visualization, and documentation developed by Autodesk, with a student license provided by the National Autonomous University of Mexico [29].

T_∞	288.15 [K]
P_∞	101,325 [Pa]
γ	1.4 [1]
R	287.058 [J/kg·K]
AoA	0 [1]

Table 1: Validation Test Conditions

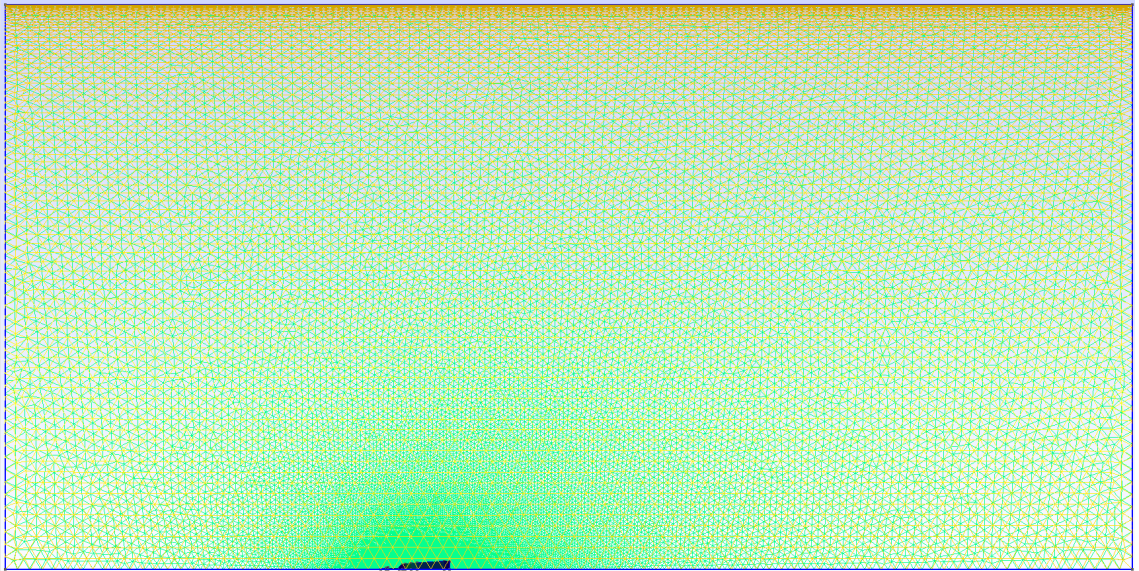


Figure 9: Side view of the Spiked Windshield’s 2D mesh.

3.3.1.1 Mesh

The geometries on figures 8 and 9 were replicated and meshed in Gmsh [25], an open source 3D finite element mesh generator. For the Spiked Windshield three mesh sizes were used, 0.1 [m] for the nodes far from the profile, 0.001 [m] for the nodes on the front of the body as they are near where the system of shockwaves appear, so a smaller size is needed to capture the sudden and big changes caused to the fluid’s properties these shockwaves provoke, and finally 0.002 [m] for the nodes on the back of the profile, meaning downstream of the body’s shoulder, because a good refinement is not needed here as there are no considerable changes or effects that need to be captured. In total this mesh in 3D has 756449 nodes and 4675535 elements, and it can be seen in figures 9 and 10, rendered only in 2D for the purposes of visualization. The whole domain is 4.5 [m] tall and 9 [m] long, which can be seen in figure 11.

In contrast, for the circular-nosed blunt body only two mesh sizes were needed

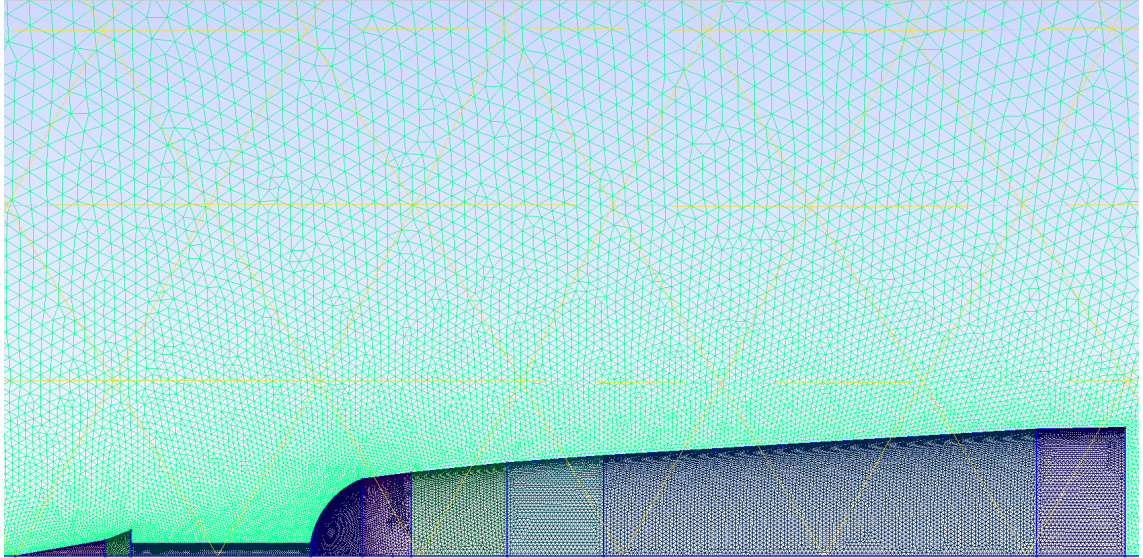


Figure 10: Zoomed side view of the Spiked Windshield's 2D mesh.

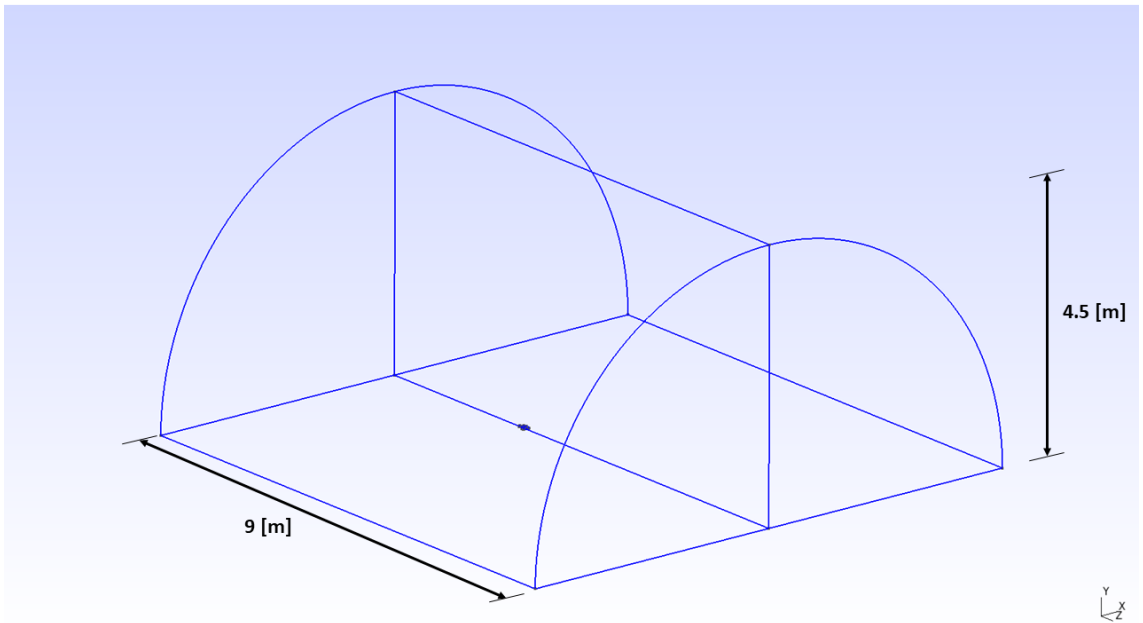


Figure 11: Computational domain's geometry.

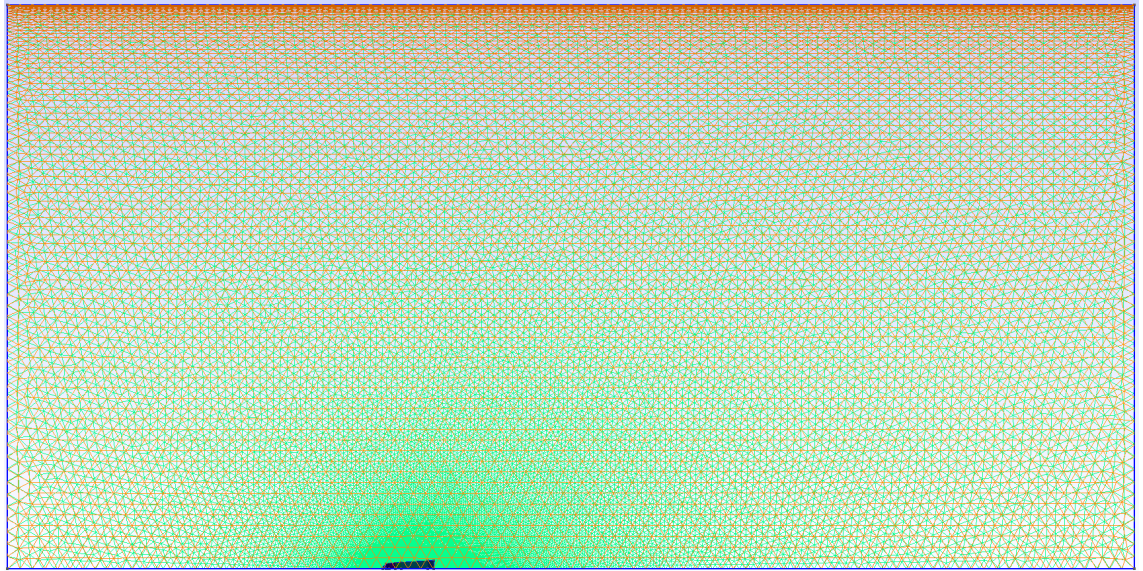


Figure 12: Side view of the Blunt body's 2D mesh.

since just one shockwave appears, so 0.1 [m] for the nodes far from the body and 0.002 [m] for the ones near it. In total this mesh in 3D has 653209 nodes 4039367 elements, and it can be seen in figures [12](#) and [13](#) rendered in 2D for the purposes of visualization. The domain size is the same as the previous one, 4.5 [m] tall and 9 [m] long (figure [11](#)).

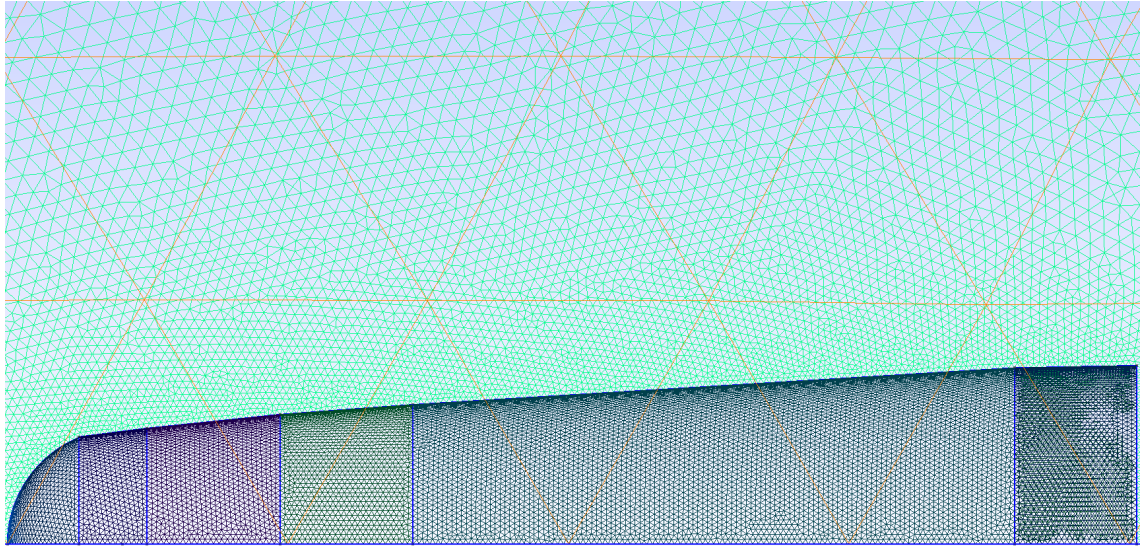


Figure 13: Zoomed Side view of the Blunt body's 2D mesh.

3.3.2 Grid Independence Test

Before explaining the simulation design and the conditions they were performed in, a grid independence test was made to ensure good results while not causing the simulations to take too long for a barely noticeable change in said results. For this test a different profile than that of the validation test was designed, a spiked blunt body with an aerodisk was decided upon, as a blunt body would be too simple compared with the more complicated designs of the ringed bodies that would later be tested, and a spiked blunt body with a ring would be more complex than necessary without really giving much benefits to the test. The geometry of this body can be seen in figure 15, its mesh in figure 20, and a zoomed in view of said mesh in figure 21.

In total, 6 different mesh designs were tested, 2 considered coarse, 2 considered to be of medium size, and 2 considered to be refined. The computational domain has the same size in all of them and it also coincides with that of the validation test, meaning it's 4.5 [m] tall and 9 [m] long (figure 11). In these meshes there are 3 important mesh sizes, one constant and two that differ among the meshes and characterize them, the normal size called tm , which is 0.1 [m] for all the meshes, the refined size called tmr , and the box size called tmb . The normal size is the biggest size and it's the default size for the computation domain, the refined size is the smallest size and is used on the body surface nodes as the effects close to the body need to be captured correctly, and finally the box size which is 1.5 times the size of the refined size and it's used in a box-shaped space around the body with the aim to capture the effects of the shock waves near the body surface correctly. This box-shaped space covers from the -0.012 [m] coordinate to the 0.2 [m] coordinate in the x axis, from the 0 [m] coordinate to the 0.07 [m] coordinate in the coordinate in the y axis, and from the -0.07 [m] coordinate to the 0.07 [m] coordinate in the z axis. It's worth mentioning that the minimum y-coordinate is 0 [m] because the mesh is to be used with a symmetry condition in the $y = 0[m]$ plane. These different sizes, except for tm as it is constant, the number of nodes and the number of elements for each of the meshes is presented in table 2.

As for the simulation properties themselves they were pretty similar to the validation test, the fluid was air at sea-level atmospheric conditions: $\gamma = 1.4[1]$, $R = 287.058[J/kgK]$, $P_\infty = 101,325[Pa]$, $T_\infty = 288.15[K]$. The boundary conditions were no-slip at the wall, constant wall temperature of 300[K], far field, and symmetry. RANS was used as the solver and SST as the turbulence model. What mainly changed was the body, and consequently the Reynolds Number, its reference length, and the reference area, which were 3464570.0 [1], 0.1 [m], and 0.007854 [m^2] respectively. Lastly all the tests were carried out with Mach Number of 1.8 and with a null angle of attack.

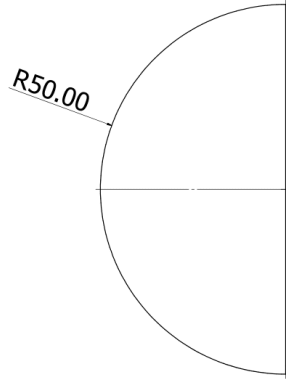
3.3.3 Mesh Design and Ringed Body Confirmation Test

For the main study, four different meshes were designed, one of the simple blunt body, one of the spiked blunt body with a hemispherical aeroshield, one of this same spiked blunt body with a reattachment ring, and lastly one of this same spiked blunt body but with a longer reattachment ring. The blunt and spiked blunt bodies were designed and

Mesh	t_{mr} [m]	t_{mb} [m]	# of nodes	# of elements
Coarse 1	0.009	0.0135	396901	2460816
Coarse 2	0.007	0.0105	404448	2507071
Medium 1	0.004	0.006	464066	2879343
Medium 2	0.003	0.0045	477966	2965092
Refined 1	0.00096	0.00144	1055506	6564303
Refined 2	0.00086	0.00129	1250095	7779659

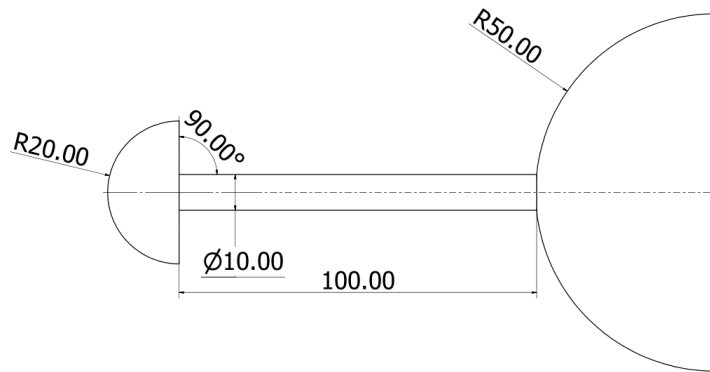
Table 2: Mesh sizes, number of nodes, and number of elements of each of the mesh designs.

simulated for simple comparison reasons, the blunt body as a full reference basis and the spiked body to mainly compare the ringed bodies to, meaning with the objective of knowing when the rings bring more disadvantages rather than advantages when there's an angle of attack, when compared to the body not having them and having only the spike. As to why two ringed bodies were made, this was done with the purpose of understanding how the length of the rings affect the drag coefficient, the body's surface temperature, and the heat transfer. A spike with an aerodisk was chosen as it is well known in the literature that they're better than a simple aerospike in both drag and heat reduction terms, and its hemispherical shape is due to the fact that spikes with rounded shoulder are less prone to suffer flow instabilities [15], and studying them is not within the purposes of this thesis. From this point forward the spikeless blunt body will be referred to as Blunt Body, the ringless spiked blunt body as Spiked Body, the spiked blunt body with the shorter ring as Ring 1, and lastly the spiked blunt body with the longer ring as Ring 2. Their geometries can be seen in figures [14] to [17], and were also drawn using Autodesk Inventor Professional 2024. The computational domain size of these 4 meshes was the same as the one of the previous ones, 4.5 [m] tall and 9 [m] long (figure [11]), and just like the mesh independence test mesh these meshes are surrounded by a box-shaped space, ranging from the -0.07 [m] coordinate to the 0.07 [m] coordinate in the x axis, from the 0 [m] coordinate to the 0.07 [m] coordinate in the coordinate in the y axis, and from the -0.012 [m] coordinate to the 0.08025 [m] coordinate in the z axis. This box technique is again used with the purpose of capturing the effects of the shock waves near the bodies' surfaces. For all meshes the default mesh size of the computational domain was $t_m = 0.1$, the size close to the body surface $t_{mr} = 0.00096$, and the size inside the boxed space was 1.5 times that of the size on the body surface $t_{mb} = 0.00144$. The design of these bodies can be seen in figures [14] - [17], and their respective meshes in zoomed in and zoomed out views in figures [18] - [25].



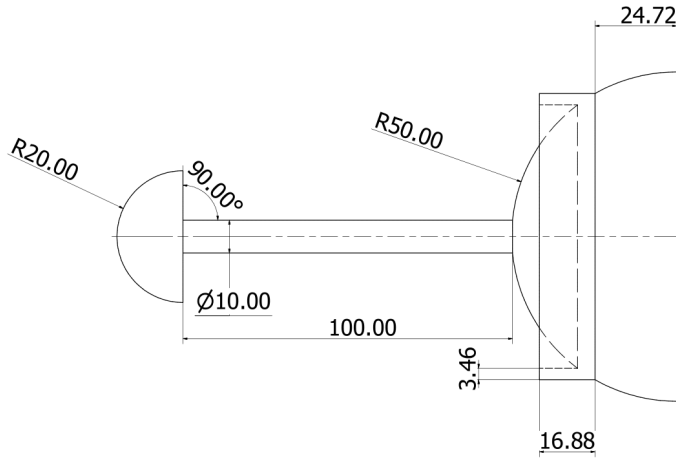
Units: [mm]

Figure 14: Geometry of the Blunt Body.



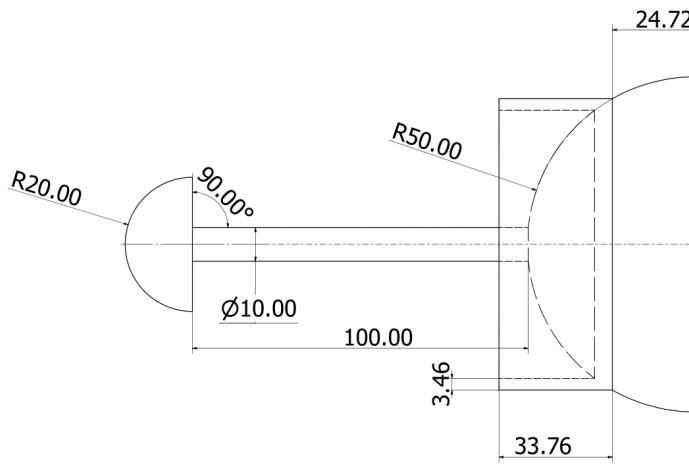
Units: [mm]

Figure 15: Geometry of the Spiked Body.



Units: [mm]

Figure 16: Geometry of the Ring 1 Body.



Units: [mm]

Figure 17: Geometry of the Ring 2 Body.

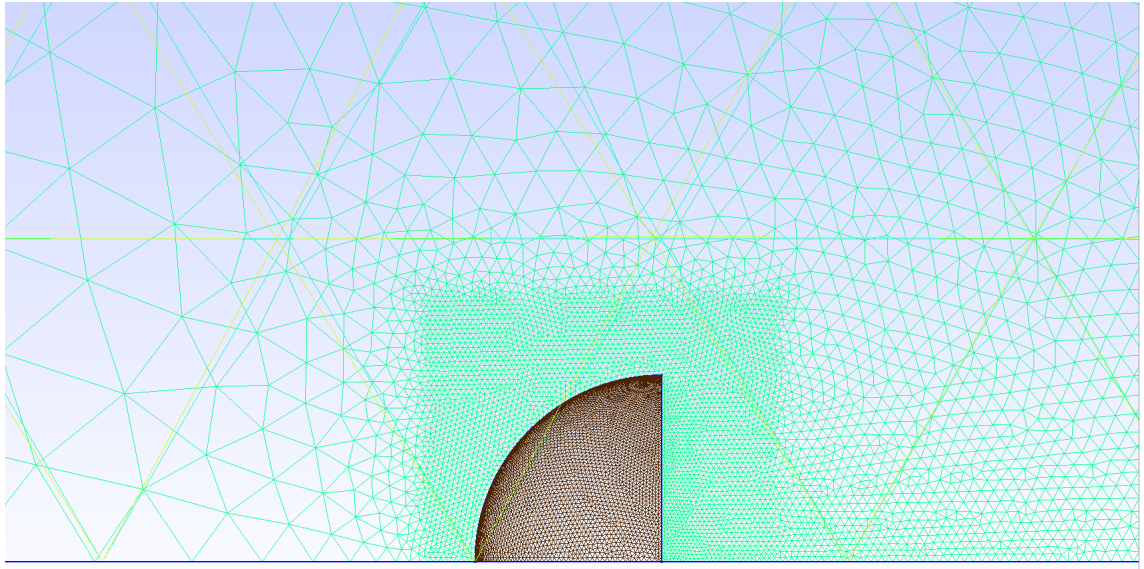


Figure 18: Side view of the blunt body mesh, meshed in 2D and zoomed in for visualization purposes.

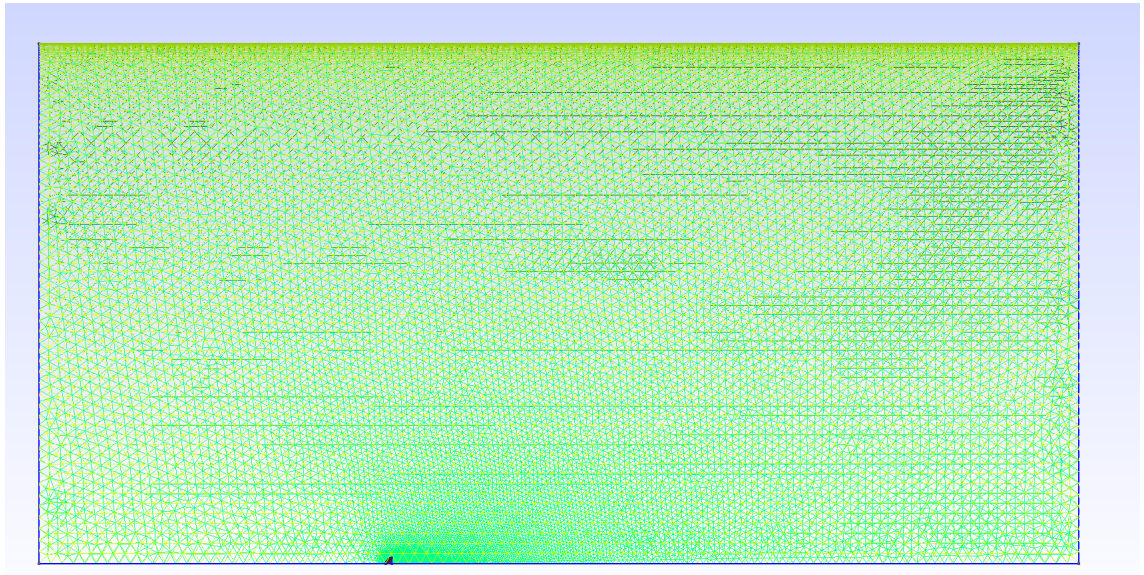


Figure 19: Side view of the blunt body mesh, meshed in 2D and zoomed out for visualization purposes.

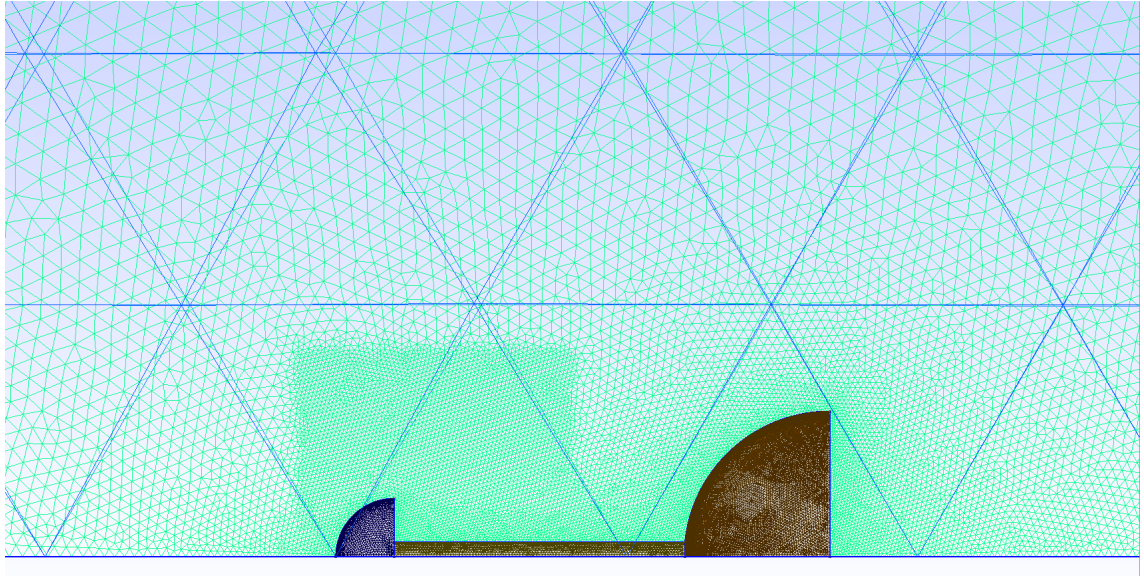


Figure 20: Side view of the spiked body mesh, meshed in 2D and zoomed in for visualization purposes.

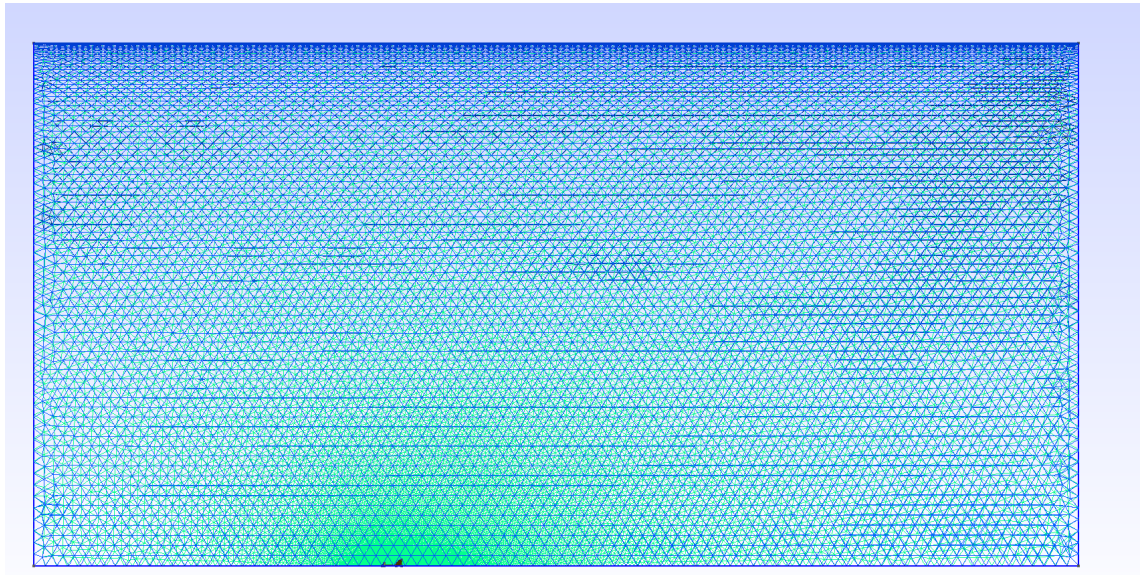


Figure 21: Side view of the spiked body mesh, meshed in 2D and zoomed out for visualization purposes.

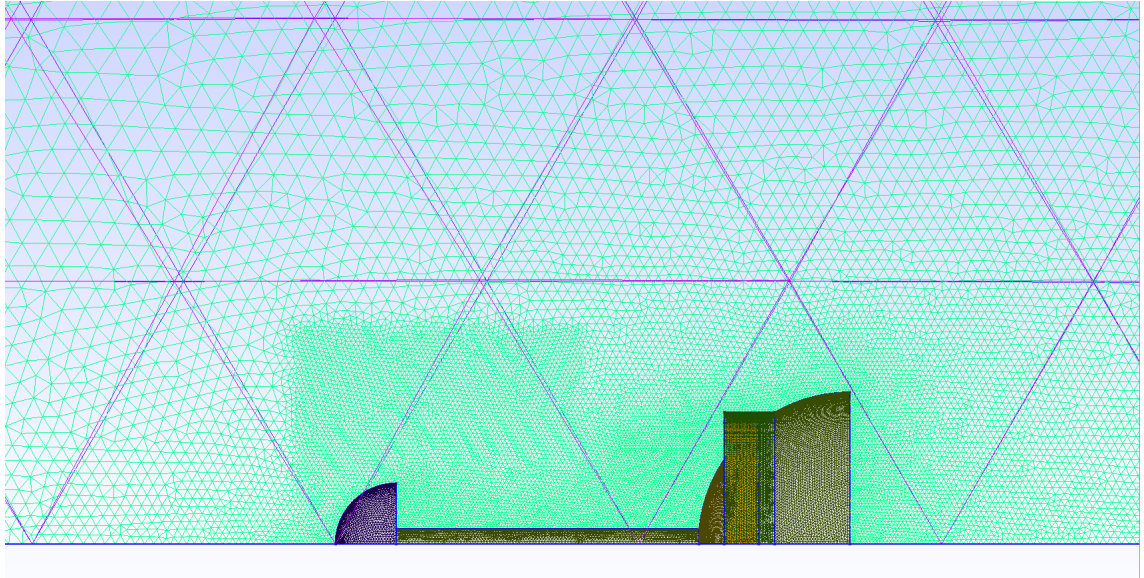


Figure 22: Side view of the short ring body mesh, meshed in 2D and zoomed in for visualization purposes.

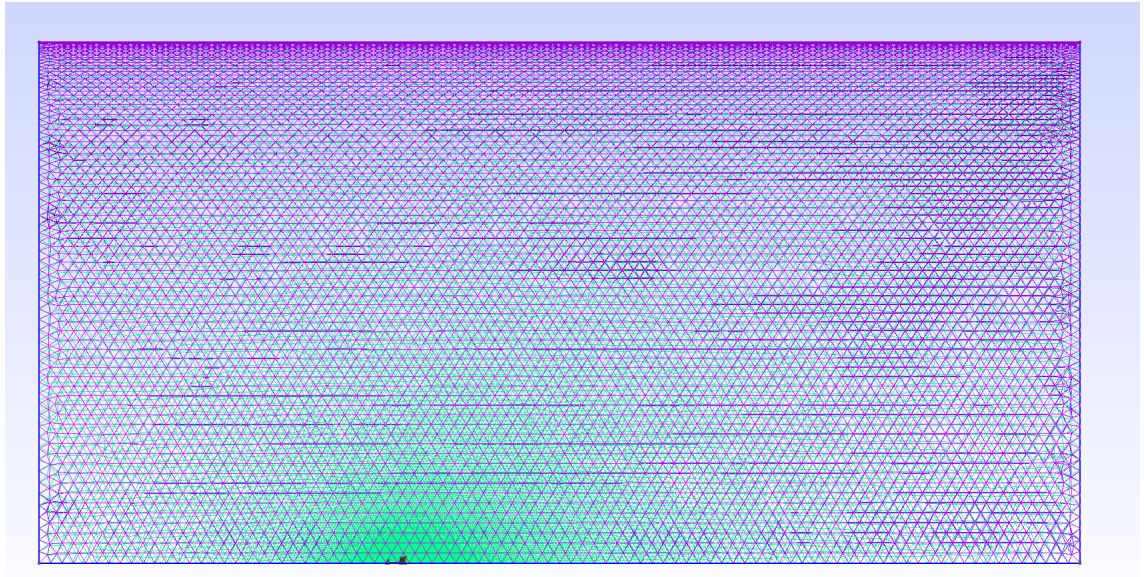


Figure 23: Side view of the short ring body mesh, meshed in 2D and zoomed out for visualization purposes.

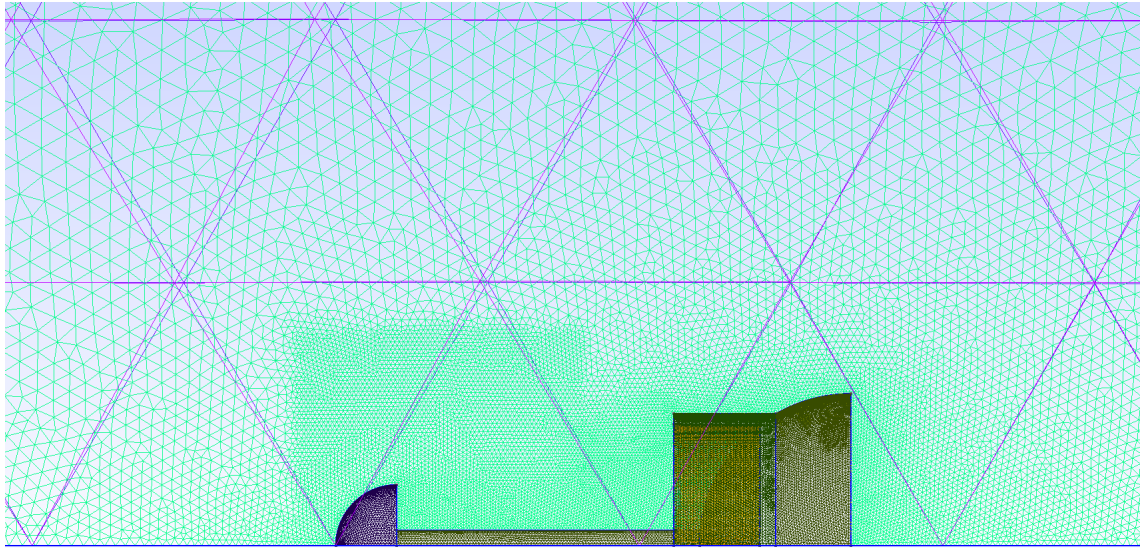


Figure 24: Side view of the long ring body mesh, meshed in 2D and zoomed in for visualization purposes.

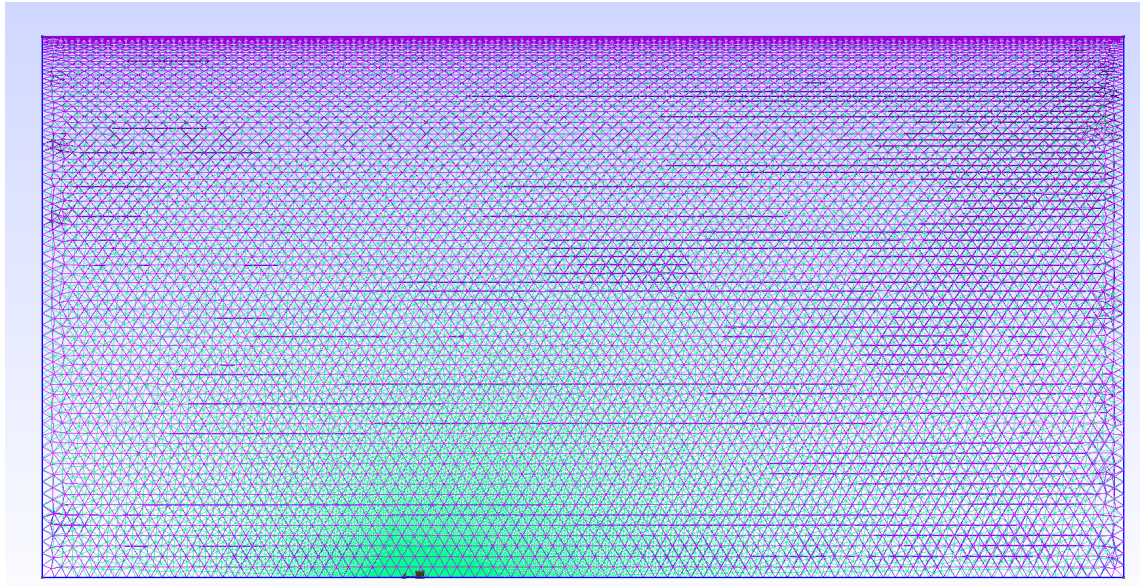


Figure 25: Side view of the long ring body mesh, meshed in 2D and zoomed out for visualization purposes.

Before performing the main study simulations, a simple test was done to ensure the ring was designed properly. The blunt body, the spiked blunt body, and the short ringed body were tested at the according atmospheric conditions of a 25,000 [m] altitude, to simulate more realistic conditions for a supersonic vehicle, these freestream properties can be found in table 3, these values were calculated using the international standard atmosphere model [27], and Sutherland’s law. The models were tested at Mach numbers 1.6, 1.8 and 2.0, the Reynolds length was the body diameter $D = 0.1[m]$, as it is customary in the literature, the corresponding Reynolds number to each Mach number can be found in table 4. Again the boundary conditions were no-slip at the wall, constant wall temperature of 300[K], far field, and symmetry on the $y = 0[m]$ plane. RANS was used as the solver and SST as the turbulence model, a constant Prandtl number was set as the conductivity model. The reference areas used are:

- Blunt Body: 0.0039263 [m²]
- Spiked Body: 0.00451547 [m²]
- Ringed Body: 0.00451557 [m²]

γ	1.4[1]
R	287.058[J/kgK]
P_∞	2,488.367[Pa]
T_∞	216.65[K]
ρ	0.04001[kg/m ³]
c_∞	295.06[m/s]
μ	$1.422 \cdot 10^{-5}$ [Pa · s]
k_c	0.0194[W/(m · K)]
Pr	0.7375[1]

Table 3: Atmospheric conditions for a 25000 [m] altitude.

3.3.4 Reattachment Ring at multiple angles of attack

As previously mentioned, the reattachment ring was first implemented by Elsamanoudy et al. [2], it was devised to alleviate the high heat experimented at the shoulder of a spiked blunt body caused by the recompression shock wave, also known as reattachment shock wave. Now, as a simple reminder of the drag and heat reduction mechanisms of a spike with an aerodisk, the spike decomposes the strong bow shock wave of a

Ma [1]	Re [1]
1.6	132,888.21
1.8	149,499.24
2.0	166,110.26

Table 4: Reynolds number and freestream speed corresponding to the different Mach numbers.

blunt body into a system of weaker shock waves and promotes the separation of the boundary layer, this creates a recirculation zone in which low pressure and speed values are attained, the aerodisk causes an adverse pressure gradient which further induces the expansion of said recirculation zone, resulting in a sort of protecting screen for the blunt body which averages it out to more streamlined effective body. However, one of the weaker shock waves, the shear layer, eventually rejoins the flow outside of the expansion zone at the shoulder body and suffers a sudden recompression which results in another shock wave, this shock wave impinges on the surface of the body causing a high heat transfer. Thus, as one can see, one of the main disadvantages of this reduction technique is this recompression shock wave, so the logical next step would be to prevent its impingement on the body surface, and there's probably multiple ways to do this, but the simple and elegant solution Elsamanoudy et al. (2013) found was to use the already present mechanism that breaks the impact of a shock wave, the aerospike, however they needed something that would break the shock wave all around the surface of the blunt body, so they came up with a ring located at the zone of reattachment where the peak heat transfer value is found. And so the reduction mechanism of the reattachment ring is exactly that of the aerospike, it breaks the reattachment shock wave into a system of smaller shock waves consequently reducing the aeroheating. Elsamanoudy et al. (2013) also found that the ring enlarged the recirculation zone, further reducing the overall drag of the body, attaining drag coefficients reductions of up to 69.82%. Elsamanoudy et al. also (2013) thought of experimenting with the ring's length, they tested one ring with a length of $h = 0.1D$ (where h is the length of the ring, and D is the diameter of the blunt body), and another one with $h = 0.5D$, and found that the body with the longer ring had a higher drag coefficient, due to part of the flow on the recirculation zone that tries to go upstream being trapped in the cavity formed by the ring and exerting a mainly axial pressure force on the surface of the body, while the body of the shorter ring also experiences pressure forces on the surface of the blunt body but its dominant component is radial. However, this body with the longer ring also experienced lower values of heat flux along most of the blunt body part due to the temperatures near the body surfaces being very close to those of the wall. These results can be seen in images [26](#) and [27](#) respectively. These results led to the conclusion that while the reattachment ring can cause both heat and drag reductions, its length can be adjusted

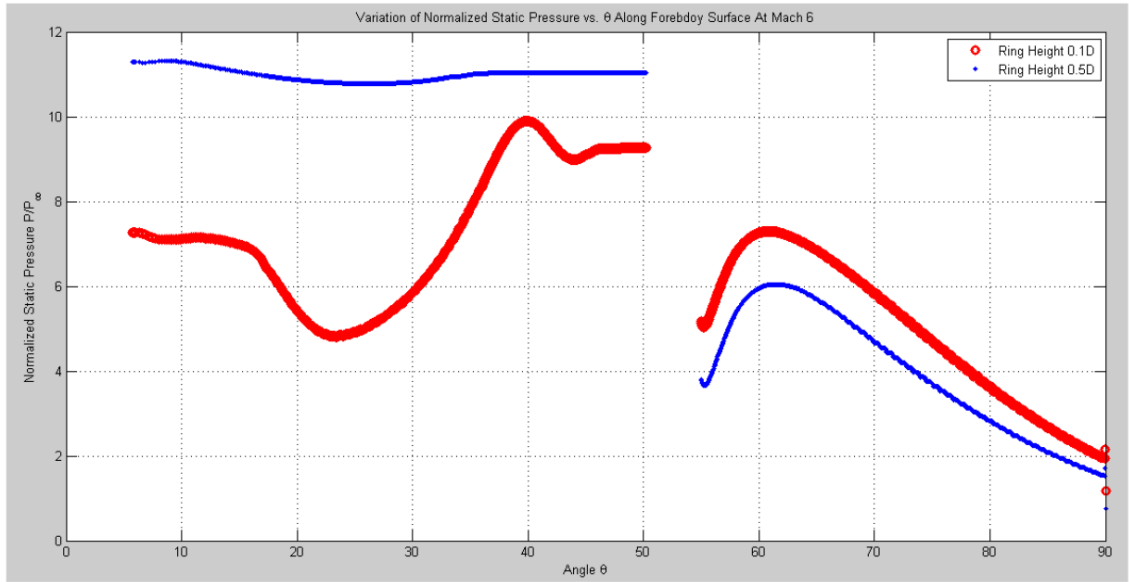


Figure 26: Elsamanoudy’s [2] Static Pressure along the hemisphere surface for $h = 0.1D$ & $h = 0.5D$ at Mach 6.

to increase the reduction of drag while lessening the reduction of heat, and vice versa, thus making its design versatile for different requirements. However, in this article [2] there is no mention of the performance of the ring in the supersonic regime (as it was only tested in the hypersonic regime), nor its performance at non-zero angles of attack, it is even stated in the recommendation chapter that ”The reattachment ring concept needs further research to optimize its performance, and in particular, its performance at non-zero angles of attack.” (Elsamanoudy et al. [2]), and so that is exactly the main topic of this thesis, investigating the performance of the ring at multiple angles of attack in the supersonic regime and the effects the variation of its length provokes in said performance.

As it was stated before, the main objective of this thesis is to analyze the performance of the reattachment ring at different angles of attack. To test this, the four meshes mentioned in the previous section were designed, one of the blunt body for overall reference, one of the spiked body to compared the ringed bodies to, and two ringed bodies, one with a shorter ring and one with a longer ring, in order to study the effects of the ring’s length on the performance at different angles of attack. These four meshes were tested at a constant Mach number of 2.0, the reasons for this are the fact that most spiked bodies studies are done at hypersonic speeds ($Ma > 5$) and most importantly that the study made by Elsamanoudy et al. [2] was performed at Mach numbers of 6, 8 and 10, so it’s worth studying the ring at lower Mach numbers. The angle of attack was changed at constant intervals of 1, but this interval changed later on when greater angles where reached as it was clear that the drag coefficient did not change too much for such small intervals, and in order to reduce the number of simulations and

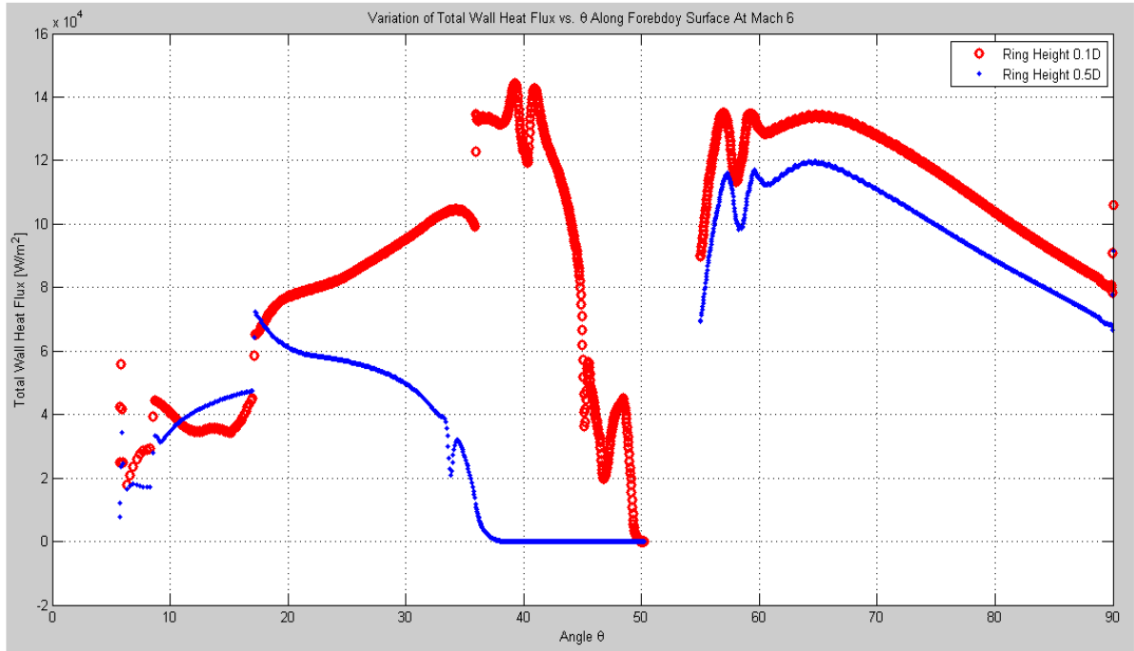


Figure 27: Elsamanouidy’s [2] Total heat flux along the hemisphere surface for $h = 0.1D$ & $h = 0.5D$ at Mach 6.

their corresponding convergence time. Just as in the previous section, the atmospheric conditions were those of a 25,000 [m] altitude and are presented in table [5], the Reynolds length was the body diameter $D = 0.1[m]$, and its corresponding Reynolds number can be found in the same table. The boundary conditions were no-slip at the wall, constant wall temperature of 300 [K], far field, and symmetry on the $y = 0[m]$ plane. RANS was used as the solver, and SST as the turbulence model, a constant Prandtl number was set as the conductivity model. The reference area for each body for each angle of attack was calculated by SU2, which does it by projecting the body onto the $z = 0[m]$ plane, and are presented in table [6], it’s worth noting that these areas are only halves of the real areas due to the presence of the symmetry condition. Finally, it’s also worth noting that the angles of attack are made with respect to the y axis, as if the $y = 0[m]$ plane was rotated, so with the perspective of the body rotating, its x and z coordinates would change while its y coordinates would remain constant.

γ	1.4[1]
R	287.058[J/kgK]
P_∞	2,488.367[Pa]
T_∞	216.65[K]
ρ	0.04001[kg/m ³]
c_∞	295.06[m/s]
μ	$1.422 \cdot 10^{-5}$ [Pa · s]
k_e	0.0194[W/(m · K)]
Pr	0.7375[1]
Ma	2.0[1]
Re_D	166110.26[1]

Table 5: Atmospheric conditions for a 25000 [m] altitude.

	Reference Areas [m^2]			
Angle of attack [$^\circ$]	Blunt Body	Spiked body	Ringed body 1	Ringed body 2
0	0.0039263	0.00451547	0.00451557	0.00451568
1	0.00392555	0.00452281	0.00454262	0.00456719
2	0.00392415	0.00452987	0.0045694	0.00461852
3	0.00392213	0.00453626	0.00459553	0.00466921
4	0.00391938	0.004542	0.00462096	0.00471918
5	0.00391603	0.00454709	0.00464563	0.00476829
6	0.00391213	0.00455132	0.00466953	0.00481674
7	0.00390743	0.00455495	0.00469282	0.00486433
8	0.00390202	0.0045579	0.0047151	0.0049113
9	0.00389657	0.00456005	0.00473719	0.0049573
10	0.00388992	0.00456165	0.00475817	0.00500255
12	0.00387533	0.0045628	0.00479756	0.00509041
14	0.00385842	0.00456104	0.00483413	0.00517502
16	0.00383789	0.00455647	0.0048683	0.00525629
18	0.00381489	0.00454922	0.00489955	0.00533452
20	0.00379053	0.00453913	0.00492749	0.00540908
25	0.00371795	0.00450186	0.00498299	0.00557834
30	0.0036332	0.0044475	0.00501891	0.00572319

Table 6: Reference areas for each body for each angle of attack.

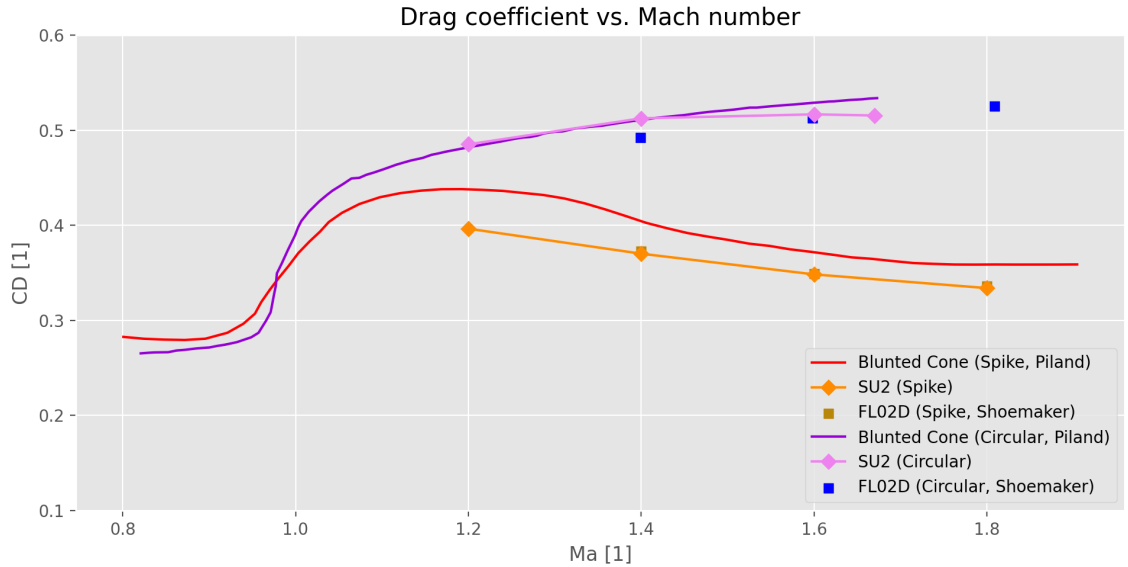


Figure 28: Drag coefficient computed by SU2 against Piland’s [24] and Shoemaker’s [20] for both the blunt and spiked bodies.

4 Results

4.1 Code Validation Results

The drag coefficient results obtained for these validation cases are plotted in figure 28. The drag coefficient (CD) was calculated for Mach numbers of value 1.2, 1.4, 1.6, and 1.8 for the spiked body, and Mach Numbers 1.2, 1.4, 1.6, and 1.67 for the blunt body. As can be seen from the plot at first sight, the SU2 computed results agree quite well for both the blunt and spiked body cases. For the spiked case it can be seen that the results for Mach 1.4, 1.6, and 1.8 are almost the same as Shoemaker’s [20], and for the blunt body the results are even closer to Piland’s experimental ones ([24]) than theirs, furthermore the behavior of the curves is quite similar which is also important for the validity of the study. It should also be noted that the blunt body with the circular nose has a higher drag coefficient than the spiked body in the supersonic flow regime, which agrees with the literature, as previously mentioned, whereas for lower values it eventually gets lower. This also demonstrates the usefulness of the spike in lowering the drag coefficient for supersonic vehicles, moreover, this effect becomes greater the bigger the Mach number gets, as can be seen at the right side of the plot. This agrees well with the literature, which is why in most articles the spikes are studied in the hypersonic flow regime.

The results were also visualized using the open-source, scientific visualization software named Paraview [26]. The computed flows can be seen in figures 29 and 30, both show all the characteristic zones for these type of flows mentioned by [15] that can be seen in figure 1. Figure 30 simply displays the strong shock bow that forms in front

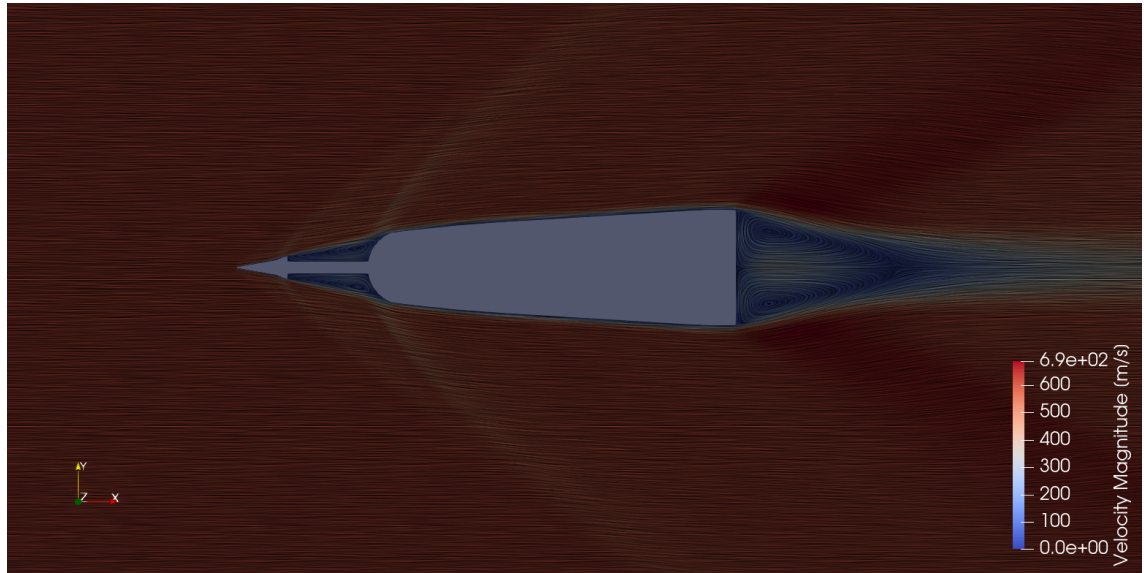


Figure 29: Spiked windshield's flow visualization at freestream Mach of 1.8, coloured by Velocity.

of a circular blunt body, and in figure [29](#) the effects of the spike are clearly visible, meaning, the decomposition of this shock wave into a system of multiple shock waves. First of all the two main shockwaves, the oblique foreshock and the reattachment zone, can be seen near the end of the spike and at the shoulder of the body respectively, there's also another foreshock at the tip of the spike which eventually merges with the other one. Then the recirculation zone is found right after the end of the spike with the appropriate vorticity structure mentioned by Ahmed in [\[15\]](#): a primary vortex found just below the shear layer, a second one below it, and a tiny tertiary one created at the root of the spike, this structure is also shown in figure [31](#), the smallest vortex was probably not captured by the simulation due to the refinement of the mesh. Lastly the reattachment zone is found at the body's shoulder as expected.

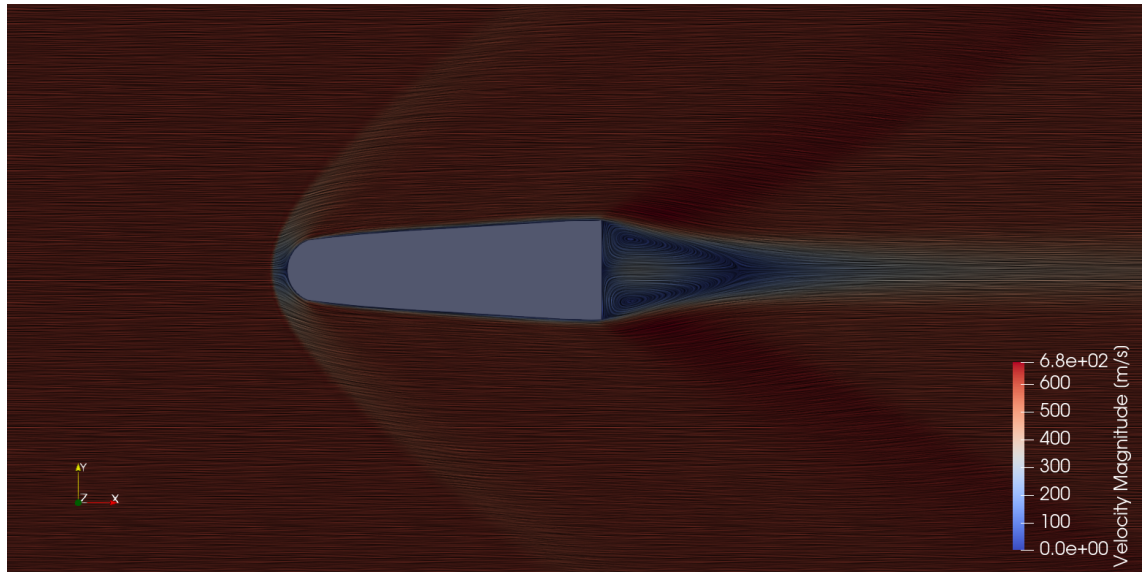


Figure 30: Blunt Body's Flow Visualization at freestream Mach of 1.8, coloured by Velocity.

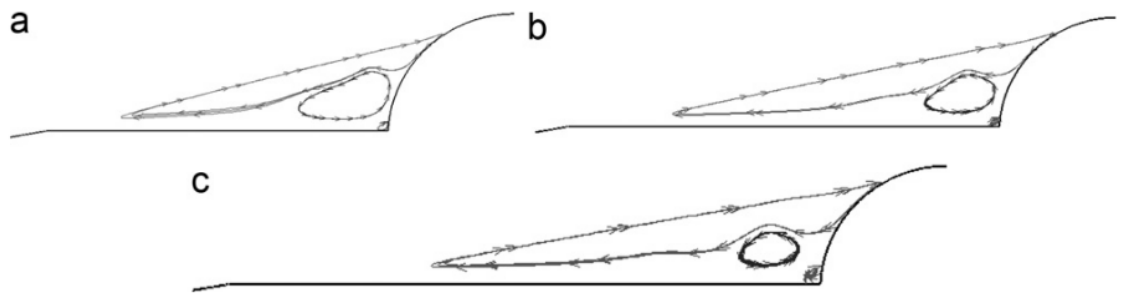


Figure 31: Ahmed's vorticity structured mentioned in [15]: "Vorticity structure inside the recirculation zone for three models with sharp spike: (a) $L/D=1.5$; (b) $L/D=2$ and (c) $L/D=2.5$."

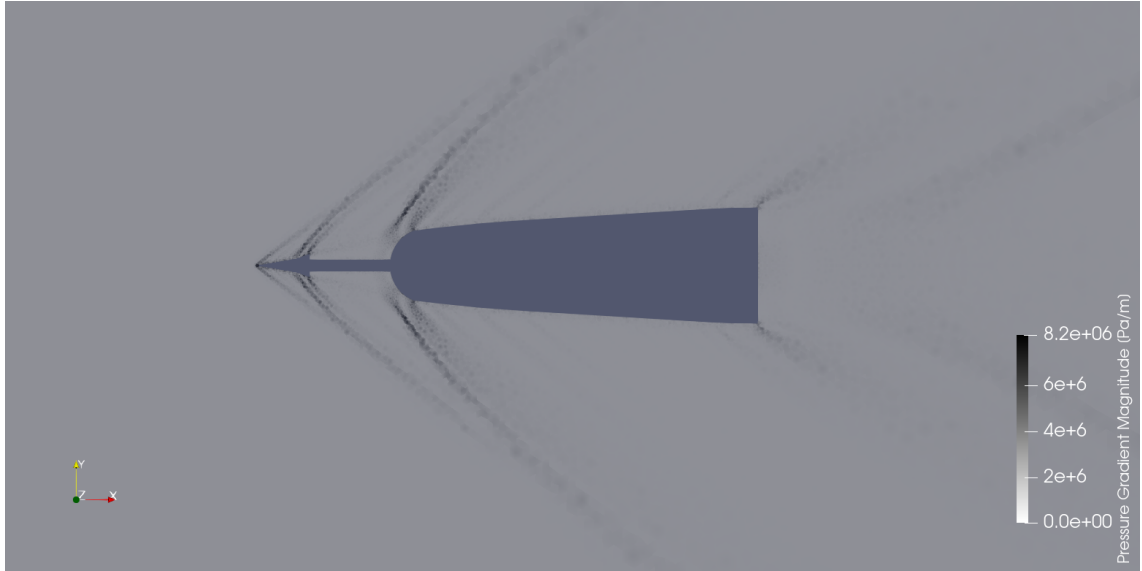


Figure 32: Spiked windshield's computed shadowgraph at Mach=1.8

To further visualize and validate the simulations, a synthetic shadowgraph for the spiked body was created on Paraview to compare it with Ahmed's [15] own shadowgraph, for the reason that with the aid of this visualization method shockwaves are more easily seen. To more easily compare the shape of these shockwaves, the coordinates of multiple points placed along the surfaces of these images were extracted and then plotted, the shadowgraphs can be seen in figures 32 and 33, and the plot of their geometries in 34. A shadowgraph of the circular blunt body was also obtained and can be seen in image 35 but there's no corresponding experimental shadowgraph in 24 to compare.

Figure 34's curves are not completely accurate to the shadowgraph's curves due to how they were obtained, but they are accurate enough for comparison purposes. It can be easily noticed that the angles agree very well at the beginning of the curves and begin to slightly differ at the end, this is because, as it was previously mentioned, the mesh was refined only close to the body surface and not on the location of the shockwaves, so their location and effects couldn't be completely captured, this could be solved with adaptive meshing, meaning refining the mesh on the shockwaves' locations, but that is out of the scope of this validation. The angle error is of 17.94% for the foreshock and 12.69% for the reattachment shockwave, if only the lengths corresponding to the first 5 points of the curves' are taken into account to lessen the mesh refinement's effects then the errors are of 14.29% for the foreshock and 9.54% for the reattachment shock, which is much better but will never be exact due to the mentioned issue.

Overall, the results obtained with the SU2 code agree quite well with the literature both in values, behavior and flow structure which justifies its usage for the studies performed in this thesis.

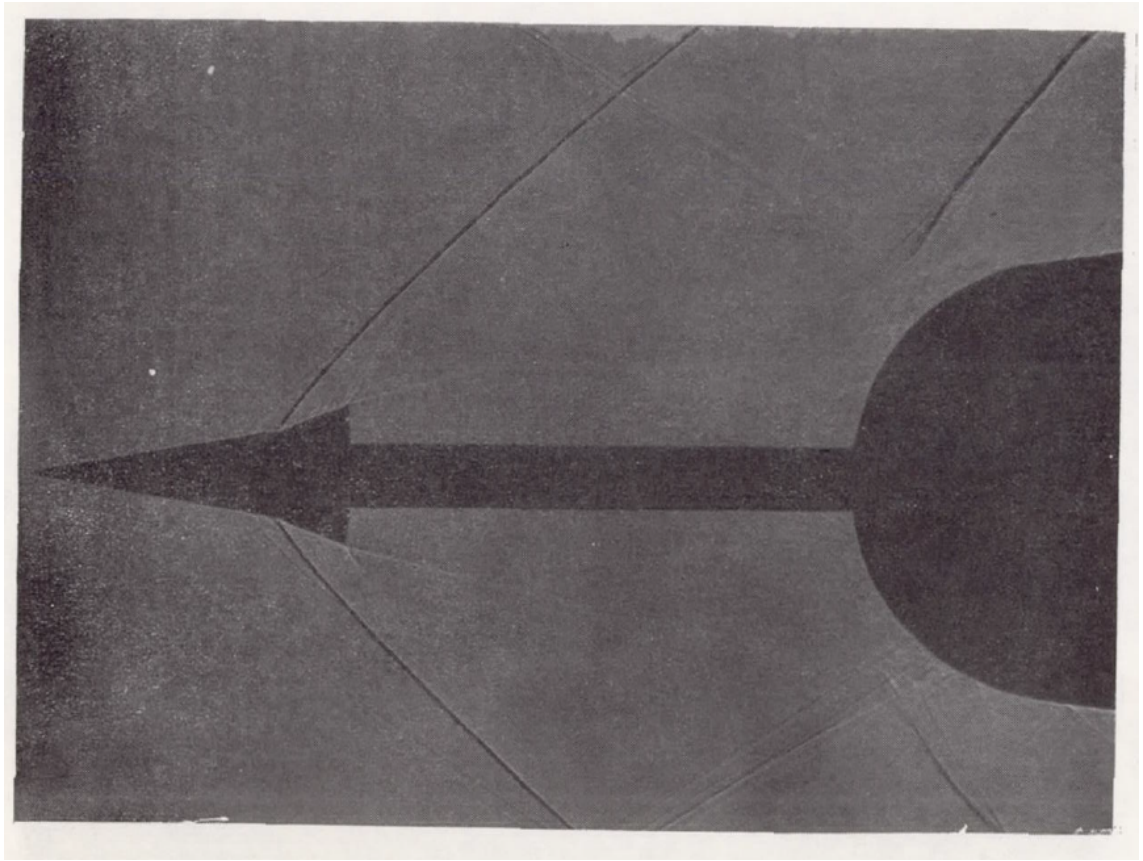


Figure 33: Piland's [24] Spiked Windshield's Shadowgraph at Mach=1.8

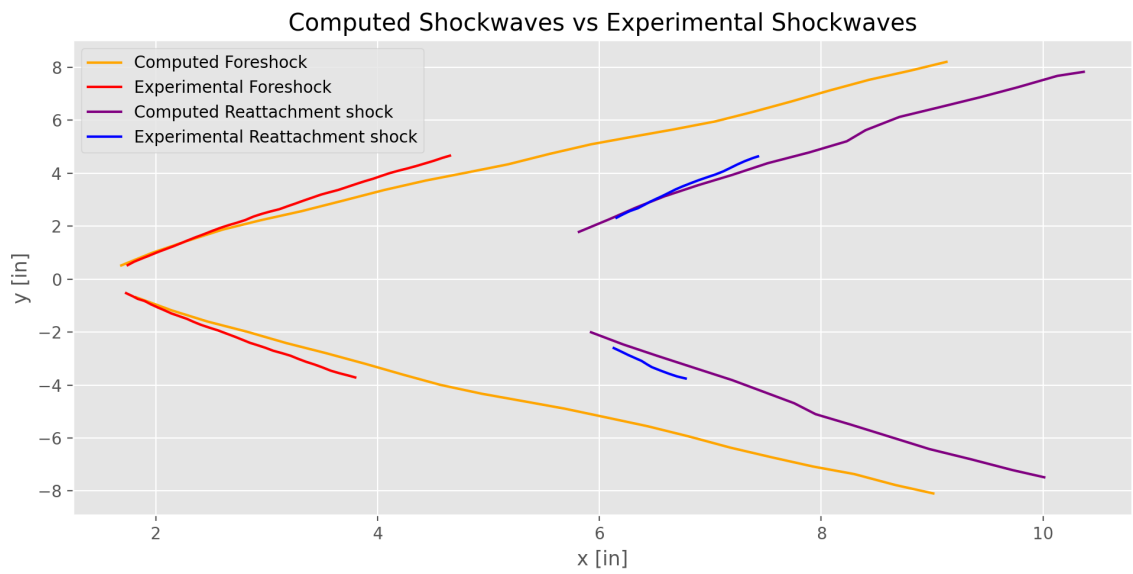


Figure 34: Computed and Experimental Foreshock and reattachment shock geometry

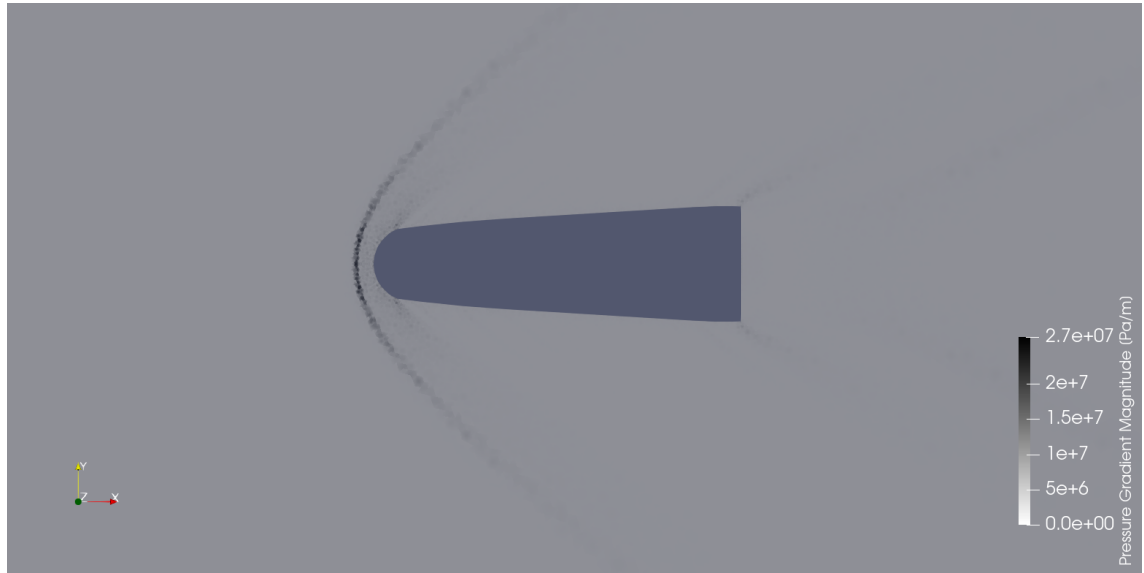


Figure 35: Blunt Body's Computed Shadowgraph at Mach=1.8

4.2 Grid Independence Test Results

The drag coefficient (DC) results of this test can be seen in figure 36 and in table 7 in the third column, along with the value difference between the mesh drag coefficient and the previous bigger mesh drag coefficient in the fourth column, and the percentage of change of the mesh drag coefficients with respect to the previous bigger mesh drag coefficient in the fifth column.

Mesh	t _{mr} [m]	DC [1]	DC difference	DC change percentage
Coarse 1	0.009	0.4898	Does not Apply	Does not Apply
Coarse 2	0.007	0.395	-0.095	-19.356%
Medium 1	0.004	0.3347	-0.06	-15.277%
Medium 2	0.003	0.3155	-0.019	-5.74%
Refined 1	0.00096	0.3069	-0.009	-2.711%
Refined 2	0.00086	0.3030	-0.004	-1.266%

Table 7: Mesh independence test results.

As can be seen from figure 36 the drag coefficients values start to converge in the last three points of the plot, as it can be seen from the drag coefficient change percentage column in table 7 that they have small change percentages as opposed to the previous points. Based on these results, the Refined 1 mesh with the t_{mr} size of 0.00096 [m]

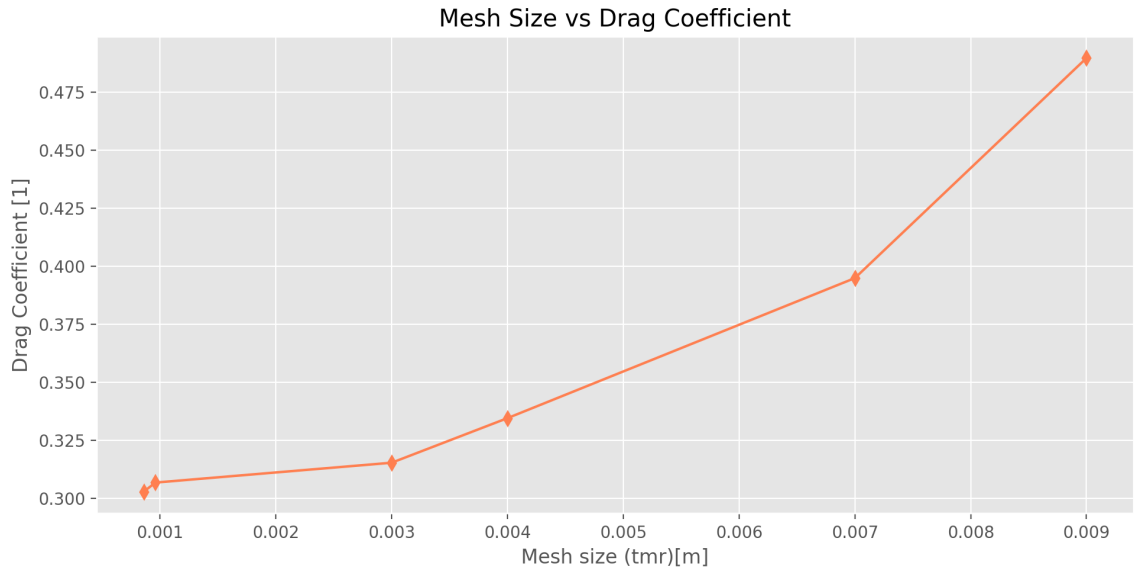


Figure 36: Mesh Independence Test Drag Coefficient Results

was decided upon as the basis for the main study meshes, as the next smaller mesh size presents little change in the drag coefficient result but a drastically higher computation time is needed.

4.3 Ringed Body Confirmation Test Results

The drag coefficient results of this test are presented in figure 37. As can be seen the aerospike severely reduces the blunt body drag coefficient for all the Mach number cases, just as the the ring in turn further reduces it in comparison to the spiked body, thus working as intended. The drag coefficient values and the spike and ring percentage reductions with respect to the blunt body for each mach number are presented in table 8.

Before talking about the flow visualization figures, it is worth noting that from here on all flow visualization images, tables, and all data in general is given in the International System Units. Also the flow visualizations presented next correspond to a Mach number of 2.

Figures 38, 39, and 40 show the pressure gradient on the top half of the image, and the stream lines colored by the Mach number on the bottom half. The blunt body flow visualization provides a simple basis, but the main focus of the analysis are the spiked and ringed bodies. The pressure gradient was calculated to better visualize the shock waves formed, figure 39 shows the correct behavior for a spiked body, the spike breaks the strong bow shockwave into a system of smaller shockwaves as it was previously seen in the validation test, but more interestingly, figure 40 shows the ring on the body surface doing the same, breaking the reattachment shockwave formed by the shear layer into a system of smaller shockwaves, while also further increasing the size of

Ma = 1.6		
Body	DC [1]	DC Reduction [1]
Blunt Body	1.0094	Does not apply
Spiked Body	0.5307	47.42%
Ringed Body	0.5006	50.4%
Ma = 1.8		
Body	DC [1]	DC Reduction [1]
Blunt Body	1.0085	Does not apply
Spiked Body	0.5041	50.02%
Ringed Body	0.4721	53.19%
Ma = 2.0		
Body	DC [1]	DC Reduction [1]
Blunt Body	1.0141	Does not apply
Spiked Body	0.5668	44.11%
Ringed Body	0.4721	47.55%

Table 8: Drag Coefficient results and reductions for all the bodies at different Mach numbers.

the expansion zone, explaining why the drag coefficient was reduced. This shockwave behavior and Mach visualization agrees quite well with the shock wave visualization obtained by Elsamanoudy et al. in [2], which was previously shown in figure 6, and their mach visualization which is now shown in figure 41.

Furthermore, figures 42, 43, and 44 show the surface fluid heat flux contour on the top half of the image, and the temperature contour on the bottom half. It's worth noting that it's the surface fluid heat flux being visualized, meaning that positive values are heat gained by the fluid on the surface of the body, while negative values are heat lost by the surface fluid and gained by the body. Again, the blunt body visualization is shown as a reference, it can be seen that most of the heat transfer is located at the body's shoulder. Now, regarding the spiked body, figure 43 shows that the heat flux is now located mainly at the shoulder of the aeroshield, which agrees well with the literature [15], and also the blunt body's shoulder. In addition, something similar can be viewed in figure 44, most of the heat flux is located on the aeroshield's and the body's shoulder, but also on the exterior surface of the ring. Also, the temperature

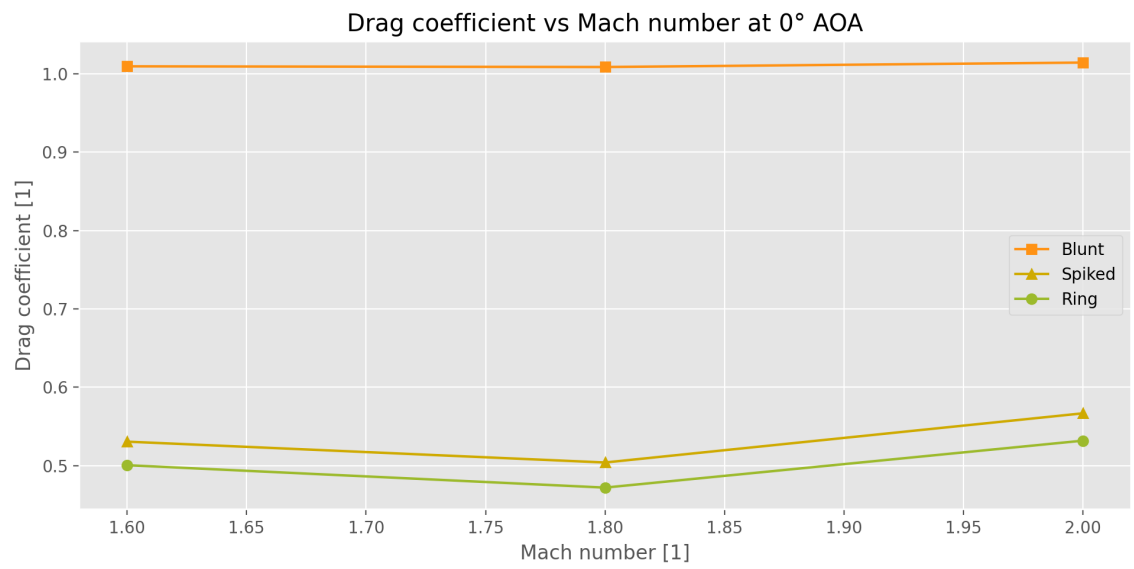


Figure 37: Confirmation test for the ringed body.

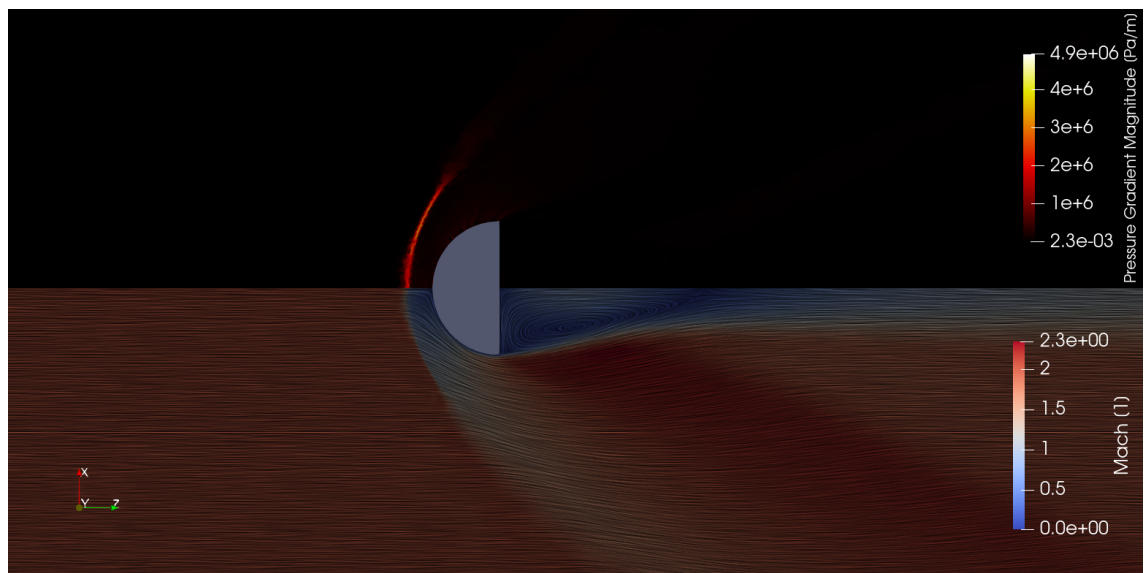


Figure 38: Pressure Gradient and Mach number of the Blunt Body at Mach 2 with null AoA.

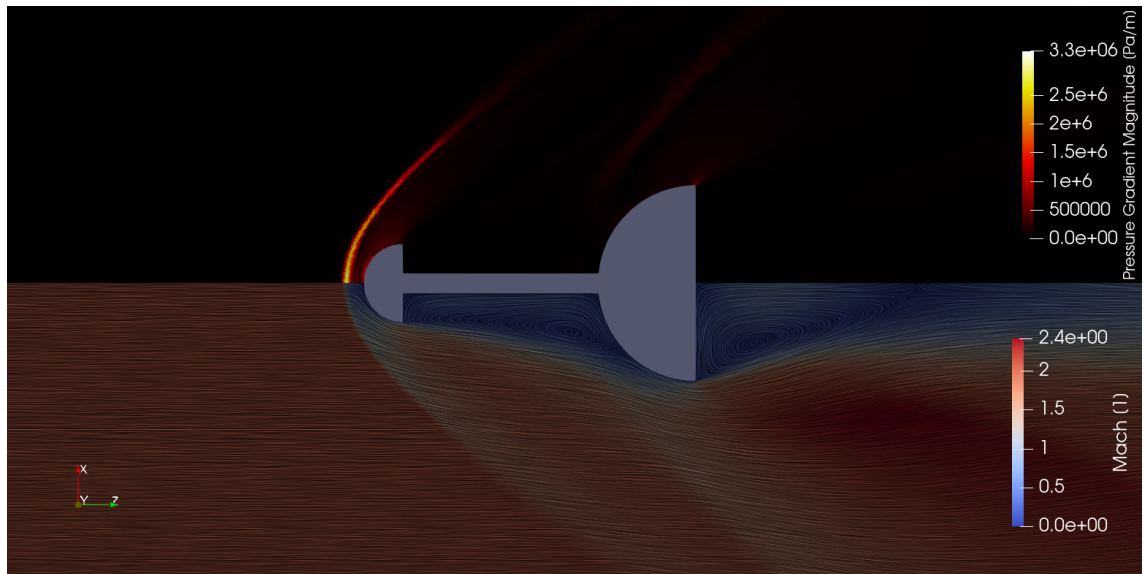


Figure 39: Pressure Gradient and Mach number of the Spiked Body at Mach 2 with null AoA.

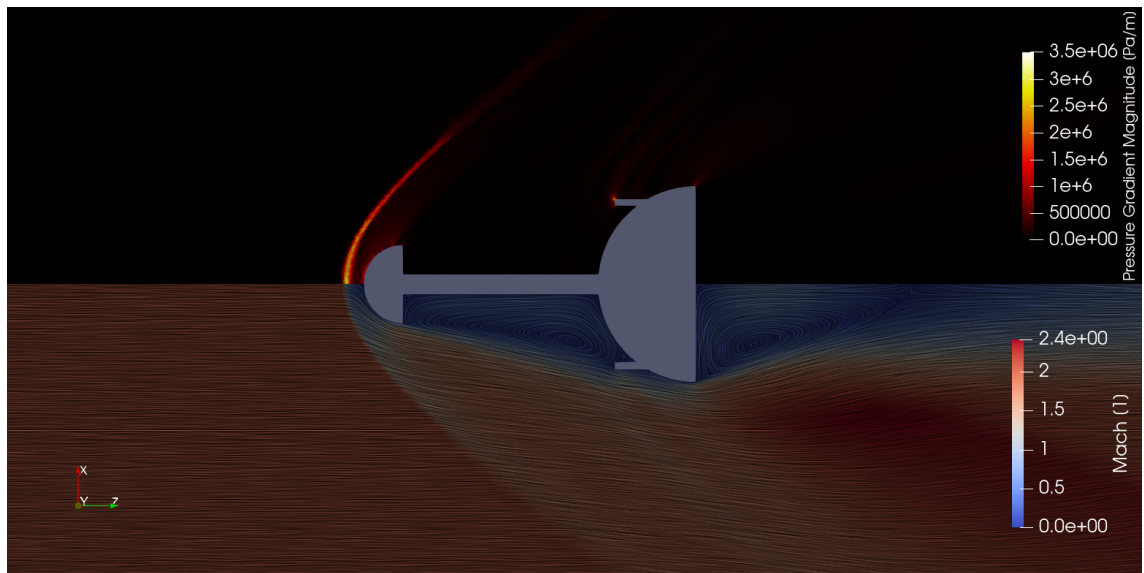


Figure 40: Pressure Gradient and Mach number of the Ringed Body at Mach 2 with null AoA.

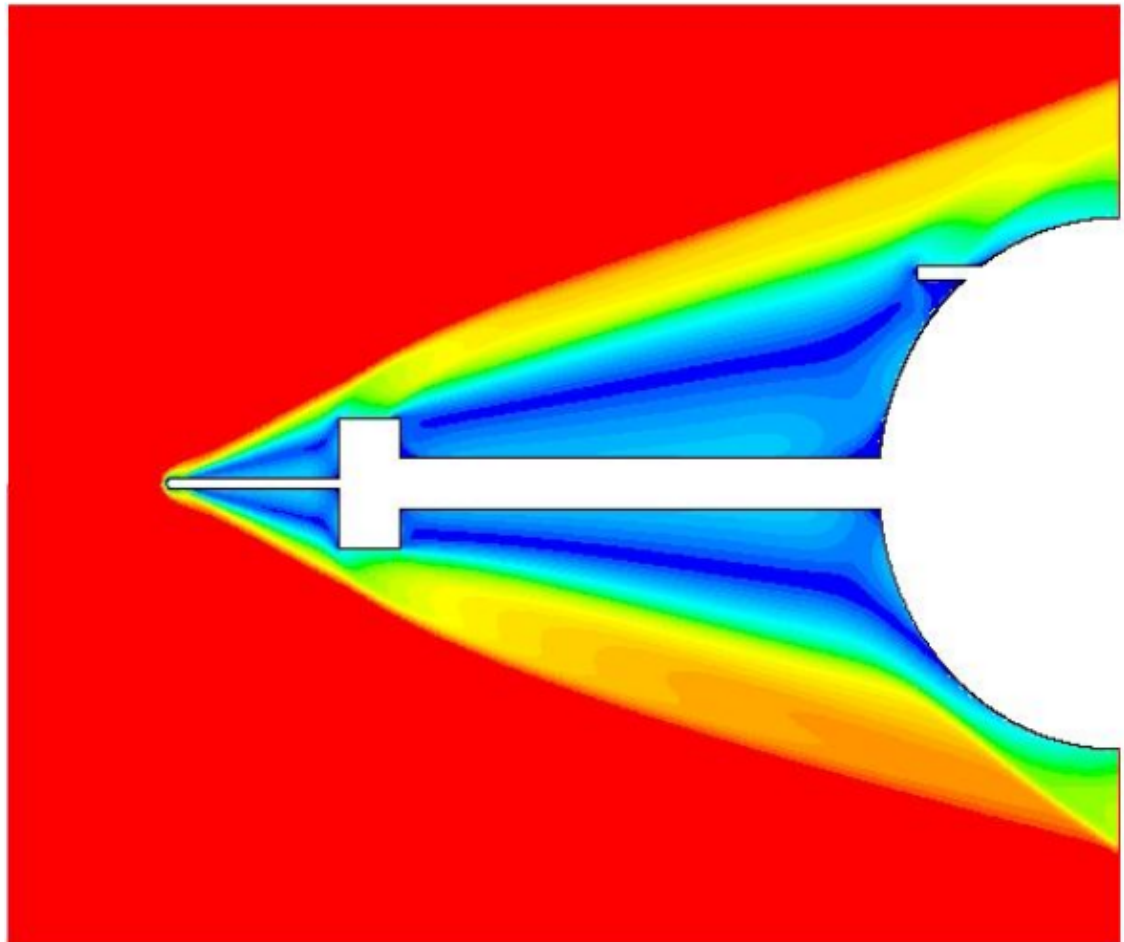


Figure 41: "Mach contour with reattachment ring (upper) and without (lower)." by Elsamanoudy et al. [2]

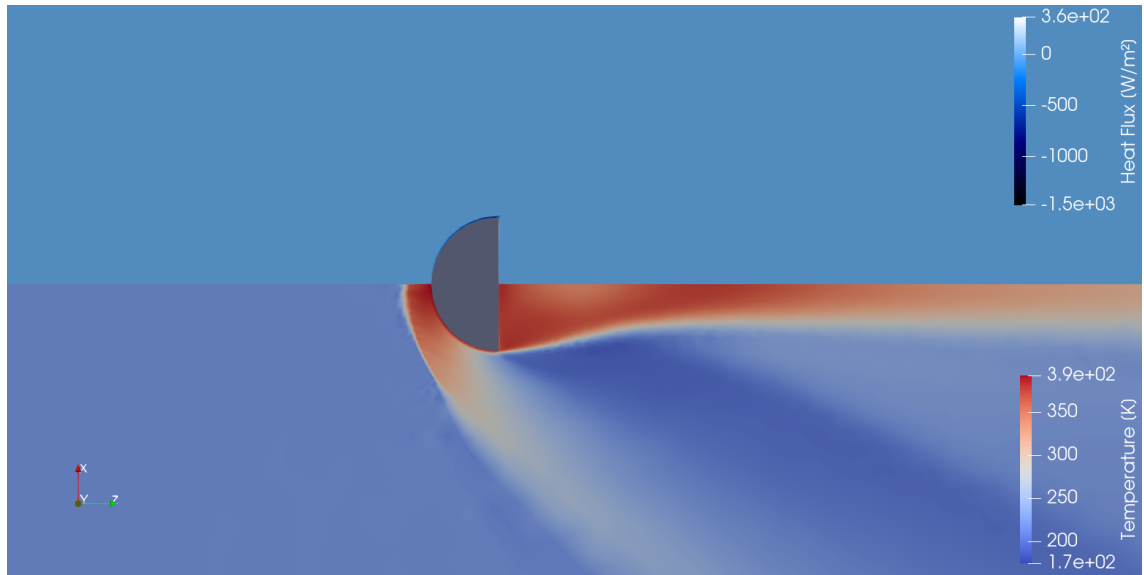


Figure 42: Surface fluid heat flux and temperature of the blunt Body at Mach 2 with null AoA.

contour agrees quite well with the one obtained by Elsamanoudy et al. in [2], which can be seen in figure 45.

These flow visualizations are mainly useful to locate where most of the surface heat transport takes place, and get a general idea of the temperature profiles that are formed, however, in order to make a more precise assessment of the thermodynamic reductions the ring provides when compared to the other two bodies, two different plots were obtained, angular position vs surface fluid temperature (it is worth emphasizing the fact that it's the temperature on the surface of the body and not the wall temperature itself, as that one is constant), and angular position vs wall heat flux (in this case the wall heat flux is visualized, so positive values are heat gained by the body, while negative values are heat lost by it). Where the angular position is the position on the main body surface, ranging from where the spike ends and the body starts, to the body shoulder, defined by the angle made between the body surface point and the point located on the body symmetry line at the right-side end of the body. These plots are similar to the ones obtained by Elsamanoudy et al. [2] in order to better analyze the performance of the reattachment ring. The plots were obtained for all three bodies for each of the Mach numbers they were tested in and can be seen in figures 47 - 52. Figure 46 shows an example of the points whose data was captured, it's worth noting in this figure how in the case of the ringed body, at around the 45° angle the fore-body's surface points are no longer captured, and instead the ring's exterior surface points data is captured.

In general, the plots have the same behavior despite the Mach number, in the temperature plots it can be seen that the spike body has a lower temperature for all the angle range, and in turn the ringed body has a lower temperature for most of the angle range, the zone that presents hotter temperatures more clearly is around the 45°

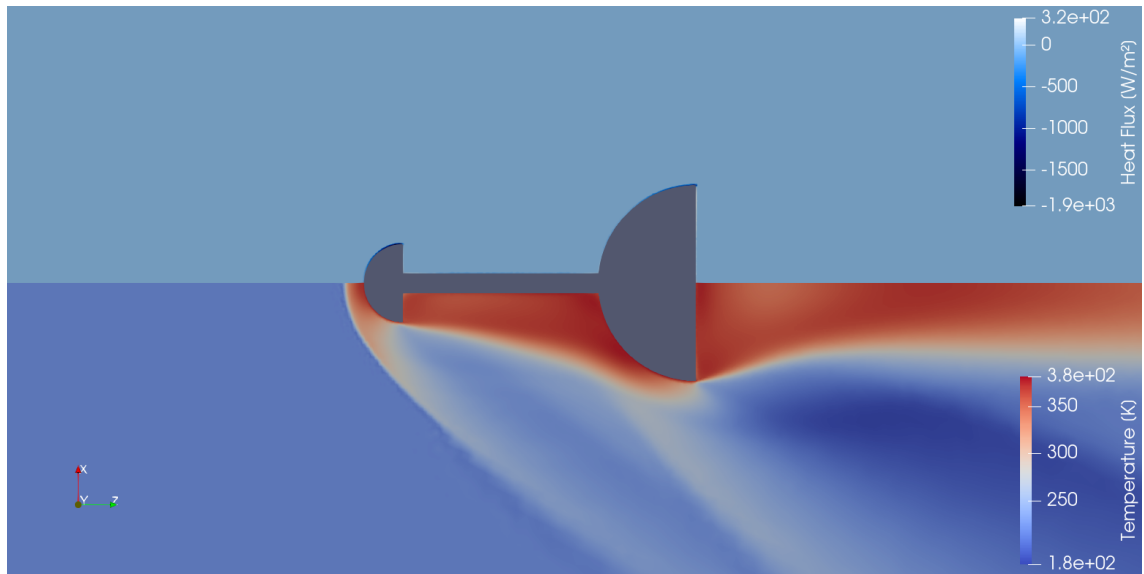


Figure 43: Surface fluid heat flux and temperature of the spiked Body at Mach 2 with null AoA.

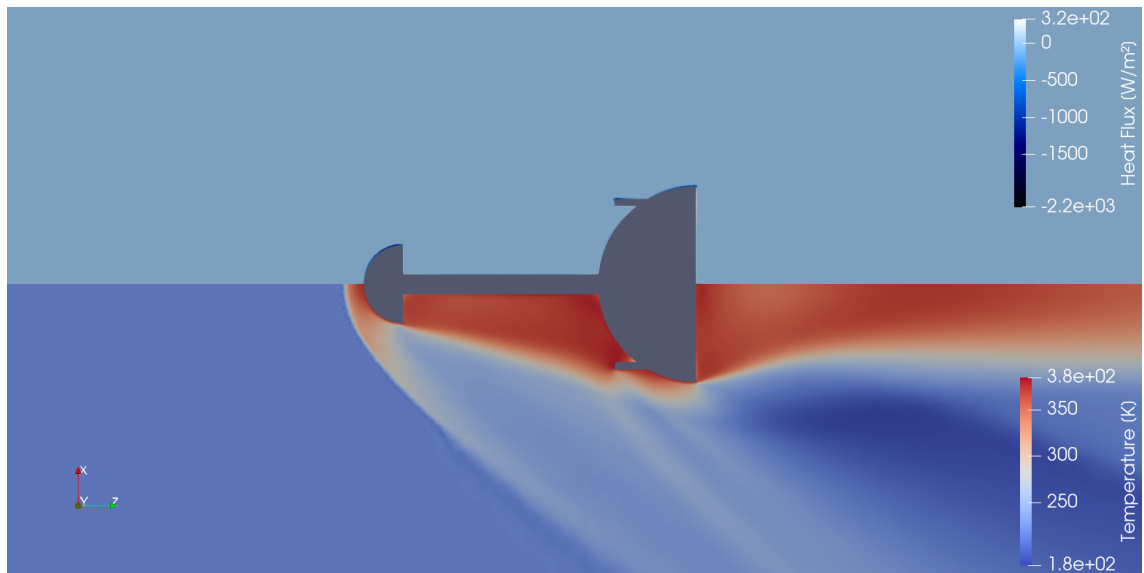


Figure 44: Surface fluid heat flux and temperature of the ringed Body at Mach 2 with null AoA.

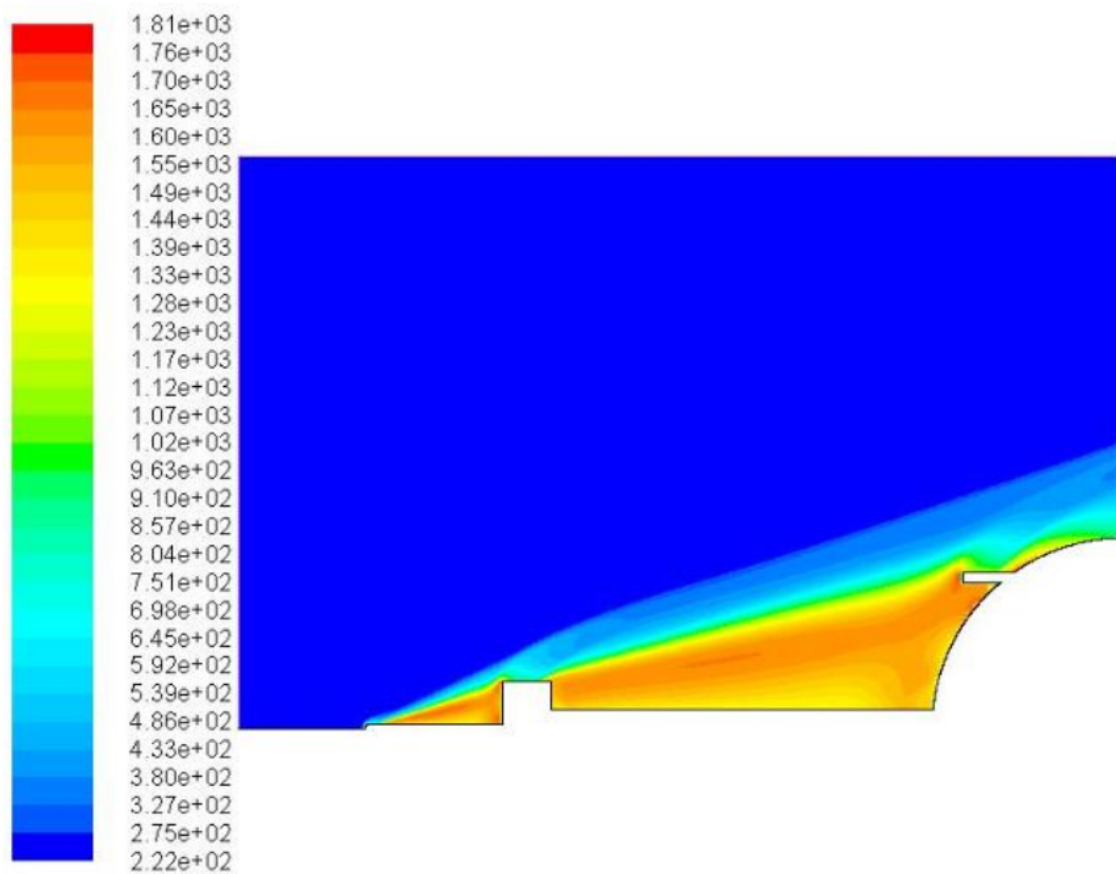


Figure 45: Temperature contours around ring fitted configuration with $h = 0.1D$ at Mach 6 (values given in Kelvins)” by Elsamanoudy et al. [2].



Figure 46: Points captured for the thermodynamic plots in the case of the ringed body.

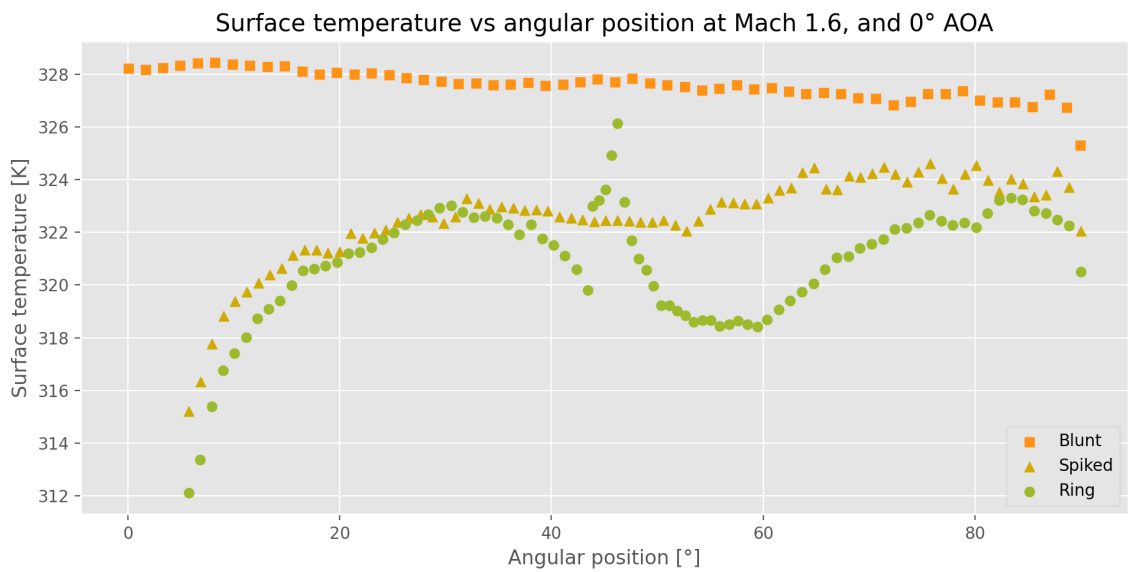


Figure 47: Fluid temperature on the body surface for the three bodies at Mach 1.6

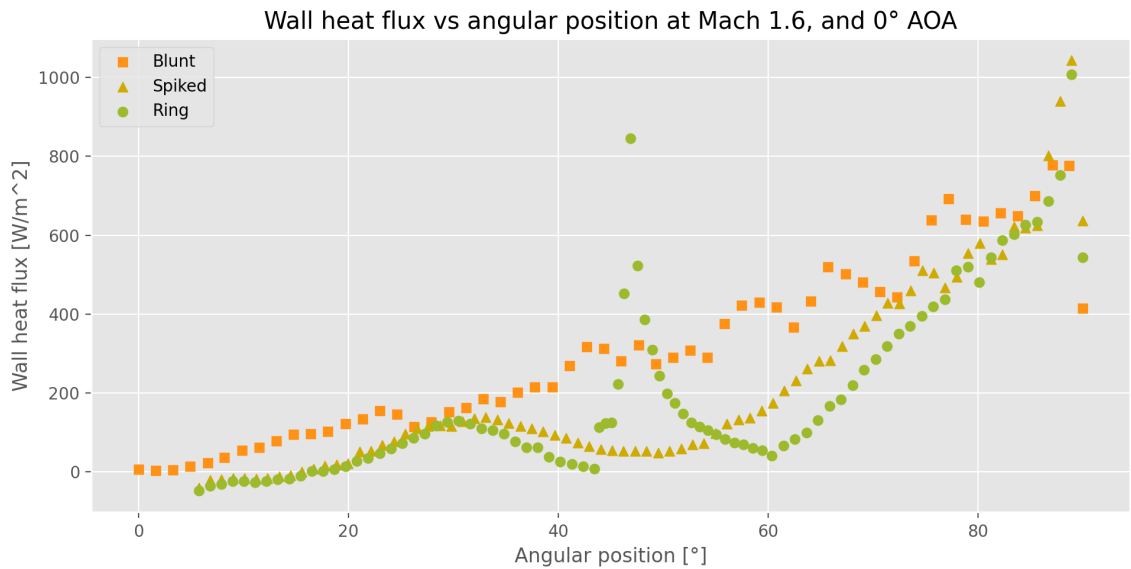


Figure 48: Wall heat flux for the three bodies at Mach 1.6

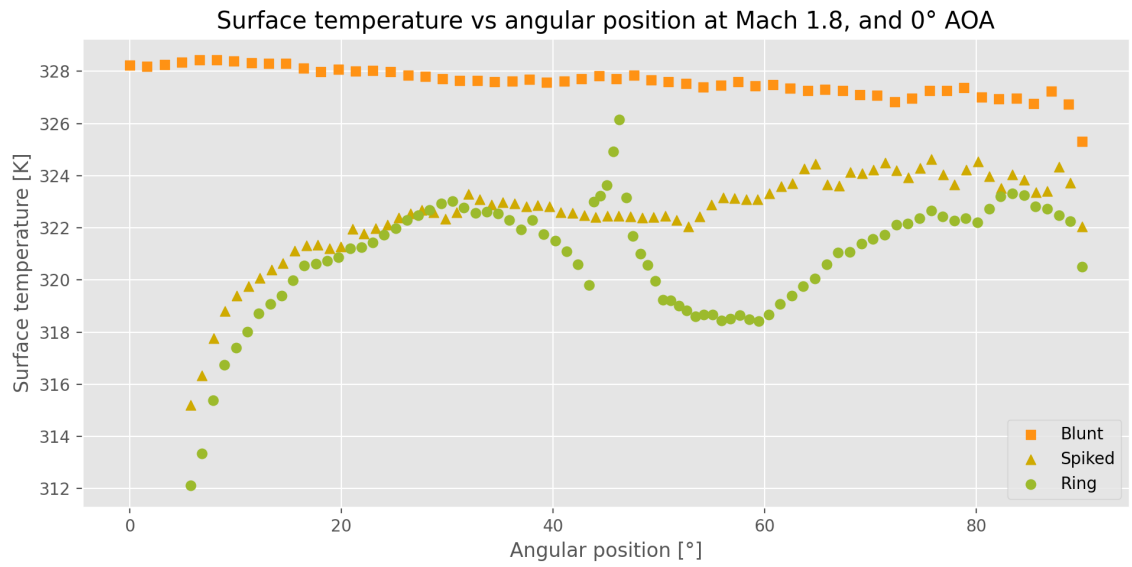


Figure 49: Fluid temperature on the body surface for the three bodies at Mach 1.8

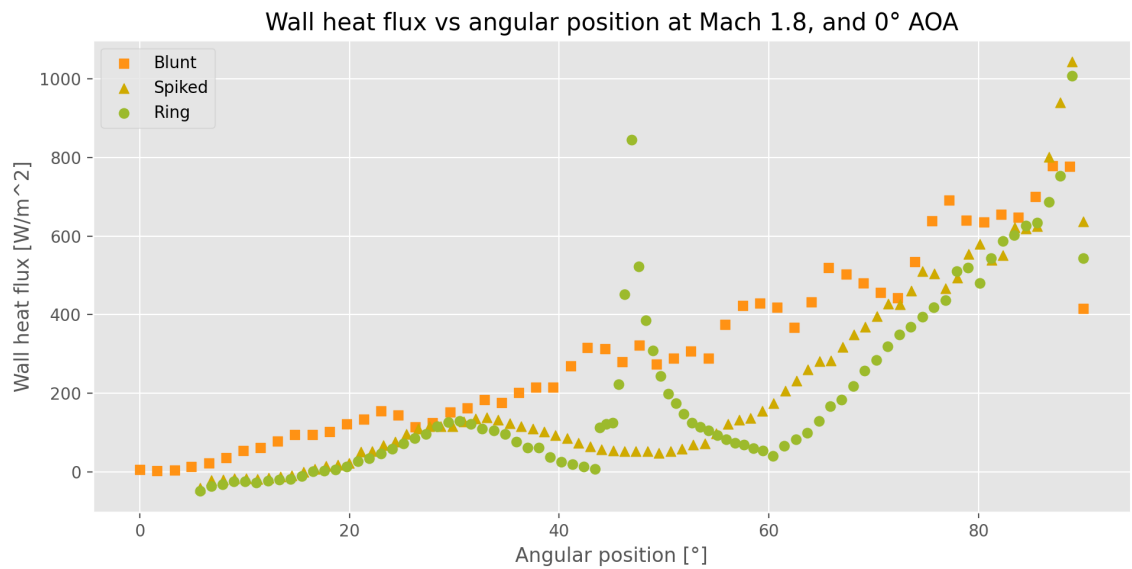


Figure 50: Wall heat flux for the three bodies at Mach 1.8

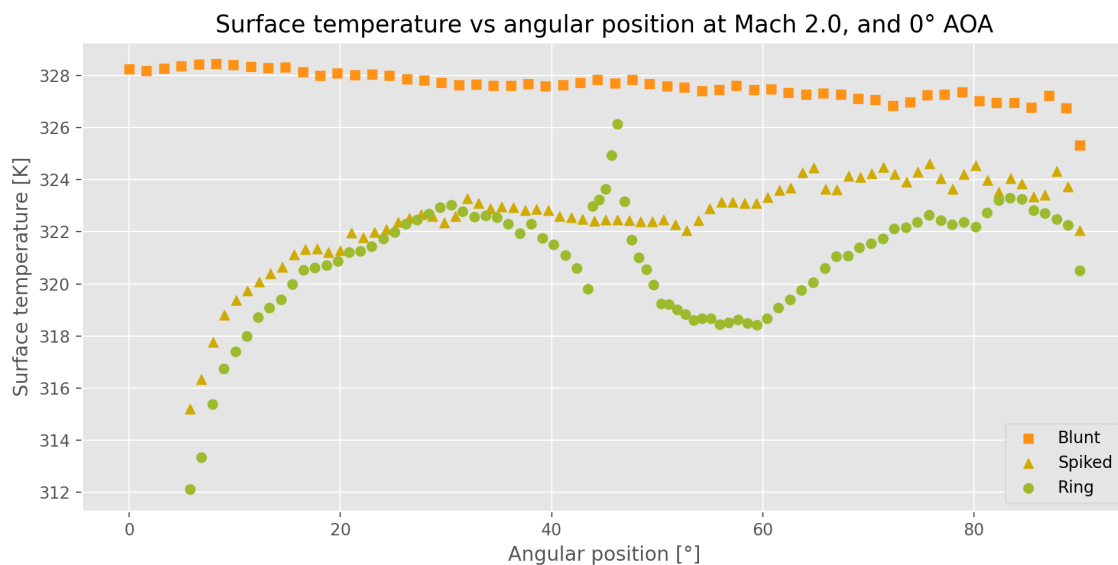


Figure 51: Fluid temperature on the body surface for the three bodies at Mach 2.0

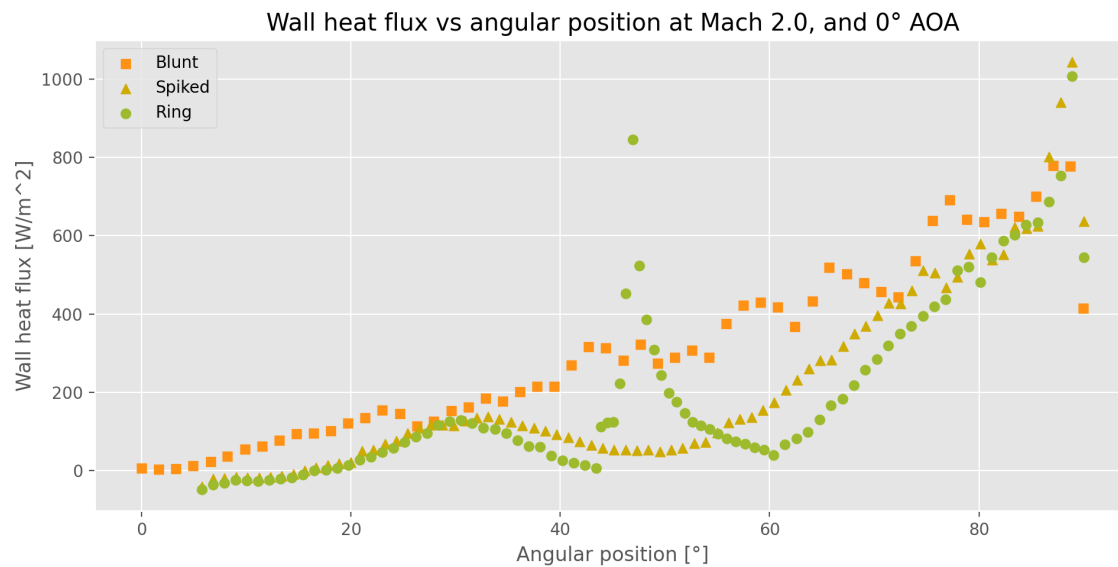


Figure 52: Wall heat flux for the three bodies at Mach 2.0

angle, this zone is exactly the outer surface of the ring. This increase in temperature makes sense as the ring is breaking the shear layer into a smaller system of shock waves, however, the fact that the temperature goes lower than that of the spiked body as the position approaches the body shoulder, means the ring is serving its purpose. Practically the same behavior can be seen in the heat flux plots, the spiked and ringed bodies have a mostly lower heat flux, and in turn the ringed body has a lower heat flux than that of the spiked body, except for the ring zone, where it increases dramatically. This behavior confirms that the ring is serving its purpose and thus, it is well designed.

4.4 Reattachment Ring at Multiple Angles of Attack Results

In this section, the results of the main study will be discussed, it is worth noting that because there are results for each body for multiple angles of attack, only the results of the 0° , 16° and 30° angles will be discussed, mainly in the case of the flow visualization and the thermodynamic analysis, as otherwise too much data would be presented with little to no purpose. It is worth remembering that as both ringed bodies will be discussed in this chapter, the body with the shorter ring is referred to as Ring 1, while the body with the longer ring is referred to as Ring 2.

4.4.1 Drag Coefficient Results

The drag coefficient results for each body are plotted against the angle of attack in figure 53 and are also presented in table 9. It can be seen that the three spiked bodies present a lower drag coefficient than the blunt body for most of the angle of attack range, both ringed bodies lower than the spiked body, and Ring 2 a little lower. The drag coefficient difference between the three spiked bodies seem to increase at first and it slowly disappears as the angle increases. The literature indicates that spikes are only useful for small angles of attack [15], as reported by Menezes et al. [19] and Huebener et al. [28], among others, tested the feasibility of spikes on blunt bodies at hypersonic speeds at multiple angles of attack, and in general noticed that the spikes lost their benefits at around a 10° angle of inclination, mainly due to the impingement of the separation shock wave on the body surface. In figure 53 it can be observed that the spiked bodies are still very much useful, in drag coefficient reduction terms at least, at even 20° degrees, this is most probably due to the fact that these results are for a Mach number of only 2, thus the separation shockwave and its effects are much weaker. This leads to the conclusion that even if the drag reduction effects of spikes and reattachment ring in the supersonic regime are much lower than those at the hypersonic regime, they can still be very useful for the cases where the blunt body needs more maneuverability. On the other hand, it seems that the ring length increase of Ring 2 lowered its drag coefficient (as it also usually happens when increasing the length of a spike), for most of the angle range, in comparison to Ring 1 despite the bigger reference area, however, later on, after 20° , Ring 2 actually surpasses the drag coefficient of both Ring body 1 and the Spiked body, and after 30° Ring 1 passes the Spiked body and Ring 2 surpasses

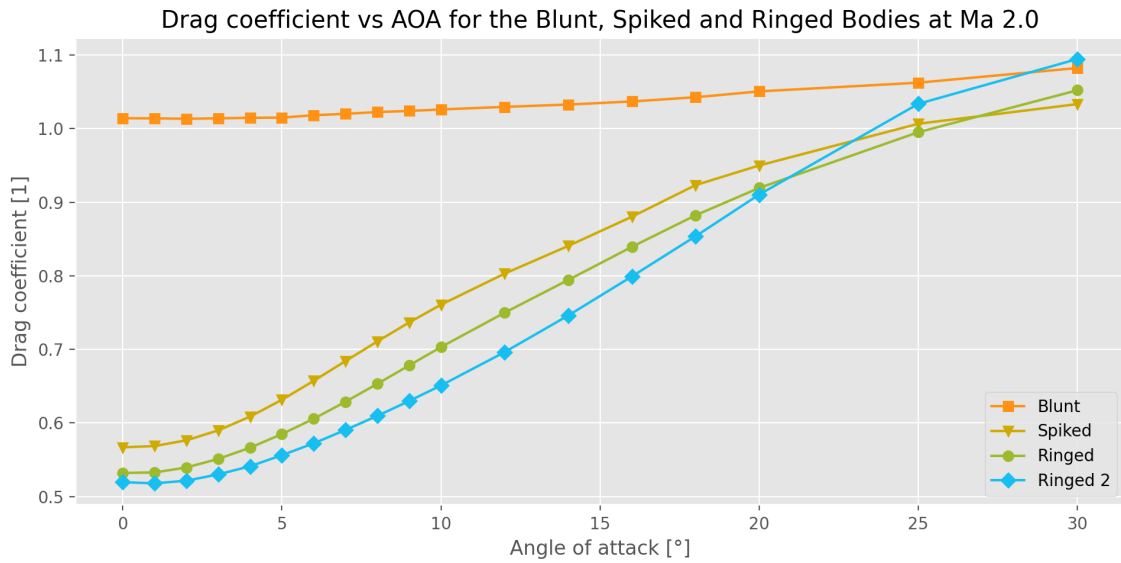


Figure 53: Drag coefficient vs Angle of Attacks for each body.

even the blunt body, becoming inefficient in terms of drag reduction. From this it can be deduced that the ring at angles of attack mostly behaves like it would a a null angle of attack, where the length of the ring can be adjusted to either benefit more the drag reduction or heat reduction effects, however even if increasing the length of the ring further reduces the drag coefficient, it only does so for a smaller range of angles, because as the angle increases, the drag effects caused by the increase of the reference area eventually overcome the drag reduction effects of the ring, increasing the Mach number most probably further reduces this efficient range as it would further increase the drag effects caused by the increase of the area of projection. This means that depending on the maneuverability needed and the Mach number, the ring's length can be adjusted to still reduce drag and heat, thus proving that in an ample variety of cases it is a good combinational method for aerospike on blunt bodies.

4.4.2 Results at 0°

Before discussing the results, it is worth noting that the results for the 0° angles of attack for the Blunt, Spiked, and Ring 1 bodies, are the same as those in the Mesh Design and Ringed Body Confirmation Test for Mach 2, as a result only the visualization for the Ring 2 body will be shown here, and in the case of the other bodies, if they are discussed they will be simply referenced. This will not be the case for the heat and temperature plots as the previous ones did not include the results for the Ring 2 body.

Starting from Ring 2's figure 54, comparing it to Ring 1's 44, it can be seen that the heat flux is located in the same places and the range of values stayed the same, and the temperature profile is pretty similar. Furthermore comparing figures 55 and 40, it can be seen that Ring 2's shockwaves have been displaced upstream due to the ring's

	Drag Coefficient [1]			
Angle of attack [°]	Blunt Body	Spiked body	Ringed body 1	Ringed body 2
0	1.0141	0.5668	0.532	0.5194
1	1.014	0.5686	0.5327	0.5179
2	1.0134	0.5763	0.5394	0.5214
3	1.014	0.5898	0.5511	0.53
4	1.0147	0.6086	0.5663	0.541
5	1.0151	0.6314	0.5848	0.5562
6	1.0182	0.6572	0.6056	0.5722
7	1.0201	0.6841	0.6288	0.5905
8	1.0225	0.7108	0.6531	0.6096
9	1.0241	0.7366	0.6781	0.6298
10	1.0261	0.7607	0.7031	0.6509
12	1.0296	0.8029	0.7498	0.6963
14	1.0327	0.8406	0.7943	0.746
16	1.037	0.8803	0.8393	0.7991
18	1.0427	0.9232	0.8822	0.8537
20	1.0506	0.95	0.9194	0.9104
25	1.0625	1.0066	0.9951	1.0337
30	1.0824	1.0334	1.0522	1.0946

Table 9: Drag Coefficient for each angle for the different bodies.

length increment, and more noticeably, on the Mach side of the image, the expansion zone has expanded, which explains the drag coefficient reduction. Now, regarding the more important figures, meaning figures [56](#) and [57](#), Ring 2 has lower values than all other bodies for both the surface temperature and the wall heat flux for most of the surface angle range, presenting peaks only on the surface of the ring, the same way Ring 1 does, thus making Ring 2 perform better than the other bodies at a 0° angle of attack, not only in terms of the drag coefficient, but also in thermodynamic terms. However it must be noted that this heat and temperature reduction is not that big close

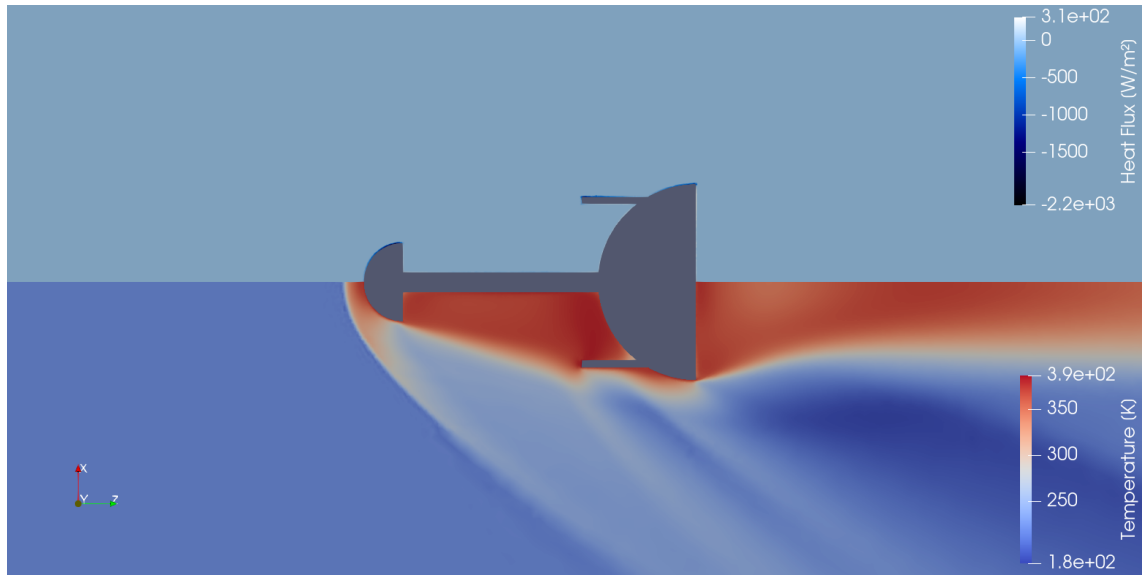


Figure 54: Surface fluid heat flux and temperature of ring 2 at Mach 2 with null AoA.

to the body shoulder when comparing it to Ring 1.

4.4.3 Results at 16°

Before discussing these results it is worth noting that the types of flow visualizations have been separated due to the flow no longer being symmetric.

Figures 58-65 show the Mach number and temperature profiles of the different bodies, they're analyzed together as they mostly show the same effects caused by the angle of attack. The blunt body's profiles have not changed much, they simply shifted accordingly to the angle of attack. However, the spiked body's profiles are pretty different from their null angle of attack counterpart, most notably on the upper side of the body, the angle of the shockwave has made the shear layer practically disappear, and the recirculation zone has been significantly reduced and is now very close to the spike, instead now there are clearly different shockwaves, one generated by the spike and another generated by the main body, thus partly defeating the purpose of the spike of shielding the main body. Lastly, there's a clear rise in temperature near the body surface at around 16° where the impingement of the shockwave on the body is located, this is due to the fact that the spike can no longer shield the body on this zone. The lower part of the body remains almost unaffected or the changes cannot be appreciated very well with this visualization, so they will be discussed later on the thermodynamic analysis plots.

Bodies Ring 1 and Ring 2 suffer most of the changes that the spiked body does, the shear layer and the recirculation zone have been reduced, however to a lesser extent, as the rings still provide the benefits of the spike up to a point by shielding the body

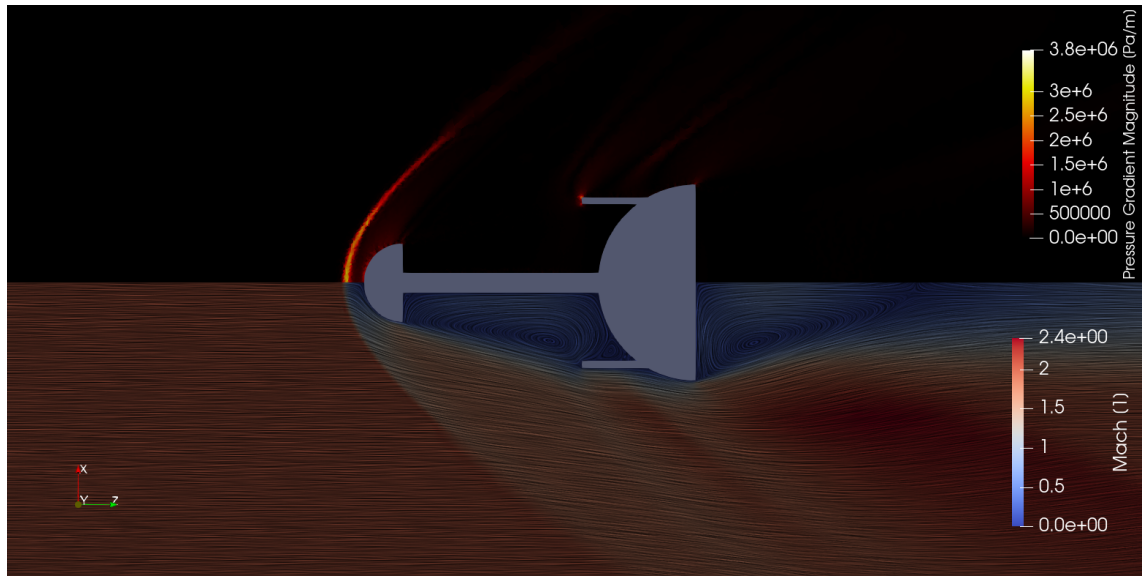


Figure 55: Pressure gradient and Mach number of ring 2 at Mach 2 with null AoA.

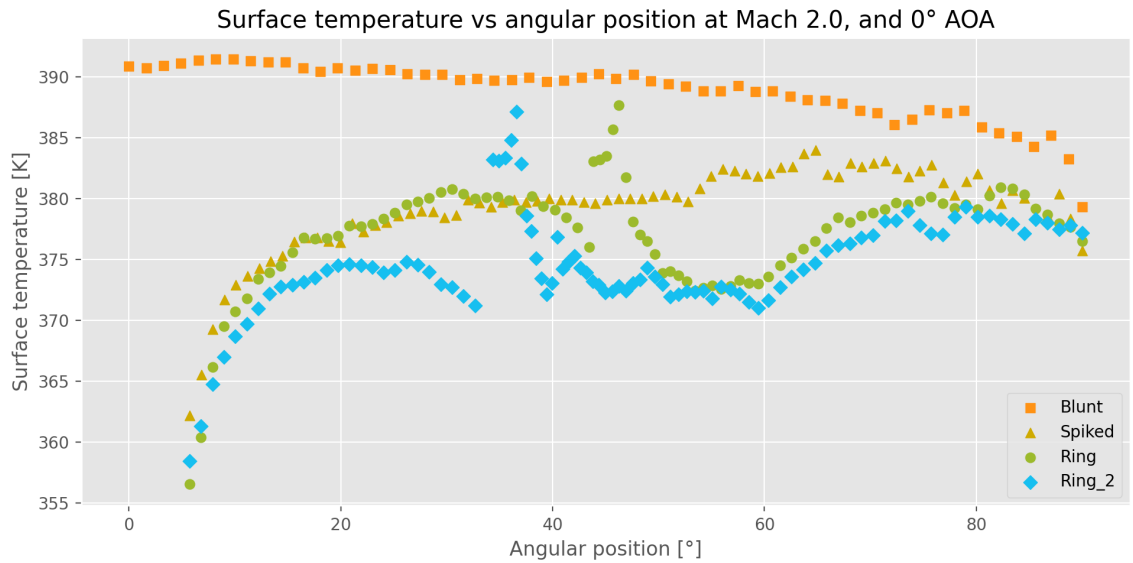


Figure 56: Fluid temperature on the body surface at Mach 2.0 and 0° AOA

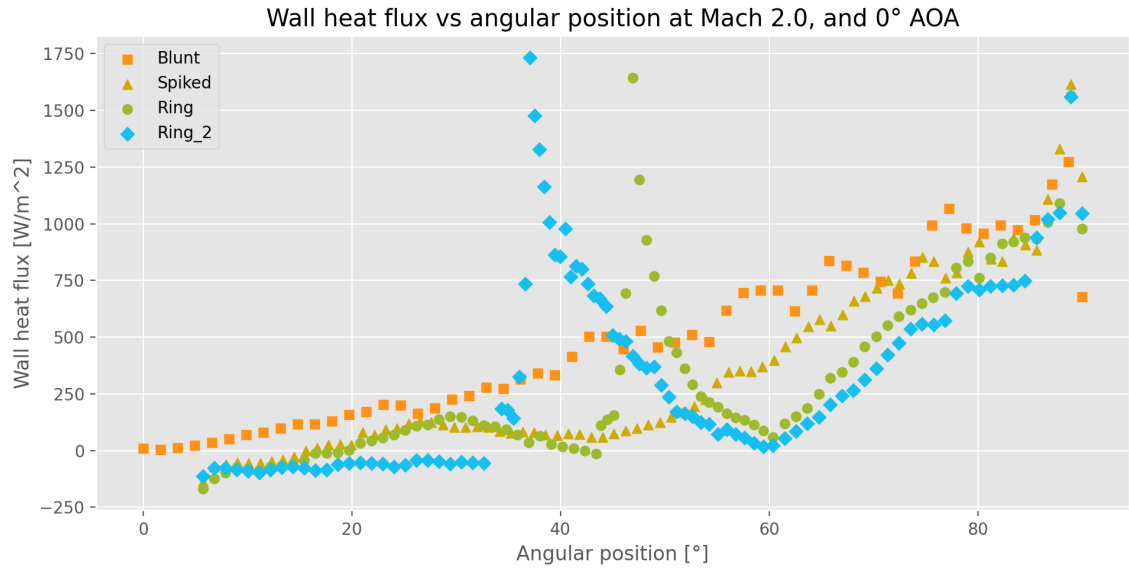


Figure 57: Wall heat flux at Mach 2.0 and 0° AOA

surface, this can be better appreciated on Ring 2 where the ring is longer so it protects more of the surface, this can also be seen in the vortex structure, where Ring 1 and Ring 2 still present the main vortex characteristic of a spiked body. However, even if a recirculation zone is still present and helps reduce the drag coefficient, at the root of the rings, a smaller recirculation zone has appeared, which in Ring 2, on the upper side, develops into a vortex, it can also be seen on the temperature profiles that in these same zones the temperature rises, this is due to the rings interfering with the flow of the fluid, causing the fluid to stagnate on even more surface than if the rings were not present, and added on to that the vortex formed here could be adding on to this effect via friction between the flow and the body, this effect can be really counterproductive if the objective of the ring and spike is to reduce the temperature.

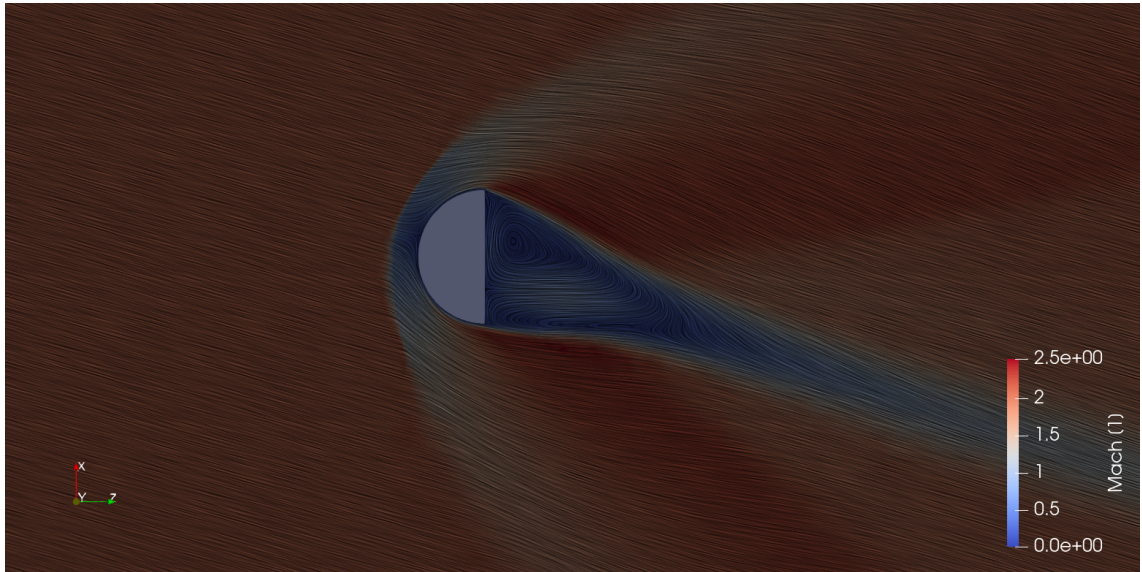


Figure 58: Mach number of Blunt Body at Mach 2 and 16° AoA.

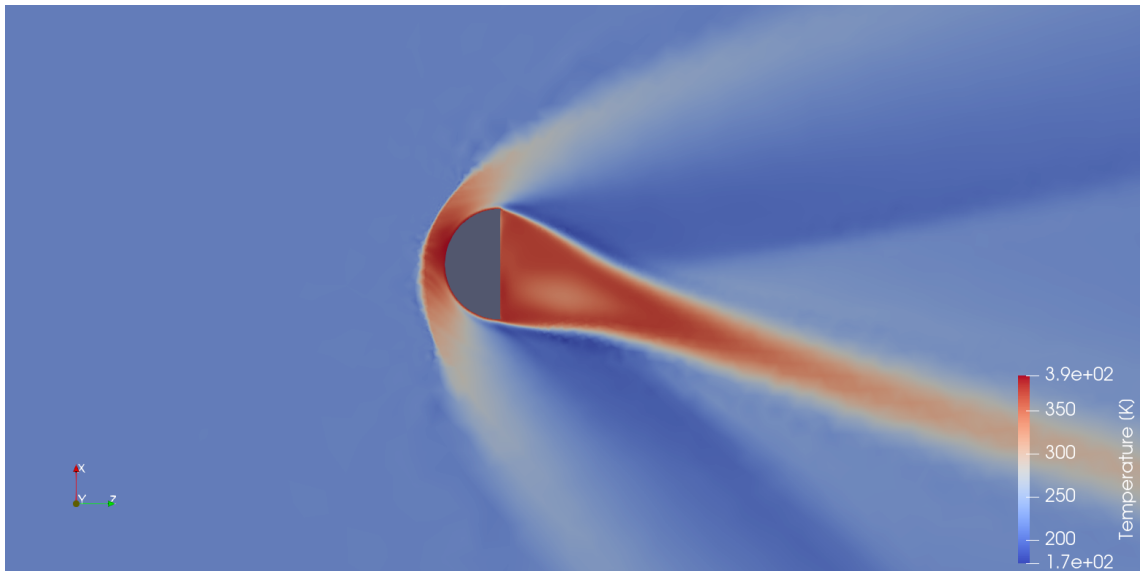


Figure 59: Temperature of Blunt Body at Mach 2 and 16° AoA.

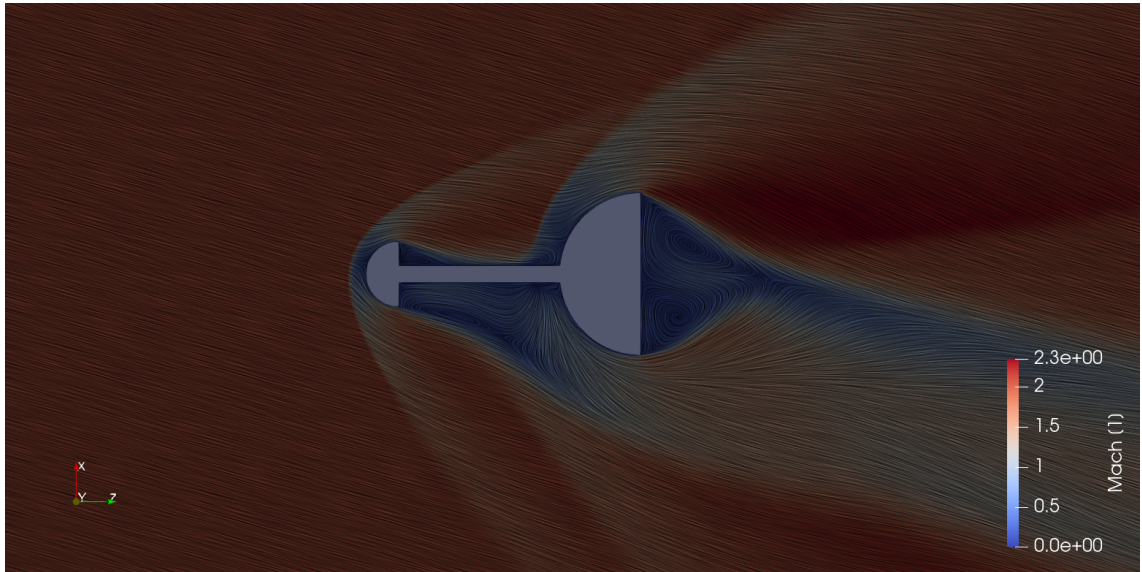


Figure 60: Mach number of Spiked Body at Mach 2 and 16° AoA.

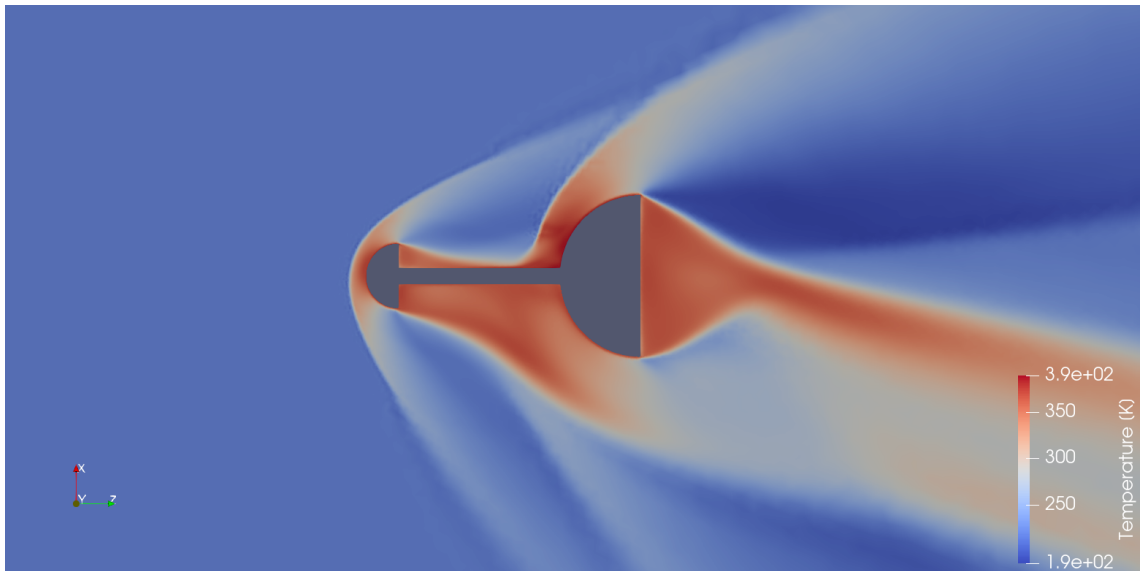


Figure 61: Temperature of Spiked Body at Mach 2 and 16° AoA.

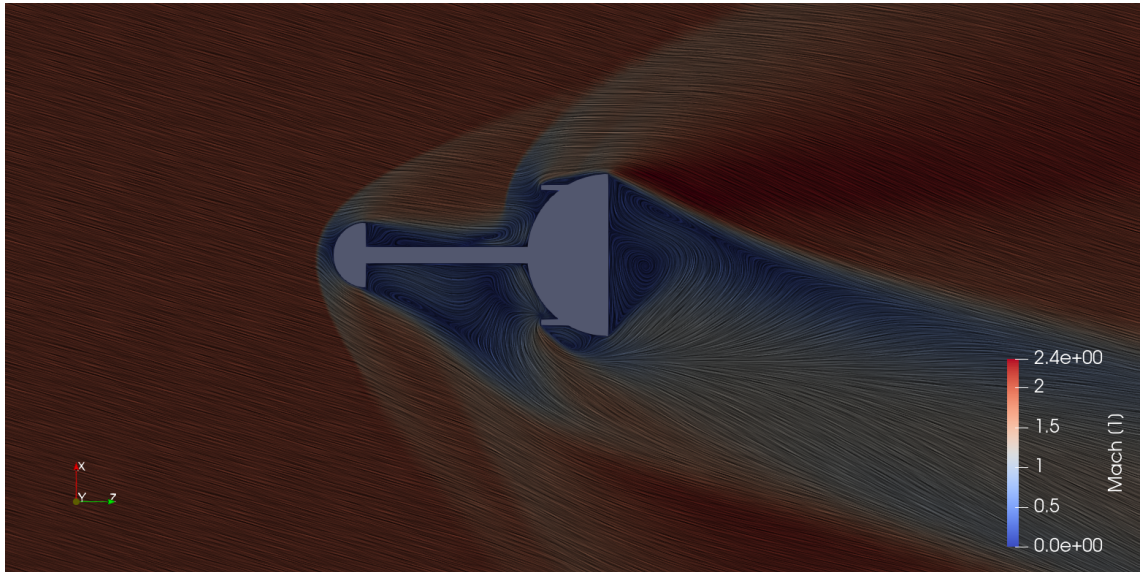


Figure 62: Mach number of Ringed Body 1 at Mach 2 and 16° AoA.

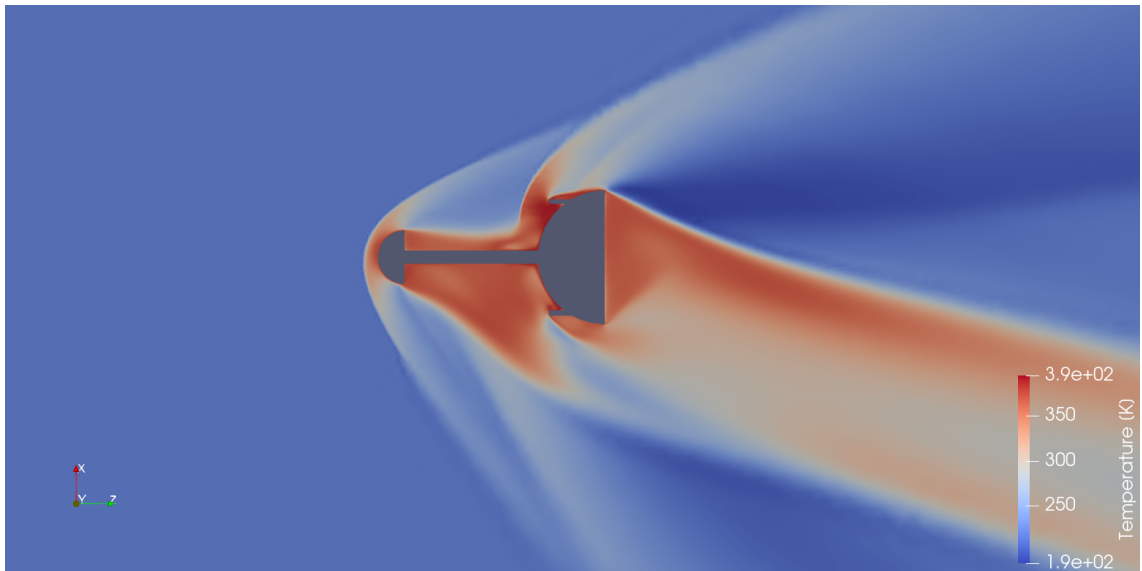


Figure 63: Temperature of Ringed Body 1 at Mach 2 and 16° AoA.

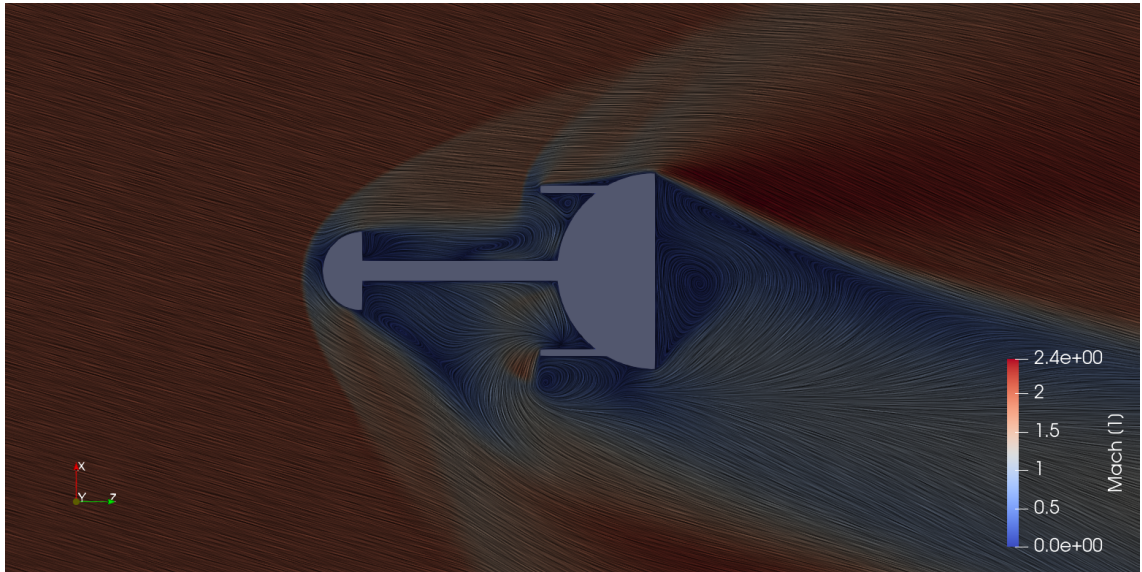


Figure 64: Mach number of Ringed Body 2 at Mach 2 and 16° AoA.

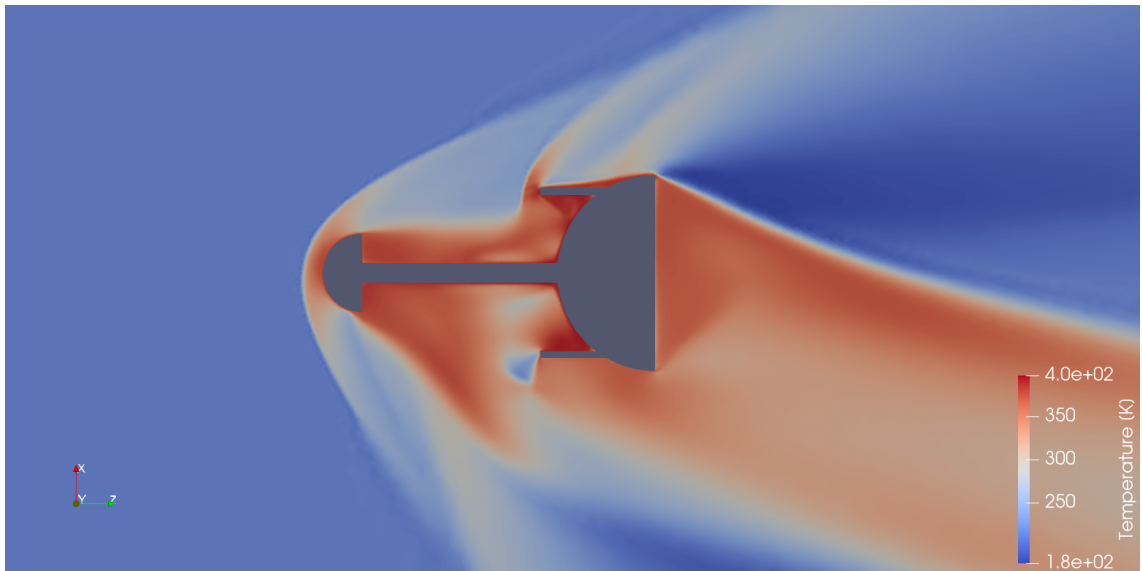


Figure 65: Temperature of Ringed Body 2 at Mach 2 and 16° AoA.

Regarding the surface fluid heat flux contours on figures [66-69](#), it can be seen that the areas of negative heat flux tend to be wider on the lower side of the bodies, this is due to the fact that the recompression effects that cause high temperatures and heat flux on the shoulders of the bodies are now present higher upstream on the lower side (and theoretically lower upstream on the upper side, but this can't be seen in these cases as there is no more surface for it to be visible) because the shape of the shockwaves has shifted, and thus the recompression affects a bigger surface. This can be easily appreciated on the blunt and spiked bodies, where the negative heat flux on the lower side of the aeroshield and the main body is wider than those areas on the upper side. Moving on to the three spiked bodies, they now show concentrated heat flux on the upper spike root surface, this is most probably due to main body shockwave colliding with the spike surface. In the case of the two ringed bodies, there is also a concentration of heat flux on the surface of the ring, both on the lower and on the upper side, and on the main body upper surface, this is happening because, as it was mentioned before, at this angle of attack the ring is still shielding the main body by working as a spike, as a result the ring is breaking shockwaves into a weaker system of shockwaves, both on the upper and lower side, thus getting heated, and making the shockwaves collide with the main body on a small surface around the ring. It can be deduced that these body-shockwave interactions would be stronger at greater Mach numbers, thus reinforcing the previous statement that the effective angle range for the spike and the rings would be smaller at greater Mach numbers. These interactions can be better appreciated on figures [70-73](#). On the blunt body contour it can be seen how the shockwave has shifted accordingly to the angle of attack, on the spiked body contour it can be clearly observed the way the shockwave collides on the spike surface, and on the ringed body contours the way the ring decomposes the shockwave into a system of weaker ones that collide with the main body can be distinctly appreciated, thus corroborating the reason for the appearance of the heat zones on the spikes' surfaces and the main bodies' surfaces. It can also be seen, in the case of the ringed bodies, how the lower side of the rings decomposes the recompression shockwave, which is why there's no negative heat flux zone on the lower body shoulders of the ringed bodies, as opposed to the ringless bodies.

Before discussing the surface temperature and wall heat flux plot it's worth noting that as the flow is no longer axisymmetric, the plots now show the 180° degrees of the body surface, except for the spike surface, which is why all the plots, except for the blunt body plot, show no information around 0°, instead of only 90° degrees like in the previous plots, so the negative values represent the lower side of the body, and the positive values represent the upper side of the body.

Observing the Surface temperature plot on figure [74](#), the previously mentioned effects can be confirmed. The temperature along the blunt body surface barely differs, except for the lower side of the body where it drops slightly. The spiked body shows lower temperatures than the blunt body all along the main body surface, even on the upper side where they're higher because of the angle of attack, proving it may still be useful even at this inclination. Regarding both ringed bodies, they both show greater temperatures values than the blunt body around the root of the spike, meaning around

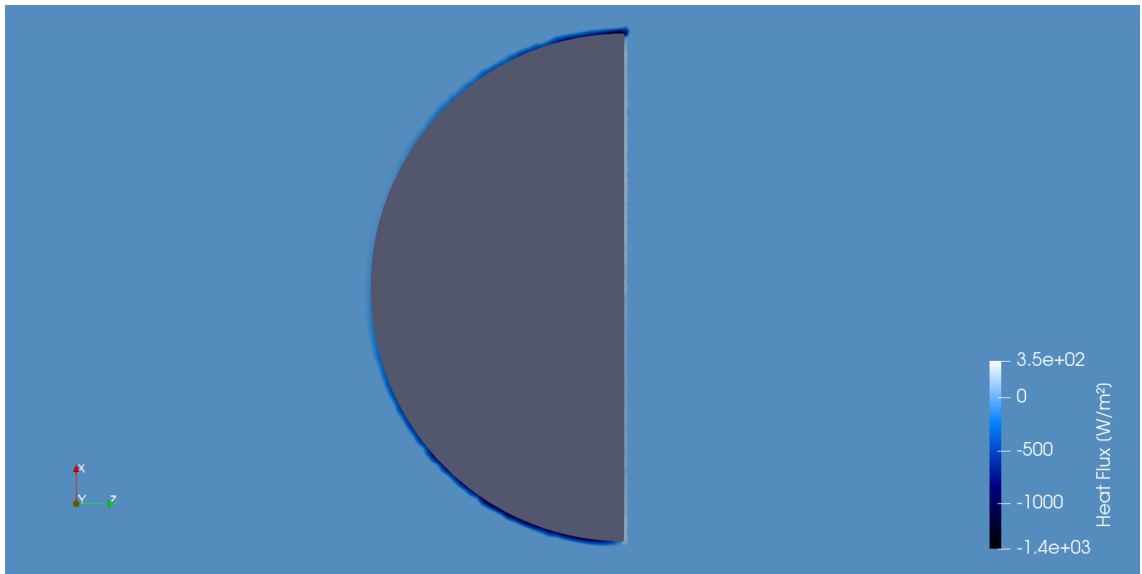


Figure 66: Surface Fluid Heat Flux of Blunt Body at Mach 2 and 16° AoA.



Figure 67: Surface Fluid Heat Flux of Spiked Body at Mach 2 and 16° AoA.



Figure 68: Surface Fluid Heat Flux of Ringed Body 1 at Mach 2 and 16° AoA.



Figure 69: Surface Fluid Heat Flux of Ringed Body 2 at Mach 2 and 16° AoA.

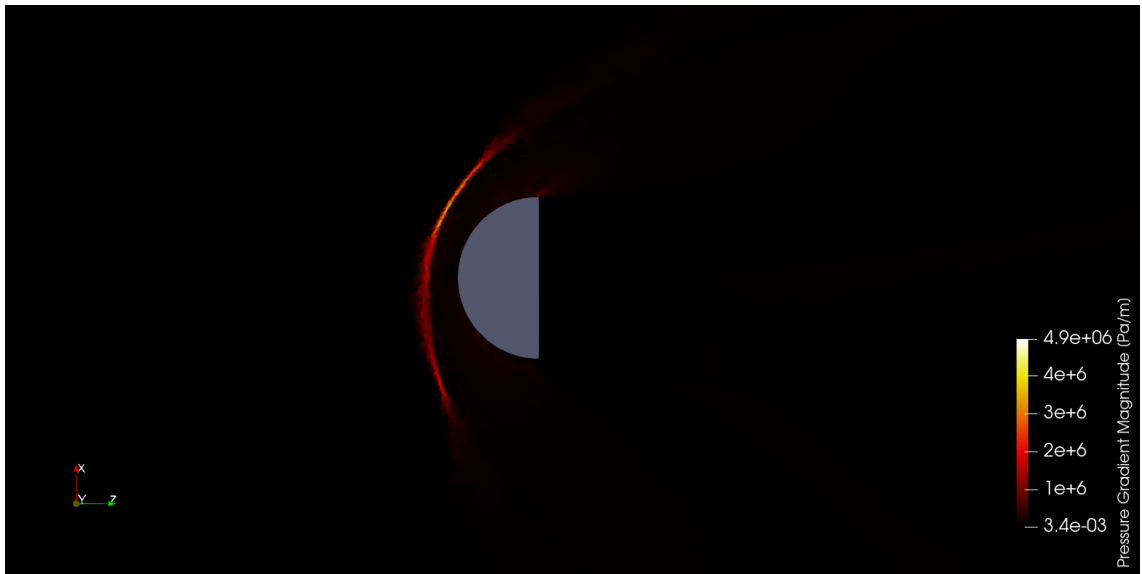


Figure 70: Pressure Gradient of Blunt Body at Mach 2 and 16° AoA.

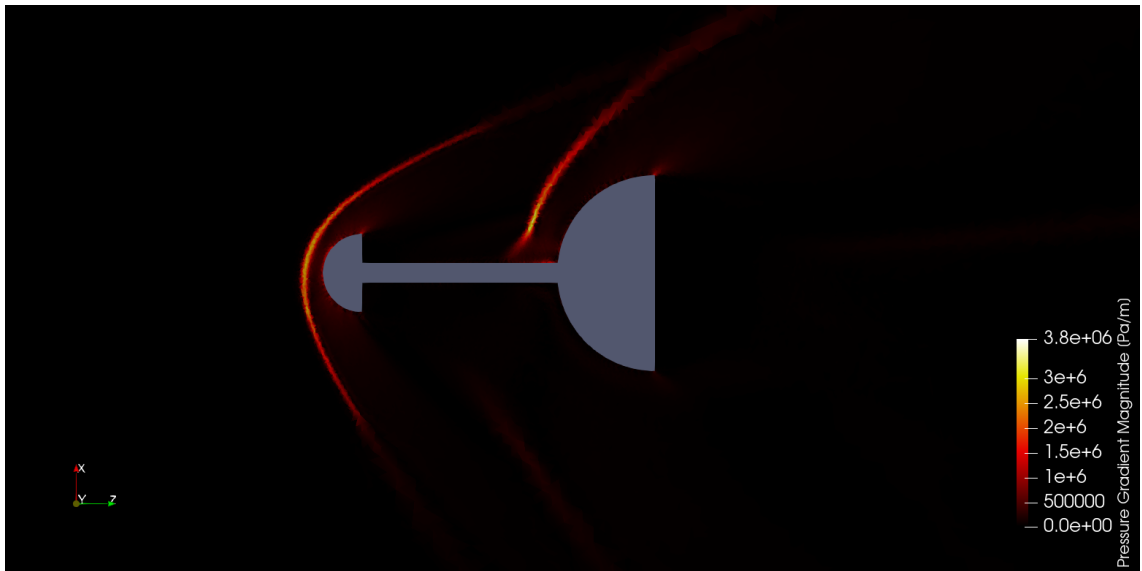


Figure 71: Pressure Gradient of Spiked Body at Mach 2 and 16° AoA.

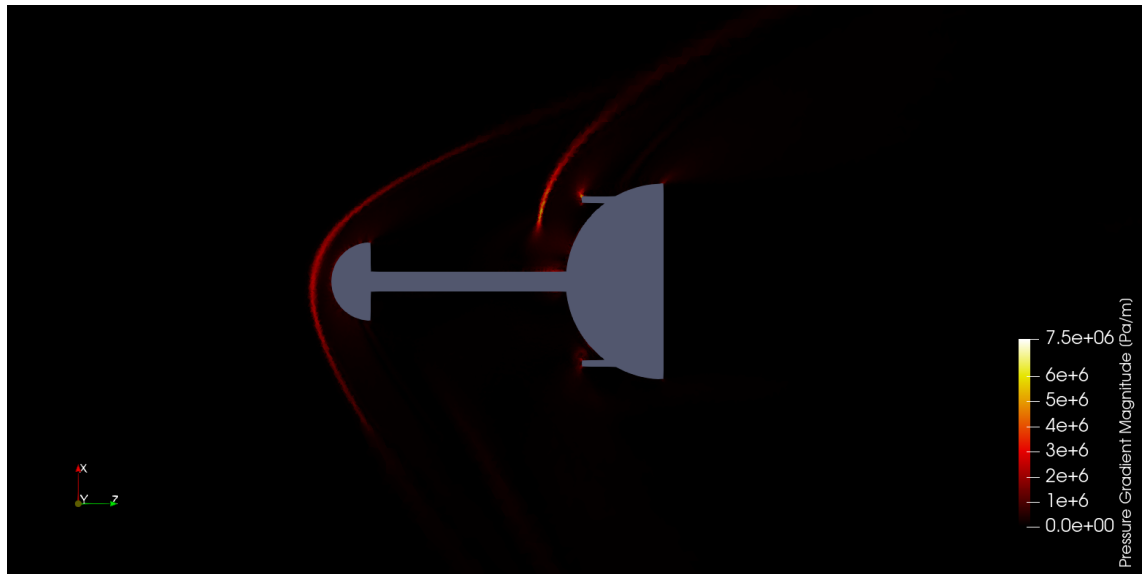


Figure 72: Pressure Gradient of Ringed Body 1 at Mach 2 and 16° AoA.

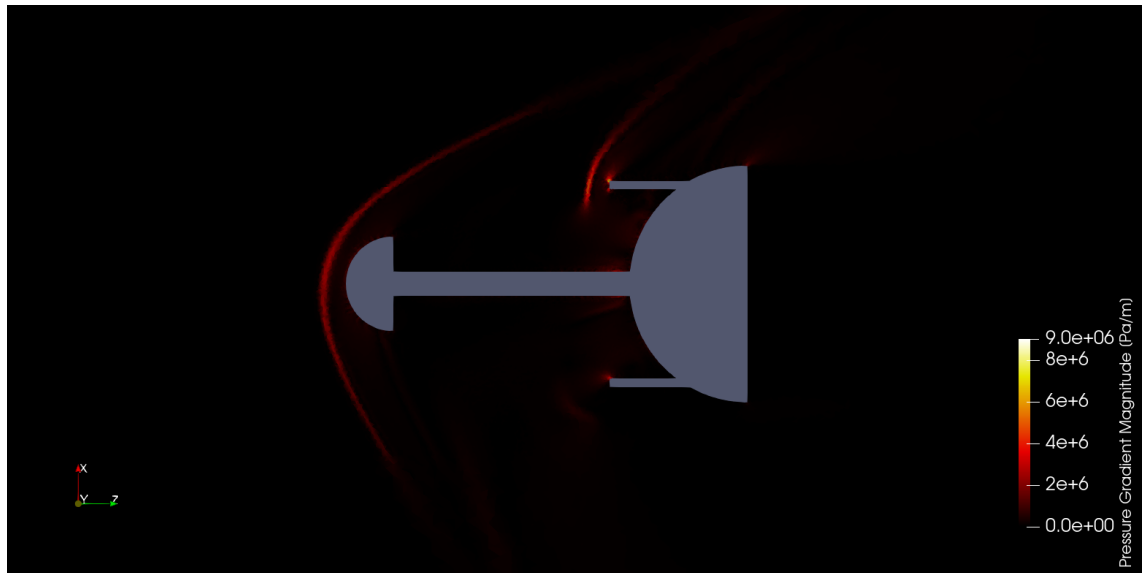


Figure 73: Pressure Gradient of Ringed Body 2 at Mach 2 and 16° AoA.

0°, on the upper side because of the impingement of the shockwave, and on the lower side due to stagnation of the flow, these values start decreasing on both sides as they approach the ring surface (the Ring 1 and Ring 2 bodies rings surface start around 50° and 40° respectively), and then rise again as they approach the body shoulder. The temperature on the upper side of the bodies is higher than on the lower side because of the shockwave colliding there due to the angle of attack.

Moving on to the wall heat flux plot on figure [75](#), the blunt body presents an almost null heat flux at the stagnation point (16°), and from there the heat flux starts rising on both directions. The spiked body presents a similar distribution, where the heat flux starts rising from the center of the plot, however said heat flux is lower than that of the blunt body on the lower side of the body, and higher than that of the blunt body on the upper side, this puts into question the thermodynamic performance of the spike at this angle of attack. Both ringed bodies present a rise in heat flux from the center of the plot, which decreases only to suddenly rise and drop again (mostly on the upper side) at the surface of the ring, the heat flux then starts rising as the position approaches the body shoulders. This initial high heat flux rise could be due to the previously mentioned effect of the shockwave collision on the body, it seems that the reduction effects caused by the expansion generated by the rings have trouble overcoming the effects caused by shockwave collision. It's also worth noting that these plots don't show neither the temperature nor the heat flux on the inner surface of the main body near the root of the ring, where the vortex start forming, this zone could also present high temperatures and heat fluxes, thus rendering the overall performance of the rings worse.

Finally, it's worth noting that the rings could still be considered useful, in thermodynamic terms, because the temperature and heat flux values are still lower than those of the blunt and spiked bodies on most of the surface, however it can be observed that even if at this angle of attack (16°) the Ring 2 body had a lower drag coefficient than the Ring 1 body, it's debatable if its thermodynamic performance, and thus overall performance, is better than that of the Ring 1 body, because its temperature and heat flux values were considerably higher in some zones and then slightly lower on others. Therefore even at this angle it can be deduced that the thermodynamic performance of the ring decreases as the angle of attack increases at a greater rate the longer the length of the ring is.

4.4.4 Results at 30°

Figures [76](#)-[83](#) show the Mach number and temperature contour profiles for each of the bodies at a 30° angle of attack. Again, these two type of profiles are presented together as a lot of the information they show is similar. Starting with the blunt body, again the detached bow shockwave has simply rotated slightly according to the angle of attack, and naturally the highest fluid temperature is located at the stagnation point, besides that, these two profiles don't show much important information and serve more as a reference for the other bodies.

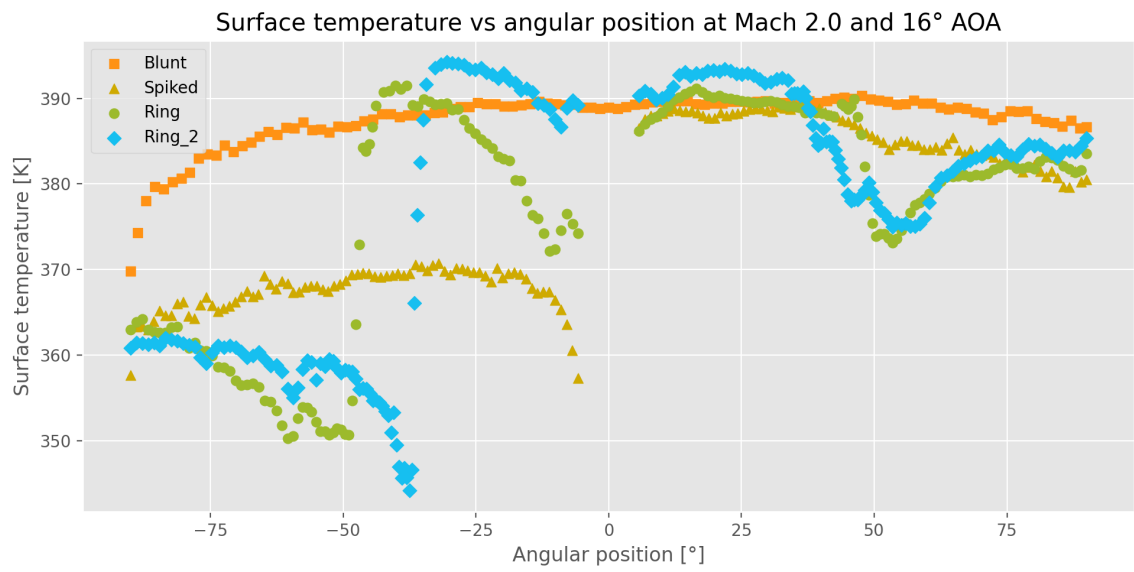


Figure 74: Fluid temperature on the body surface at Mach 2.0 and 16° AoA

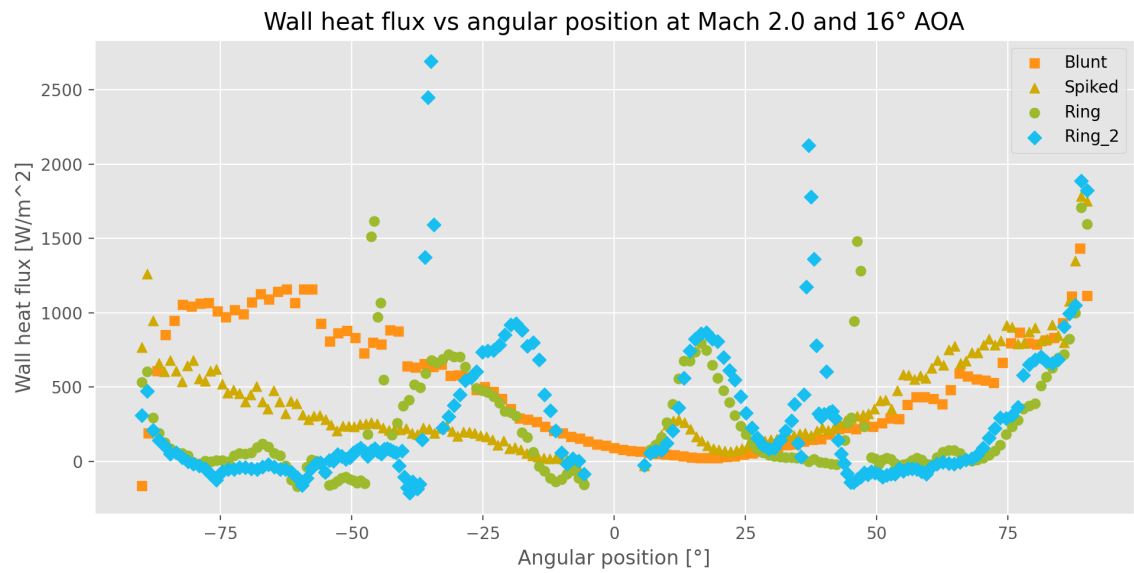


Figure 75: Wall heat flux at Mach 2.0 and 16° AoA

Continuing with the Spiked body, the recirculation zone on the upper side of the body has practically disappeared, and although it remains in a way on the lower side of the body it's not as favorable as in a null angle of attack as the recirculation streamlines are completely deformed. Because the spike is practically not shielding the main body anymore two very visible shockwaves can be observed, one caused by the aeroshield and another caused by the main body, less visible shockwaves caused by the aerospike still decomposing the main shockwave into smaller weaker ones can also be seen. High fluid temperatures can be seen around the stagnation points of the main body and the spike.

Moving on to the ringed bodies, it can be easily observed that they too have lost their recirculation zones, the Ring 2 body's ring still seems to be shielding the main body and creating a small recirculation zone, however, the drag coefficient plot (figure 53) shows that at this angle the Ring 2 body's drag coefficient is higher than that of the blunt body, so it can be deduced that the small reduction the ring could bring is surpassed by the increment of the projection area it causes. Just as the Spiked body, these two bodies' have two distinct shockwaves caused by the main body and the spike, the spikes still cause multiple weak shockwaves to appear, the highest fluid temperatures can be observed on the stagnation points, and a sort of recirculation zone, identified by the low Mach number and temperature, can be observed on the lower side of the body due to the recompression effects. Again, the benefits that the small recirculation zones observed on the lower side of the ringed bodies could bring are overcome by the increment of the reference area that the rings have caused, at this angle both rings can be considered counterproductive in drag reduction terms, as both ringed bodies' drag coefficients are higher than those of the Spiked body, and the Ring 2 body's drag coefficients is even greater than that of the blunt body. Moreover both ringed bodies present high temperatures on the inner surfaces of the main body and the ring, this is due to the stagnation of the fluid on the main body surface, this effect is not as prevalent on the Spiked body, this is because on the ringed bodies the rings themselves are obstructing the flow of the fluid, which leads to the fluid stagnating on even more surface of the body, added to that the vortex generated on these zones could be adding to the effect via skin friction, this too is counterproductive for the the rings, whether or not the rings could still be considered useful in thermodynamic terms will be discussed when the thermodynamic plots are analyzed.

Figures 84 - 87 show the surface fluid heat flux contour profiles for each body at a 30° angle of attack. The blunt body profile presents most of its heat flux on the lower side of the body, this is due to the recompression effects shifting upstream due to the shape of the shockwave also shifting due to the angle of attack. As for the spiked body, the main thing to note is that the negative heat flux zone on the spike surface has increased, this is caused by the shockwave impinging on even more surface due to the pronounced angle of attacked. Additionally, when compared to its null angle of attack equivalent on figure 43 it can be noted that the thermodynamic performance of the spike has gotten significantly poorer, while the contour at a 0° angle of attack shows most of its negative heat flux (meaning heat transferred to the body) on the aeroshield

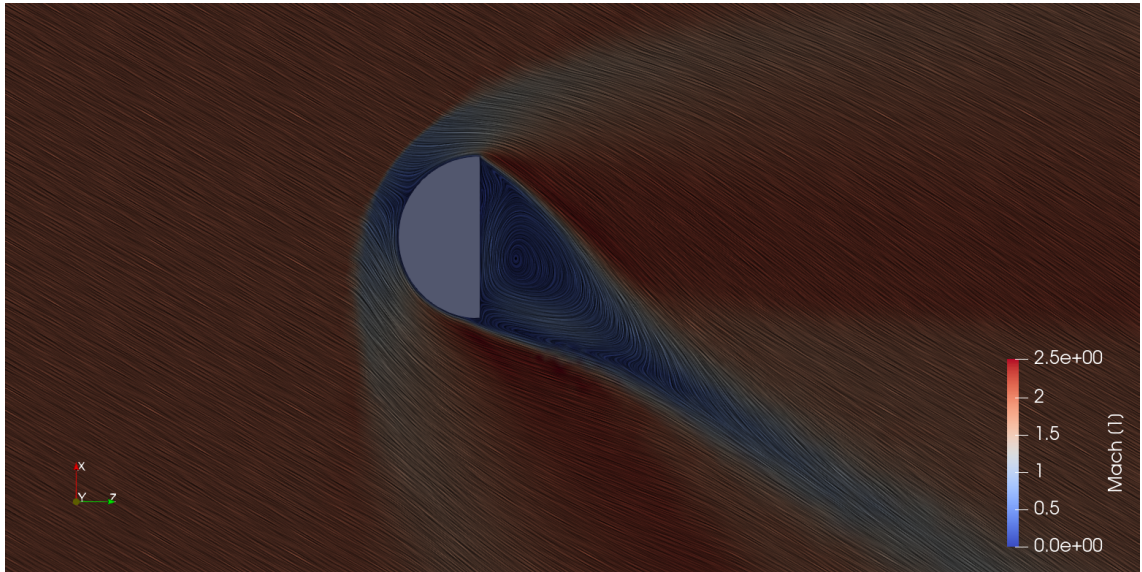


Figure 76: Mach number of Blunt Body at Mach 2 and 30° AoA.

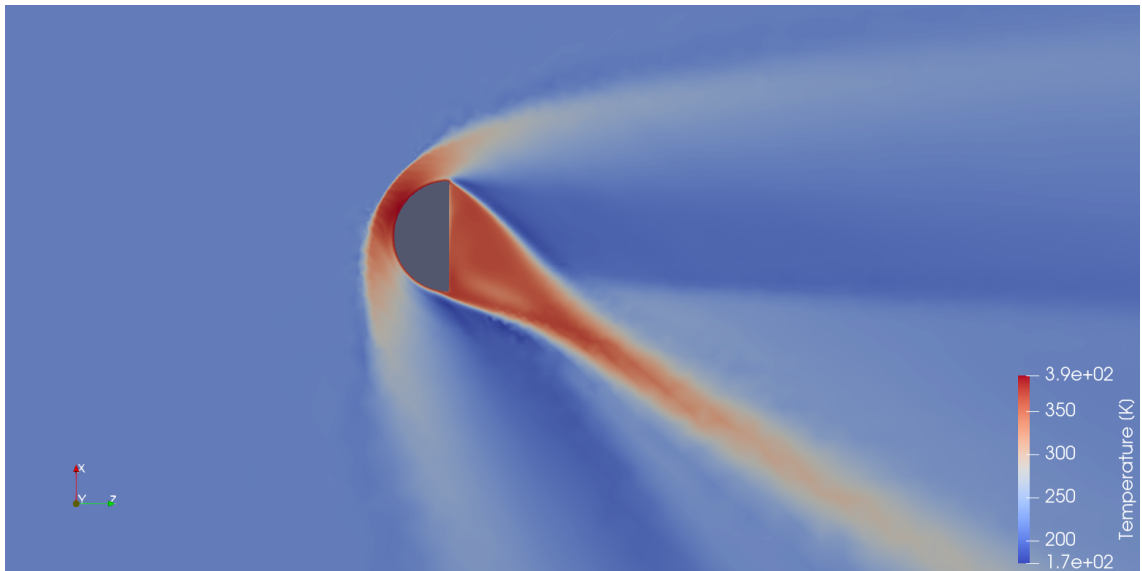


Figure 77: Temperature of Blunt Body at Mach 2 and 30° AoA.

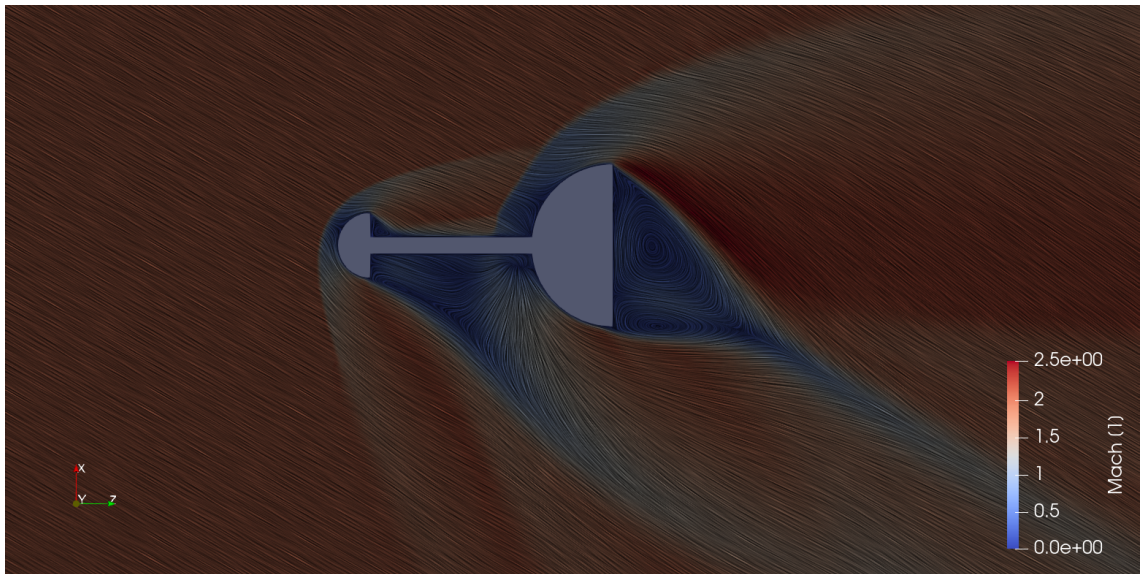


Figure 78: Mach number of Spiked Body at Mach 2 and 30° AoA.

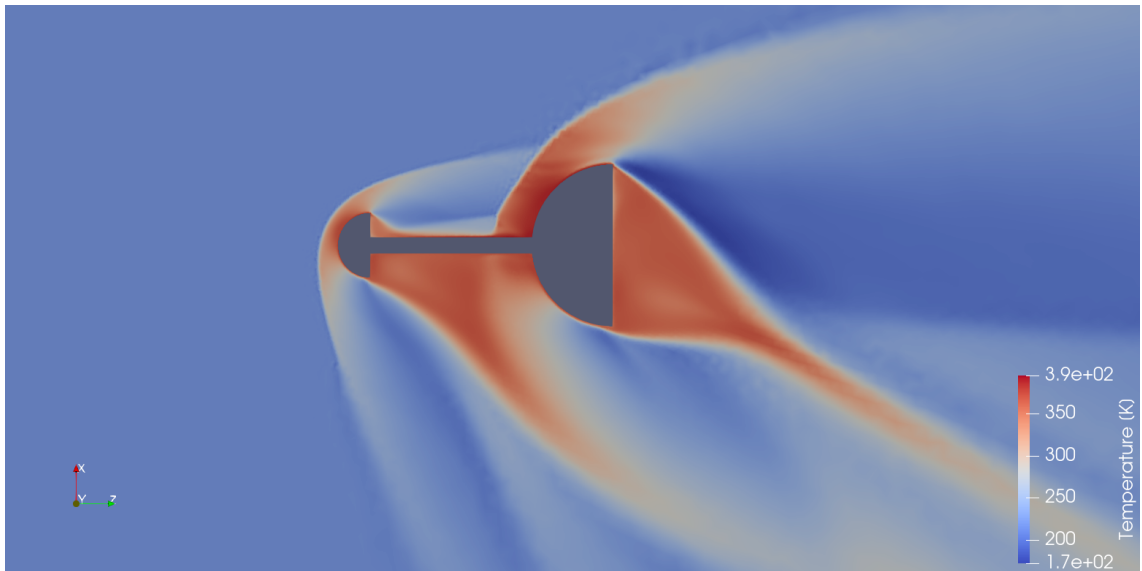


Figure 79: Temperature of Spiked Body at Mach 2 and 30° AoA.

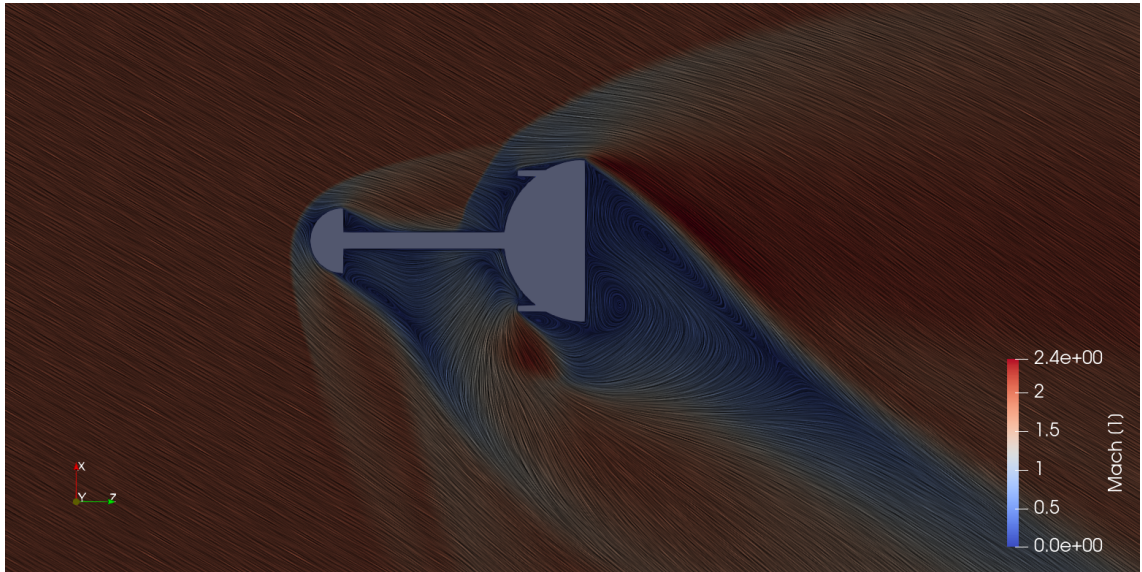


Figure 80: Mach number of Ringed Body 1 at Mach 2 and 30° AoA.

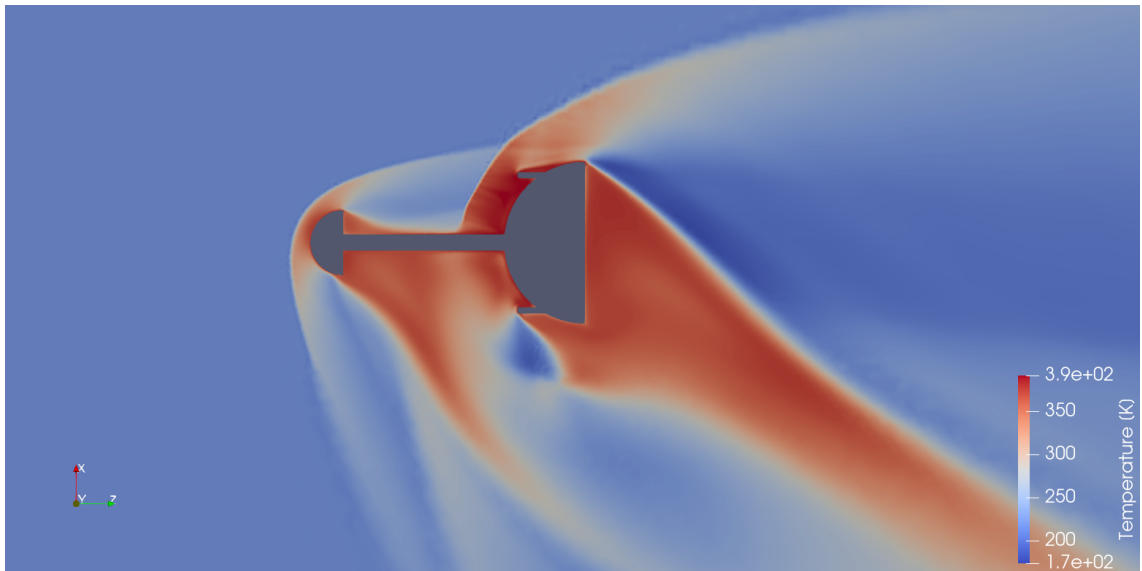


Figure 81: Temperature of Ringed Body 1 at Mach 2 and 30° AoA.

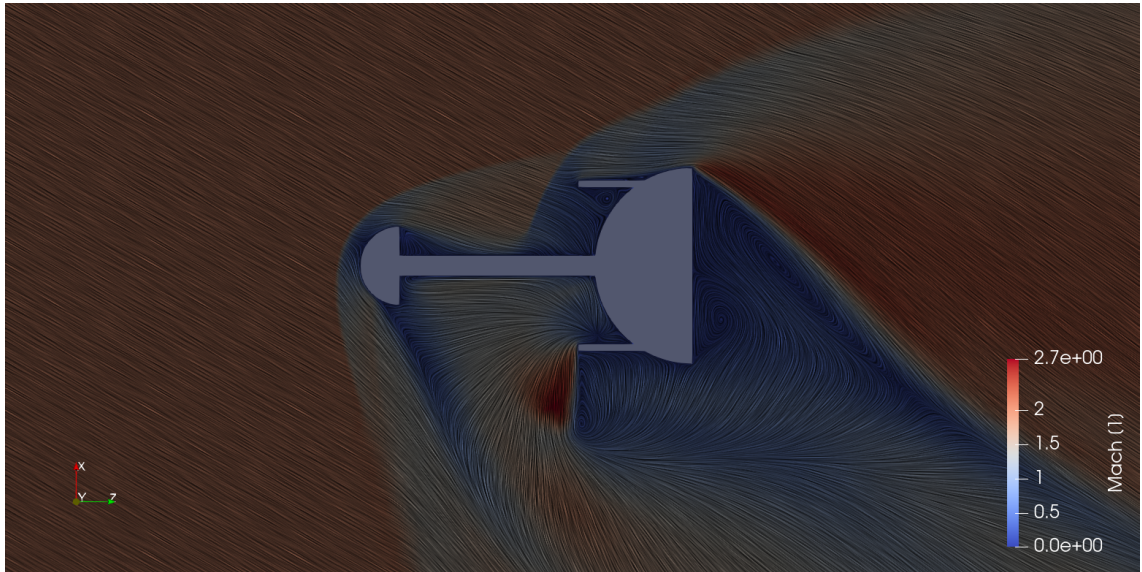


Figure 82: Mach number of Ringed Body 2 at Mach 2 and 30° AoA.

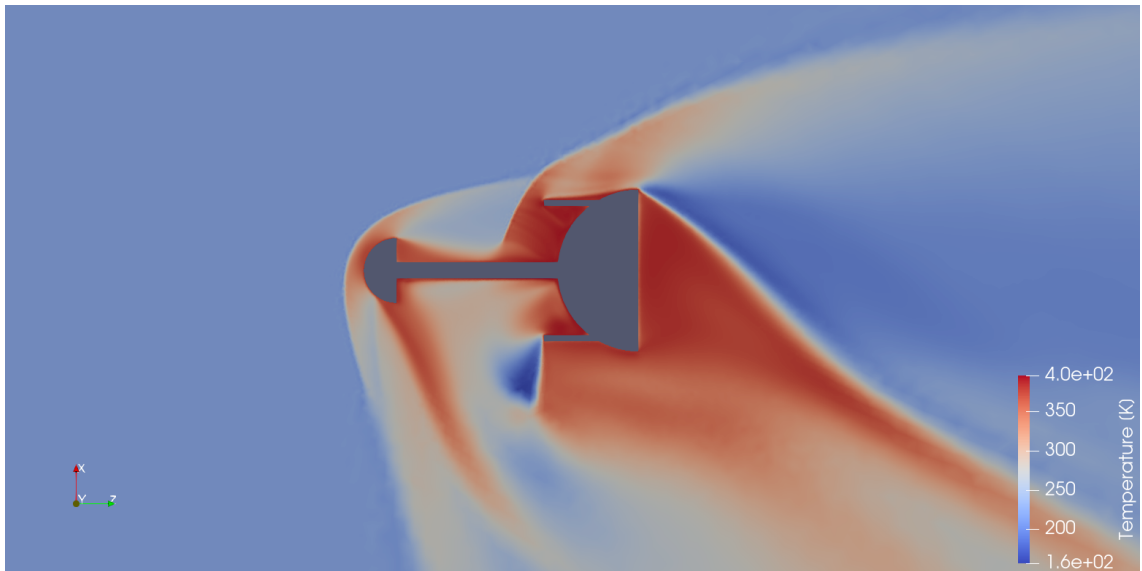


Figure 83: Temperature of Ringed Body 2 at Mach 2 and 30° AoA.

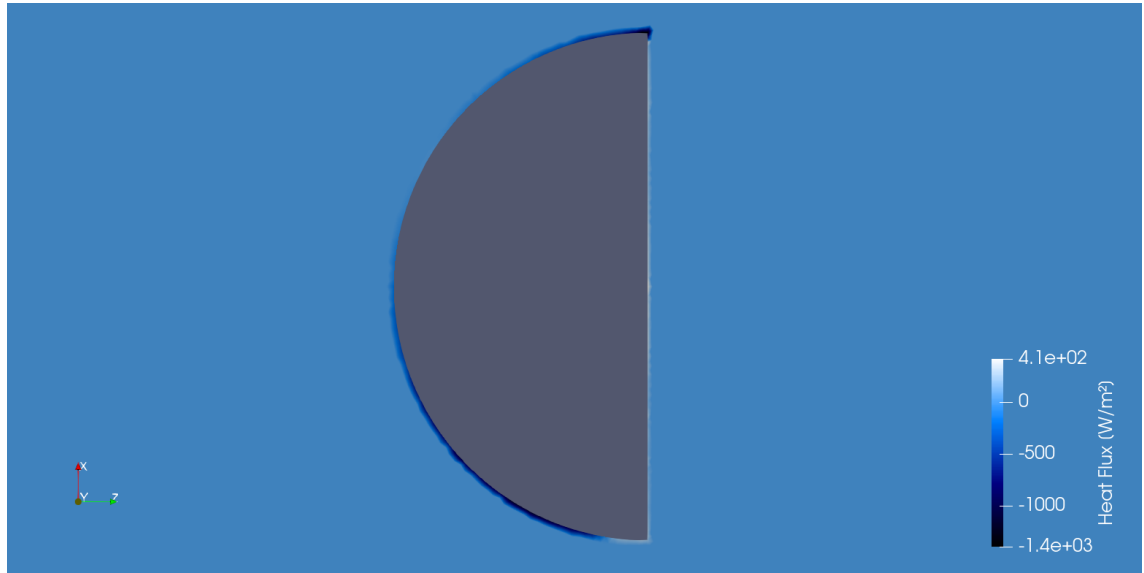


Figure 84: Surface Fluid Heat Flux of Blunt Body at Mach 2 and 30° AoA.

surface and the main body shoulder, the 30° degree angle of attack case on figure [85](#) shows a lot more negative heat flux on the main body surface, which is exactly the zone the spike aims to protect.

The ringed bodies also show negative heat flux on the aeroshield surface, on the spike surface and on the upper shoulder surface, (seen on figures [81](#) and [83](#)), however, they do not present much negative heat flux on the main body, meaning that even if the rings at this angle are being counterproductive in terms of drag reduction, the small recirculation zones they cause are still protecting the main body in temperature and heat flux terms, this negative heat flux is instead being concentrated on the ring surface. Whether or not this means that at this angle of attack the rings can still be considered useful or not will be discussed on the thermodynamic plots analysis.

Figures [88](#) - [91](#) show the pressure gradient contour profiles for each body at a 30° angle of attack. The blunt body contour shows a simple shift in the shockwave due to the angle of attack, and it's shown mainly for reference purposes.

The spiked body contour presents two strong and clearly visible shockwaves, one caused by the aeroshield and another one caused by the main body, this last shockwave seems to collide with the spike's surface and is the reason why there's a concentration of negative heat flux on this zone, as can be seen on figure [85](#), as the fluid gets significantly hot near the spike's surface. Other weaker shockwaves can be seen as a results of the spike shockwave decomposition mechanism and they're the reason for the low Mach number zones on the lower side of the body, visible on figure [78](#). Even at this angle the mechanism of the spike seems to be effective as figure [53](#) clearly shows that the Spiked body has a lower drag coefficient than the Blunt body.

Moving on to the ringed bodies, they present two strong shockwaves caused by the aeroshield and the upper side of the ring, regarding the latter shockwave, it can be

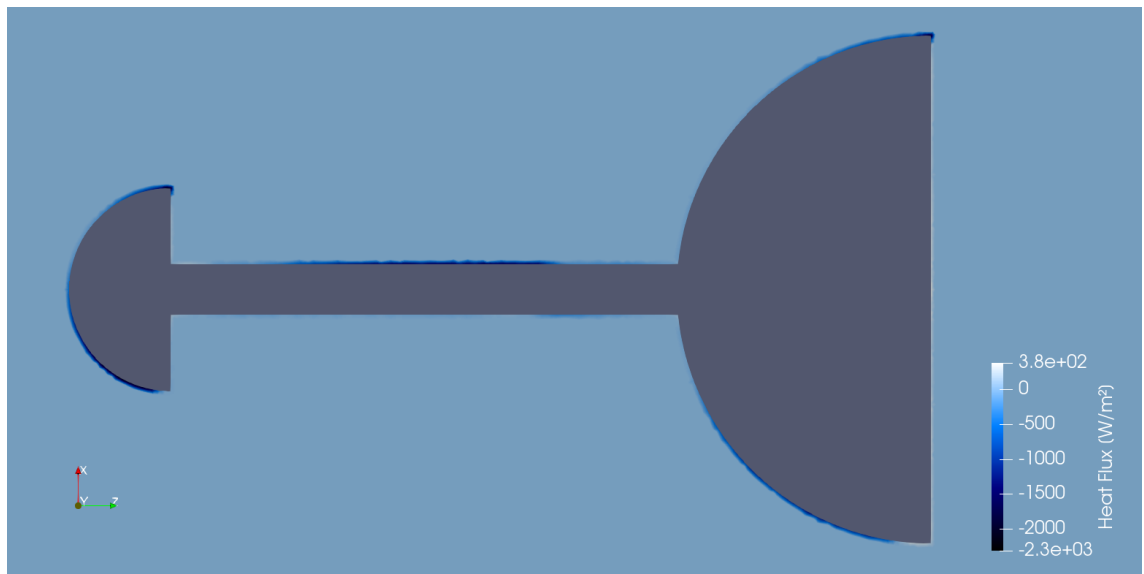


Figure 85: Surface Fluid Heat Flux of Spiked Body at Mach 2 and 30° AoA.

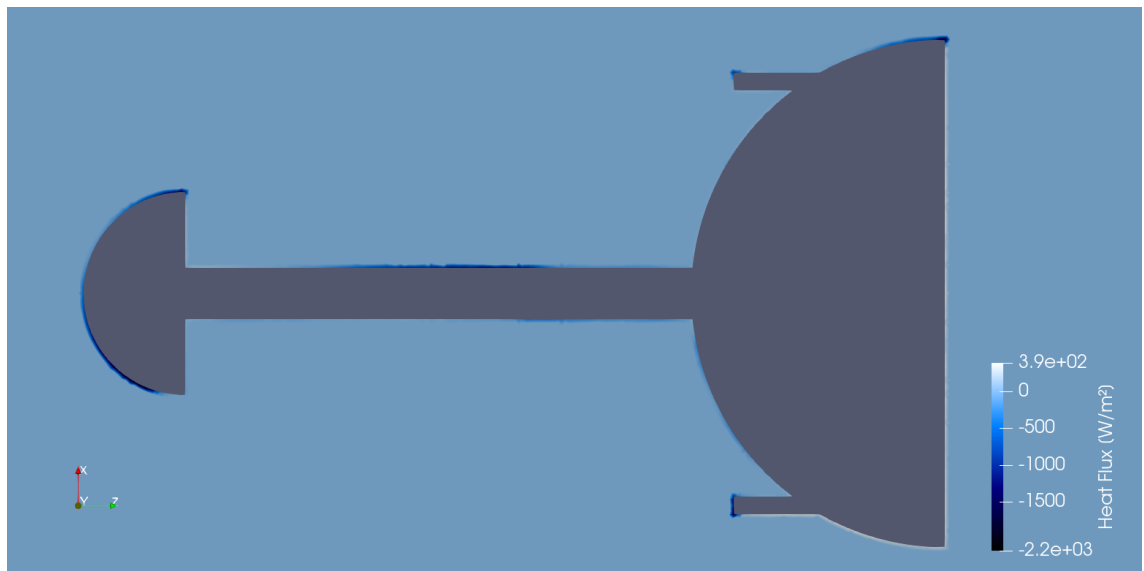


Figure 86: Surface Fluid Heat Flux of Ringed Body 1 at Mach 2 and 30° AoA.

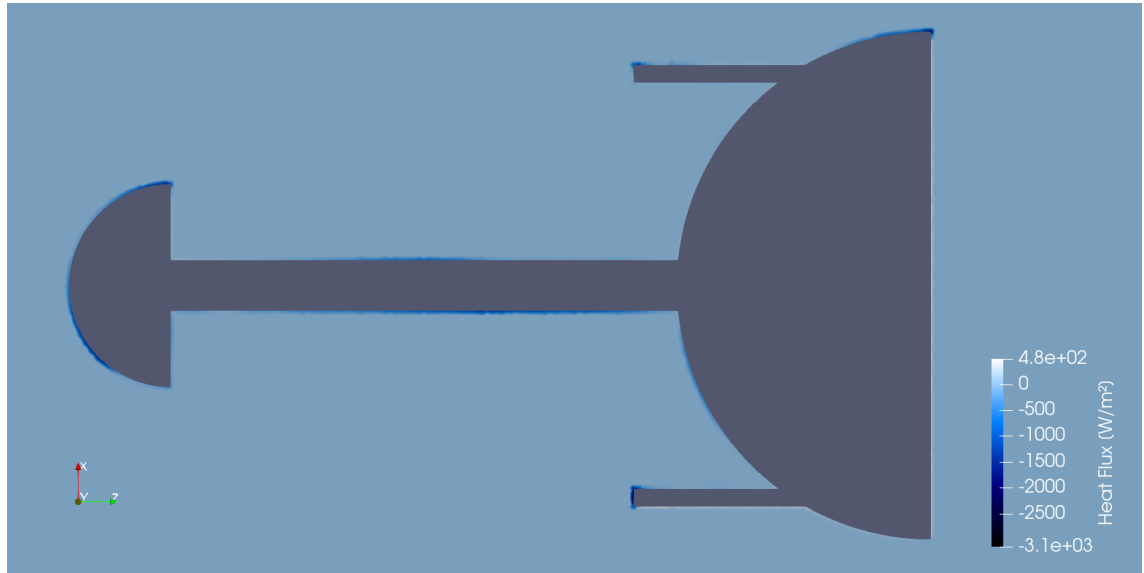


Figure 87: Surface Fluid Heat Flux of Ringed Body 2 at Mach 2 and 30° AoA.

seen that due to the length of the Ring 2's ring being longer, this shockwave does not completely collide with the spike surface, and that is the reason why it doesn't present a concentration of negative heat flux on this zone (seen on figure 87), as opposed to the Spiked body and Ring 1 (seen on figures 85 and 86, respectively). The two show the spike's shockwave decomposition mechanism causing weaker shockwaves to appear and generating low Mach number zones, however, as mentioned before, this drag reduction mechanism is surpassed by the rings causing the body to have an overall greater projection area and thus a greater drag coefficient than the Spiked body.

Figure 92 shows the temperature of the four different bodies along the main body surface at a 30° angle of attack. As expected, all bodies present higher temperature on their upper sides due to the angle of attack causing their stagnation points and shockwaves to shift there. The blunt body's temperature fluctuates only slightly except on the lower side where it drops to a small degree. The three spiked bodies show their temperatures rise and then drop around the spikes' roots, however, the ringed bodies' temperatures rise significantly more due to the previously discussed stagnation zones created by the rings themselves, these temperatures then decrease significantly because of the presence of the rings, whose surface is not as hot because the fluid only stagnates on one point, the temperature then seems to start rising again when approaching the body shoulders, due to the recompression effect that always presents itself in these areas. The Spiked body presents a lower temperature than the Blunt body all along its surface, and it's worth noting that when compared to its null angle of attack counterpart on figure 56 it can be seen that the temperatures have now shifted to be higher on the main body surface than on the body shoulder, when previously the opposite was true, this shows that the stagnation effects caused by the angle of attack have become greater than the recompression effect that takes place on the body shoulder due to the

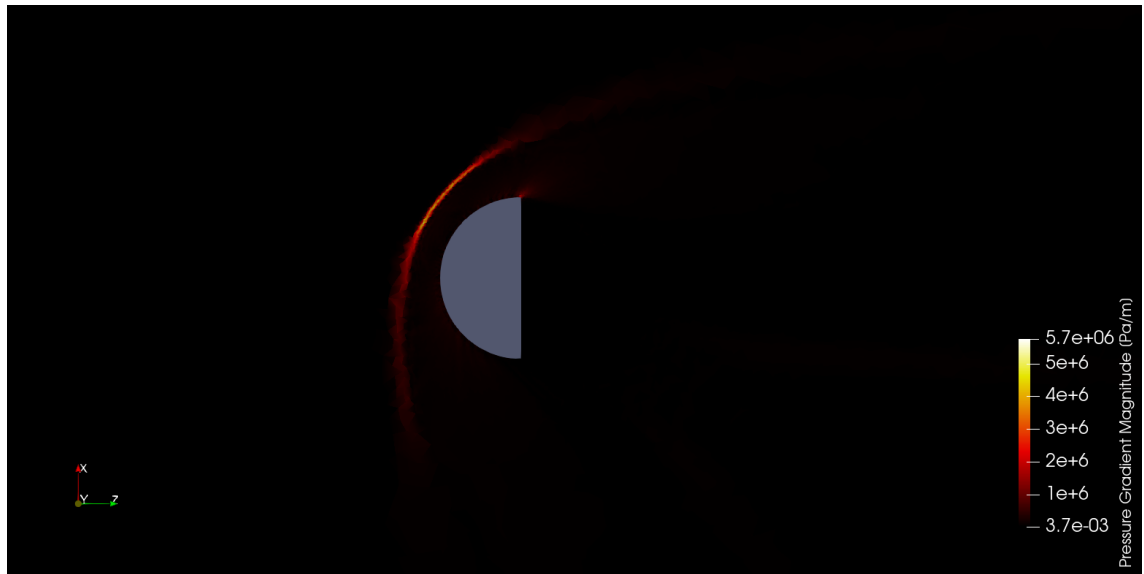


Figure 88: Pressure Gradient of Blunt Body at Mach 2 and 30° AoA.

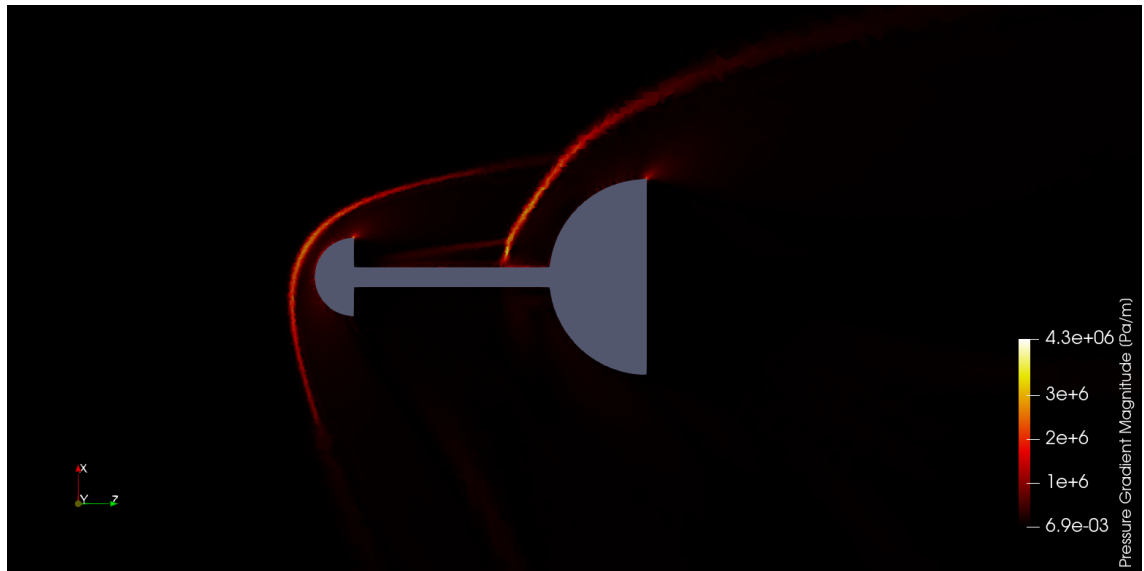


Figure 89: Pressure Gradient of Spiked Body at Mach 2 and 30° AoA.

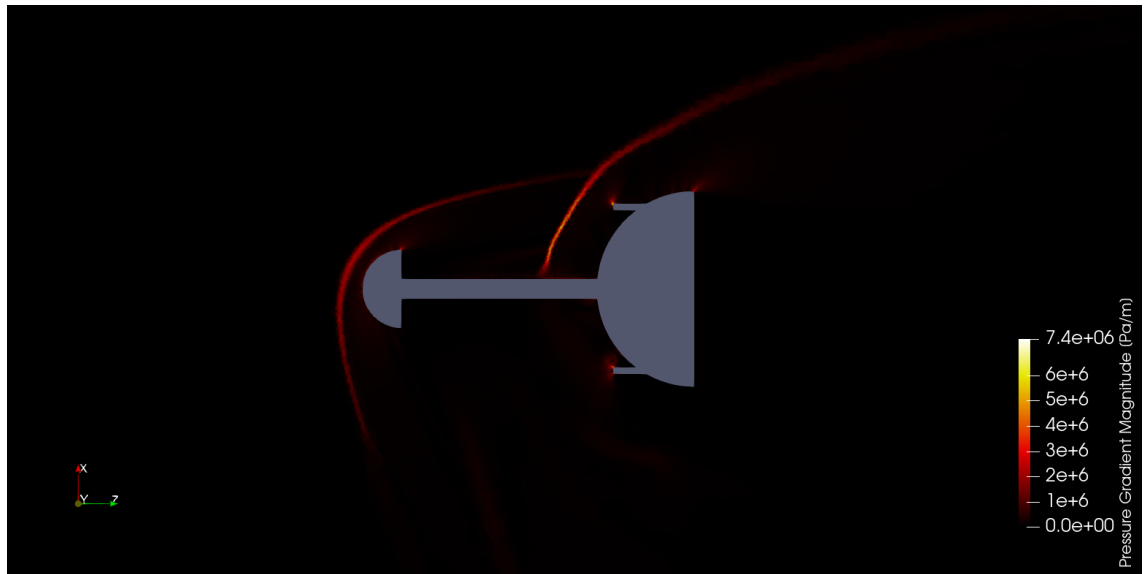


Figure 90: Pressure Gradient of Ringed Body 1 at Mach 2 and 30° AoA.

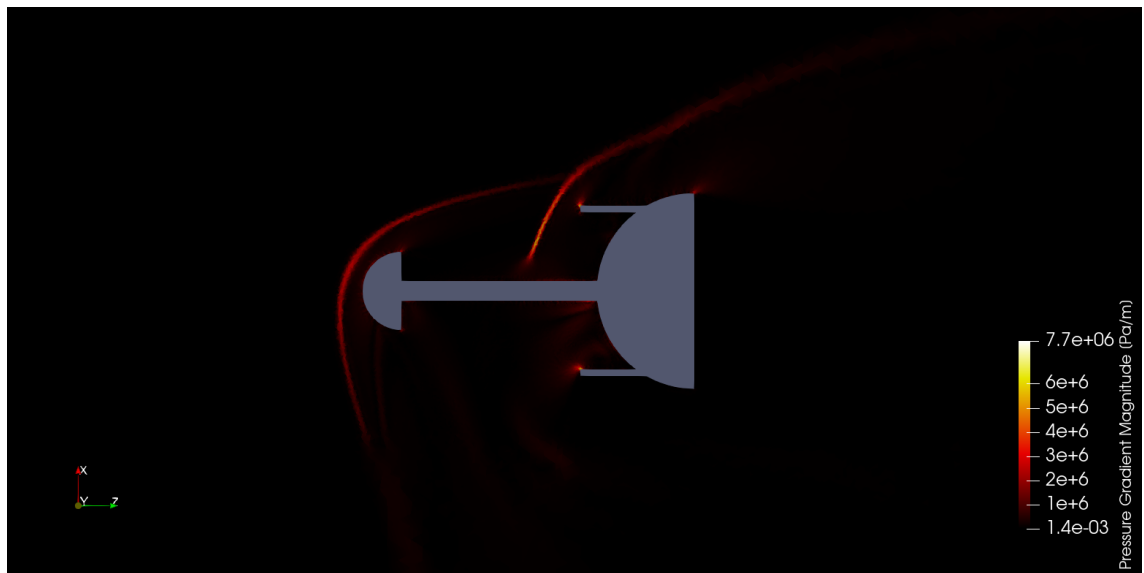


Figure 91: Pressure Gradient of Ringed Body 2 at Mach 2 and 30° AoA.

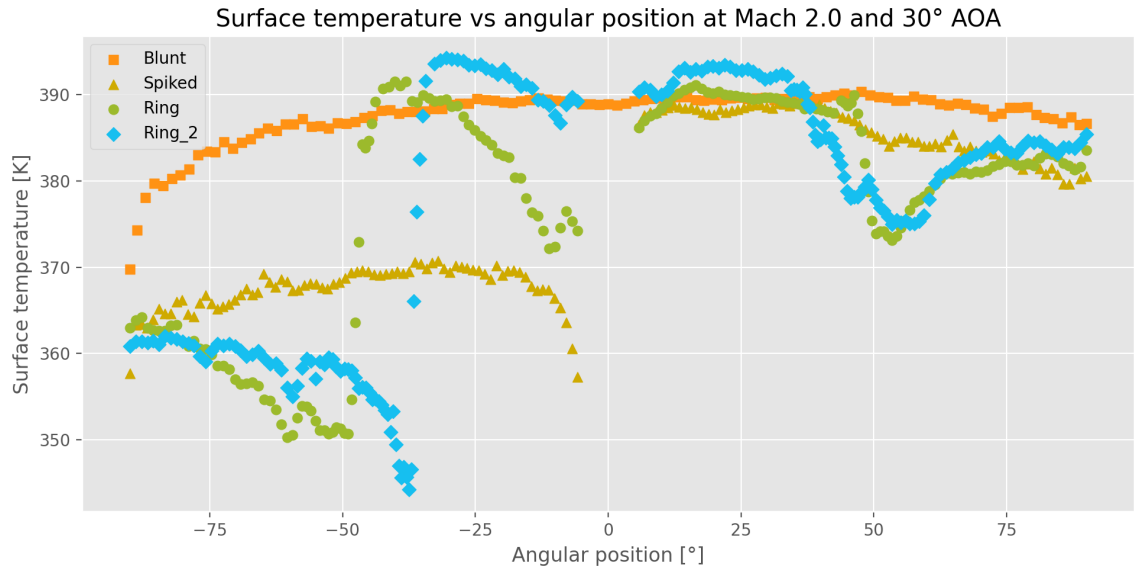


Figure 92: Fluid temperature on the body surface at Mach 2.0 and 30° AoA.

spike. The ringed bodies still show lower temperatures than the Spiked body on most of their surface, but where they don't the temperature is even greater than that of the blunt body, this really puts into question if they're still viable or not.

Figure 93 shows the wall heat flux of the four different bodies along the main body surface at a 30° angle of attack. The blunt body shows the least amount of heat flux around its stagnation point, and then it starts gradually increasing as the position approaches the body shoulders, except that on the lower side the heat flux drops significantly around the body shoulder. The Spiked body shows a behavior where its heat flux starts increasing from the root of the spike to the body shoulders, however, the heat flux is greater than that of the Blunt body on the upper side of the body, and lower on the lower side of the body, it also shows a small rise which rapidly decreases on the upper root of the spike, this is a cause of the stagnation of the fluid on this zone due to the presence of the spike. Moving on to the ringed bodies, their heat flux significantly rises around the spike root due to the stagnation zones previously discussed caused by the presence of the rings, the heat flux then start dropping only to dramatically rise and drop quickly on the rings' surfaces, this sudden rise and drop is caused by the ring outer surfaces having their stagnation mainly only on the tip of the ring, the heat flux then naturally starts slowly rising as the position approaches the body shoulders.

In conclusion, the Spiked body seems to still be effective both in drag and temperature reduction terms, even if its heat flux is greater than that of the Blunt body on its upper surface, the factor that determines whether or not the main body, its contents, and even its material are being protected is the temperature. The same cannot be the same for the ringed bodies, their drag coefficient is greater than that of the spiked body, and even if their surface temperature is lower than that of the spiked body on most of its surface, its surface temperature is significantly higher than that of the Spiked and even

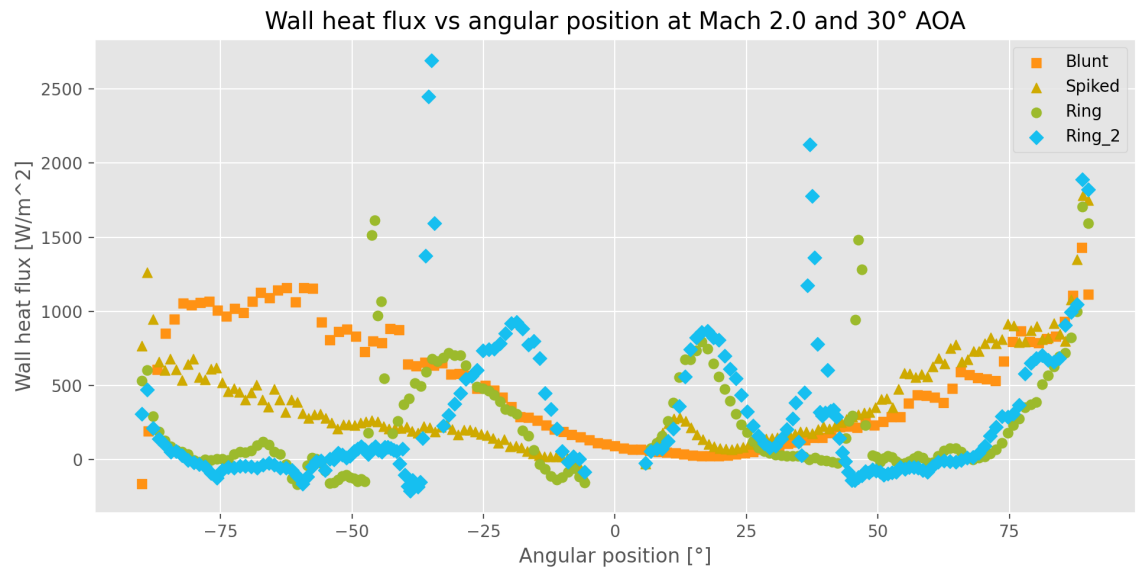


Figure 93: Wall heat flux at Mach 2.0 and 30° AoA.

the Blunt body on the rest of its surface, the same can be said about its heat flux, and because most of the time the aim is to protect all of the main body and not only some of its surface, they can easily be considered to no longer be viable.

Conclusions

All in all, it was shown that the Reattachment Ring can be used in cases where an angle of attack is present to further reduce the drag coefficient of a spiked body, its surface temperature/heat flux, or even both, depending on the length of the ring. However, the reattachment ring also reduces the angle of attack range where the spike is useful, where said range reduction is greater the longer the ring is. At small angles the ring can help the spike maintain its recirculation zone, but as the angle increases so does the projection area due to the presence of the rings, causing the surfaces where stagnation occurs to increase, leading to increments in both the drag coefficient and surface temperature/heat flux, the longer the length of the ring is the faster this happens. Furthermore, most probably, the greater the mach number is the smaller the working range of the rings is, as the speed of the flow causes this stagnation effects to be greater. However the fact that most of the time most vehicles will be flying at a 0° inclination must be taken into account, so even if the reattachment ring reduces the angle of attack range at which the spike effectively reduces the drag, the further drag, temperature, and heat flux reduction it would bring most of the time at a null inclination or at smaller angle of attack ranges could still be very much useful for a lot of vehicles. At the end of the day, the reattachment ring is another reduction method, another tool, and just as any other, its usefulness depends on its working conditions.

Further Research

Combinational schemes could prove to further reduce the drag coefficient and/or the heat flux, at null angles of attack, or even help solve the problems that arise at non-zero angles of attack. Furthermore, as Elsamanoudy et al. indicated, optimization tests still need to be carried out to better design rings according to the reduction objectives. It is the author's opinion that locating multiple rings along the main body surface or giving the rings an aeroshield, similar to that of the spike, could increase the angle of attack range at which the rings is effective.

References

- [1] Miguel de Unamuno. *Vida de Don Quijote y Sancho, según Miguel de Cervantes Saavedra, explicada y comentada por Miguel de Unamuno*. 1905.
- [2] M. Elsamanoudy, A. Ghorab, M. Hendy. *Drag Reduction Using Spiked-Aerodisk & Reattachment Ring for Hypersonic Hemispherical Bodies*. ASAT-15-151-AE, 2013. https://www.researchgate.net/publication/256129047_Drag_Reduction_Using_Spiked-Aerodisk_Reattachment_Ring_for_Hypersonic_Hemispherical_Bodies
- [3] CFD Online. *Navier-Stokes equations. Equations*. August 28, 2012. Consulted on November 16, 2021 from: https://www.cfd-online.com/Wiki/Navier-Stokes_equations#Equations
- [4] Nancy Hall. NASA. *Mach Number*. May 13, 2021. Consulted on November 23, 2021 from: <https://www.grc.nasa.gov/www/k-12/airplane/mach.html>
- [5] White, Frank. *Fluid Mechanics*. 4th edition. McGraw-Hill Higher Education, 2002, ISBN: 0-07-228192-8.
- [6] Wikipedia. *Drag coefficient*. Consulted on November 24, 2021 from: https://en.wikipedia.org/wiki/Drag_coefficient
- [7] Wikipedia. *Lift coefficient*. Consulted on November 24, 2021 from: https://en.wikipedia.org/wiki/Lift_coefficient
- [8] Cheng, J., Chen, R., Qiu, R., Sun, W., You, Y. *Aerothermodynamic study of Two-Stage-To-Orbit system composed of wide-speed-range vehicle and rocket*. 2021. Acta Astronautica. 330–345. <https://doi.org/10.1016/j.actaastro.2020.11.034>
- [9] Carlos Abraham Aguilar Vera. *Simulación Numérica de tópicos de flujo supersónico: Chorro supersónico subexpandido y flujo supersónico sobre un cuerpo con perfil de cápsula espacial*. Autonomous National University of Mexico. Faculty of engineering. Mexico. February, 2014.
- [10] Wikipedia. *Shock wave*. Consulted on November 26, 2021 from: https://en.wikipedia.org/wiki/Shock_wave
- [11] Sinclair, J., Cui, X. (2017) *A theoretical approximation of the shock standoff distance for supersonic flows around a circular cylinder*. Physics of Fluids 29. <https://doi.org/10.1063/1.4975983>
- [12] Wikipedia. *Schlieren photography*. Consulted on November 26, 2021 from: https://en.wikipedia.org/wiki/Schlieren_photography

- [13] Mizukaki, T. *Detached Shock Waves around Cylinders Flying at Mach Number Ranging from 1 to 2*. Journal of Visualization (Vol. 11, Issue 2), 133-141. Japan. 2008. <https://doi.org/10.1063/1.4975983>
- [14] Wikipedia. *Drag coefficient, Blunt and streamlined body flows*. Consulted on May 29, 2022 from: https://en.wikipedia.org/wiki/Drag_coefficient
- [15] M.Y.M. Ahmed, N. Qin. *Recent advances in the aerothermodynamics of spiked hypersonic vehicles*. Progress in Aerospace Sciences 47, 425-449, 2011. <https://doi.org/10.1016/j.paerosci.2011.06.001>
- [16] Michael S. Holden. *Experimental studies of separated flows at hypersonic speeds. I - Separated flows over axisymmetric spiked bodies*. AIAA Journal, 4(4), 591-599. 1966. <https://arc.aiaa.org/doi/10.2514/3.3494>
- [17] Zhen-guo Wang, Xi-wan Sun, Wei Huang, Shi-bin Li, Li Yan. *Experimental investigation on drag and heat flux reduction in supersonic/hypersonic flows: A survey*. Acta Astronautica 129, 95-110, 2016. <https://doi.org/10.1016/j.actaastro.2016.09.004>
- [18] Xiwan SUN, Wei HUANG, Min OU, Ruirui ZHANG, Shibin LI. *A survey on numerical simulations of drag and heat reduction mechanism in supersonic/hypersonic flows*. Chinese Journal of Aeronautics 32(4), 771-784, 2019. <https://doi.org/10.1016/j.cja.2018.12.024>
- [19] Menezes, V., Saravanan, S., Jagadeesh, G., & J. Reddy, K. P. *Experimental Investigations of Hypersonic Flow over Highly Blunted Cones with Aerospikes*. AIAA Journal, 41(10), 1955-1966. doi:10.2514/2.1885, 2003.
- [20] J. Michael Shoemaker, S. Saravanan, G. Jagadeesh, K. P. J. Reddy. *Aerodynamic spike flowfields computed to select optimum configuration at Mach 2.5 with experimental validation*. AIAA-9000414, 1990. <https://doi.org/10.2514/6.1990-414>
- [21] Economon, T. D., Palacios, F., Copeland, S. R., Lukaczyk, T. W., & Alonso, J. J. (2016). *SU2: An Open-Source Suite for Multiphysics Simulation and Design*. AIAA Journal, 54(3), 828-846. doi:10.2514/1.j053813
- [22] Cadence CFD. *The Reynolds-Averaged Navier-Stokes (RANS) Equations and Models*. Cadence-System Analysis. Consulted on September 26th of 2022 from: <https://resources.system-analysis.cadence.com/blog/msa2021-the-reynolds-averaged-navier-stokes-rans-equations-and-models>
- [23] NASA-Christopher Rumsey. (2021). *The Menter Shear Stress Transport Turbulence Model*. NASA, Langley Research Center, Turbulence Modeling Resource. Consulted on September 27, 2022 from: <https://turbmodels.larc.nasa.gov/sst.html>

- [24] Robert O. Piland. (December 9, 1952). *Preliminary Free-Flight Investigation Of The Zero-Lift Drag Penalties Of Several Missile Nose Shapes For Infrared Seeking Devices*. NACA, Langley Aeronautical Laboratory Langley Field, Va. Consulted from: <https://ntrs.nasa.gov/citations/19930090417>
- [25] C. Geuzaine and J.-F. Remacle. *Gmsh: a three-dimensional finite element mesh generator with built-in pre- and post-processing facilities*. International Journal for Numerical Methods in Engineering 79(11), pp. 1309-1331, 2009.
- [26] Henderson, A. *ParaView Guide, A Parallel Visualization Application*. Kitware Inc., 2007.
- [27] Mustafa Cavcar. *The International Standard Atmosphere (ISA)*. Anadolu University, Turkey.
- [28] Lawrence D. Huebner, Anthony M. Mitchell, Ellis J. Boudreaux. *Experimental Results on the Feasibility of an Aerospike for Hypersonic Missiles*. NASA Langley Research Center, USAF Wright Laboratory. 33rd Aerospace Sciences Meeting and Exhibit. AIAA 95-0737, January 9-13, 1995.
- [29] Autodesk. *Autodesk Inventor Professional 2024*. San Rafael, California, USA, 2023.